High-pressure infrared studies of Jahn-Teller-active and orientationally disordered C_{60}-based compounds

Dissertation zur Erlangung des Doktorgrades
der Mathematisch-Naturwissenschaftlichen
Fakultät der Universität Augsburg

vorgelegt von
Estaline Amitha Francis
aus Indien

September 2012

Erstgutachter:	Prof. Dr. C.A. Kuntscher
Zweitgutachter:	Prof. Dr. Armin Reller
Tag der Einreichung:	28 Sep 2012
Tag der mündlichen Prüfung:	30 Nov 2012

Contents

1. Introduction

Carbon has been an outstanding element for centuries with the two main forms, namely graphite and diamond. The discovery of the synthetic allotropes of carbon namely fullerene, nanotubes, and graphene starting from the end of the last century, made them a thriving field of research on their own. Due to their novel properties with potentially rich applications, carbon nanostructures have attracted a wide range of audience. A dramatic increase in exploration of the physics of carbon nanostructures was witnessed during the last three decades.

The fullerene-based compounds that were investigated within this project can be broadly classified as Jahn-Teller active fulleride anions and orientationally-disordered rotor-stator co-crystals. The samples that were studied are $(Ph_4P)_2IC_{60}$, A_4C_{60} (A = K and Rb), and $C_{60}{\cdot}C_8H_8$. Alkali fulleride and $(Ph_4P)_2IC_{60}$ were synthesized and characterized as a part of this project.

The main investigation method in this work is the high-pressure infrared spectroscopy. To investigate the properties of matter over a wide energy range, a well-established method is infrared spectroscopy. The vibrational and electronic spectra provide information about the microscopic mechanism that contributes to the overall electronic properties. In combination with the high-pressure technique, the infrared spectroscopy is a holistic approach to tune the material property, since compression of the lattice will directly influence the band width of electronic states. The main goals are to understand the pressure dependence of the phenomena namely the Jahn-Teller effects, insulator-to-metal transition, and orientational-ordering transition.

The C_{60}^- in $(Ph_4P)_2IC_{60}$ were investigated to understand the Jahn-Teller dynamics under high-pressure. $(Ph_4P)_2IC_{60}$ is an ideal system to study nearly isolated C_{60}^- in the solid-state environment due to the well positioned large cation. A vast amount of data on the temperature dependence of $(Ph_4P)_2IC_{60}$ by different techniques are available [1–5]. On cooling, C_{60}^- in $(Ph_4P)_2IC_{60}$ undergoes a dynamic-to-static Jann-Teller transition. By lowering the temperature, both the lattice constants and the thermal energy decreases whereas an increase in pressure only affects the former. The absence of any pressure-dependent studies on $(Ph_4P)_2IC_{60}$ made it an interesting compound to be investigated in order to understand if the external pressure effects on $(Ph_4P)_2IC_{60}$

is similar to effects produced by lowering the temperature. Infrared spectroscopy is a very sensitive technique as it can promptly reflect the molecular symmetry changes through splitting of the vibrational modes. By investigating the vibrational, electronic, and vibronic transitions in $(Ph_4P)_2IC_{60}$, the pressure induced changes on the Jahn-Teller distorted C_{60}^{-} can be understood.

In A_4C_{60} (A = K, Rb) the interplay of the electron interaction, the Jahn-teller effect, and the crystal field yield a very complex electronic behavior. At ambient conditions, the insulating property of A_4C_{60} was extensively studied by both theory and experiment. Both A_3C_{60} (A = K, Rb) and A_4C_{60} have a partly-filled t_{1u} band with strikingly different properties; A_3C_{60} is metallic and even superconducting at low temperature while A_4C_{60} is a Mott-Jahn-Teller insulator. An immense effort has been devoted to understand the properties of the alkali fulleride series of compounds under extreme conditions due to the superconducting behavior of A_3C_{60}. Among the scientific community working on A_4C_{60}, there are controversial ideas about their behavior under pressure, especially the driving mechanism responsible for the insulator-to-metal transition. Thus, A_4C_{60} are highly interesting compounds to study under high-pressure by infrared spectroscopy over a broad spectral range, as it can shed light on electronic states and would answer the open questions about the insulator-to-metal transitions. Also the Jahn-Teller dynamics of C_{60}^{4-} under pressure is interesting, as it provides a platform to understand the nature of the electronic behavior of the A_4C_{60}.

The other exciting compound that was investigated is the rotor stator co-crystal $C_{60}{\cdot}C_8H_8$. The $C_{60}{\cdot}C_8H_8$ has a neutral fullerene molecule in an expanded fcc lattice in comparison to pristine C_{60}, which on cooling undergoes orientational ordering transition similar to the pristine fullerene. Both C_{60} and $C_{60}{\cdot}C_8H_8$ are held together by weak Van der Waals interactions. The pressure induced orientational ordering transition in pristine C_{60} is a well studied phenomenon. This work is aimed at understanding the driving mechanism and the influence of the cubane molecule in the orientational ordering transition by investigating the vibrational properties of $C_{60}{\cdot}C_8H_8$ under hydrostatic pressure. Furthermore from the splitting of the infrared vibrational modes, the recently discovered space group (Pnma) of the ordered $C_{60}{\cdot}C_8H_8$ phase can also be confirmed.

The upcoming Chapter 2 is dedicated to the physics of fullerene and fullerene-based compounds which introduces various concepts that will be useful for understanding the results of this thesis. Chapter 3 gives an overview of the experimental techniques involved in this project, mainly infrared spectroscopy in combination with high-pressure technique and other details related to this work. This chapter also presents the theories related to the optical response functions and the models used for analyzing the optical

spectra under pressure. In Chapter 4 the synthesis of samples and characterization are reviewed in detail. The following three Chapters 5, 6, and 7 discuss the important finding of this work in detail about the Jahn-Teller effects in C_{60}^{-}, insulator-to-metal transitions in alkali fullerides, and orientational ordering transition in $C_{60}{\cdot}C_8H_8$, respectively. Finally Chapter 8 outlines the most important findings of this thesis.

2. Physics of fullerene and fullerene-based materials

2.1. Introduction

This chapter gives an overview of physics of C_{60} and fulleride anions particularly C_{60}^{-} and C_{60}^{4-} that are related to this thesis. The vibrational and electronic properties of fullerene are reviewed in detail. Other phenomena which are later used for discussion of the results are introduced in this chapter such as the Jahn-Teller effect, pseudorotation, vibronic coupling, orientational ordering transitions. Finally, section 2.11 is dedicated to the infrared spectroscopy on fullerene and fulleride anions.

2.2. C_{60} fullerene molecule

Carbon, known for centuries, is a naturally abundant nonmetallic element, that has atomic number 6 and belongs to the 4^{th} group of the periodic table. The most commonly occurring natural allotropes of carbon are graphite and diamond which have sp^2 and sp^3 hybridization, respectively. Fullerene, a molecular allotrope of carbon, was discovered in 1985 by Kroto *et al.* [6]. Since then fullerene has fascinated the scientific community and its discovery commemorated a new era of synthetic carbon allotropes. In 1991, carbon nanotubes were added to this family by Iijima [7]. The recent discovery of awe-inspiring graphene in 2004 by Novoselov and Geim [8], a one-atom thick sheet of carbon atoms arranged in honeycomb pattern is a new brainchild for researchers across the world.

Fullerene is a spherical molecule entirely composed of carbon atoms. C_{60} is the most abundant fullerene which is followed by C_{70}. Other higher fullerenes include C_{76}, C_{84} and more recently C_{80} [9]. The name fullerenes (nicknamed buckyball) was a homage to R. Buckminster Fuller, an architect who constructed the geodesic domes with similar structure. The discovery of fullerene by Kroto *et al.* was inadvertent while attempting to understand the formation mechanism of long-chain carbon clusters in interstellar space. Kroto, smalley and co-workers vaporized graphite in a high density

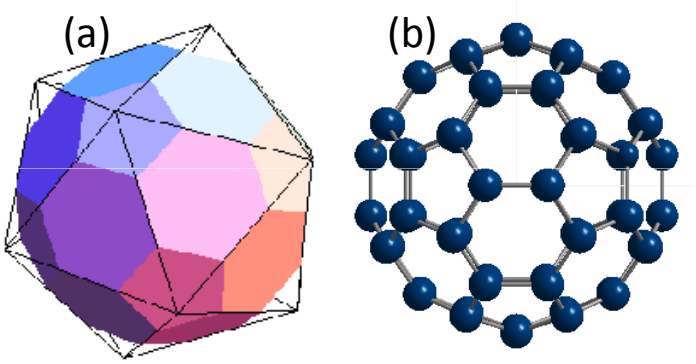

Figure 2.1: (a) The truncated icosahedron with pentagonal and hexagonal faces and (b) molecular structure of the C_{60}.

helium flow by a focused pulsed laser and analyzed the resulting distribution of carbon clusters by time-of-flight mass spectrometry [6]. They observed that for the clusters formed by more than 40 atoms only the even number of atoms were stable. However under certain conditions a peak at 720 amu corresponding to a cluster of 60 carbon atoms (C_{60}) was 40 times larger than neighboring peaks in the mass spectrum. They proposed that this extraordinary stability of C_{60} could be explained by the perfect symmetry of the molecule.

Finding fullerene in meteoroids was unsuccessful, which lead to the belief that fullerene were man-made allotropes until Busecker *et al.* [10] reported the presence of fullerene in carbonaceous rocks. Fullerene is predominantly synthesized in the lab by various techniques, but it can also occur in nature when carbon atoms encounter extreme conditions such as volcanoes, interstellar space, lightning, etc. Another constraint is that the effect of non-inert gases in nature can inhibit the growth and lifespan of fullerene. However overcoming all odds, fullerene was indeed spotted in an usual carbonaceous rock *Shungite* found in Shunga, Russia. In these 1.84 billion years old rocks, the presence of C_{60} and C_{70} was confirmed by HRTEM studies [10–12].

Synthesis of fullerene in macroscopic quantities was first reported by Krätschmer *et al.* [13] by arc discharge method over graphite and this brought the revolution in fullerene research. The structure of fullerene is a truncated icosahedron formed by removing the corners of a regular icosahedron, as shown in Fig. 2.1 (a). C_{60} consists of sixty equivalent carbon atoms in a spherical network with the shape of a football as shown in Fig.2.1 (b) with I_h point group symmetry. The surface of the C_{60} sphere with a diameter of 7 Å is formed by 12 pentagons and 20 hexagons. Each atom of C_{60} has a sp^2-like hybridization, but the curvature of the sphere gives rise to a small admixture of sp^3-character. Each carbon atom has 4 valence electrons, three of which occupy the lower lying molecular orbital (MO) forming the σ–bond that stabilizes the cage and the fourth electron participates in the formation of outermost molecular orbitals with π–characteristics. The C_{60} molecule consists of 360 electrons, out of which 120

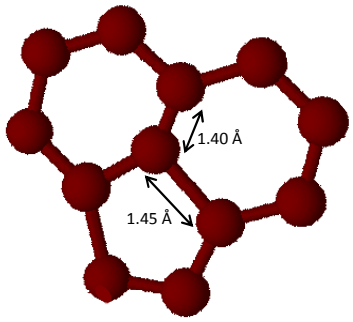

Figure 2.2: Schematic representation of single (1.45 Å) and double bond (1.40 Å) alternation of carbon atoms in C_{60} molecule [16]

are core electrons and the remaining 240 electrons belong to the valence molecular orbitals which delocalize over the spherical surface of the molecule. The 60 conjugated π electrons are mainly responsible for the electronic properties of C_{60}. The two type of carbon bonds forming the C_{60} molecules are shown in Fig. 2.2; (i) there are 30 double bonds (C=C) of length 1.40 Å, that fuse two hexagons and (ii) 60 longer single bonds of length 1.45 Å that hold the pentagon to hexagon [14]. This results in conjugation, that is known as *alternation* of single and double bonds [15]. Difference in the bond length gives rise to a non-uniform electron density distribution over the molecule. This project is on C_{60}-based compounds, so any further reference to fullerene will refer to C_{60} unless stated otherwise.

2.3. C_{60} fullerides

The C_{60} molecule in the solid-state forms a face centered cubic (fcc) structure as shown in Fig. 2.3. The crystalline form of fullerene is termed as *fullerites*. The C_{60} molecules in fcc lattice are held together by the weak Van der Waals interaction. The symmetry of fcc C_{60} is $Fm\bar{3}m$ and the lattice constant is $a = 14.17$ Å with the nearest-neighbor distance of 10.02 Å [17]. The cubic symmetry is not compatible with I_h space group, thus the equivalence of all the carbon atoms as in the case of the molecule is not valid in the solid C_{60}, giving rise to three inequivalent carbon atoms in fulleride crystals.

In the solid-state, the electronic properties of the insulating C_{60} crystal are inherited from the molecular ones [16]. At room temperature, the C_{60} molecules are orientationally disordered and undergo continuous reorientation. Therefore all the four C_{60} molecules of the cubic cell become equivalent in time average. Crystals which have such rapidly reorienting molecules with effective symmetry higher than the molecular symmetry are known as *plastic crystals*.

The C_{60} crystal is a fairly open structure with voids. The fcc C_{60} has a tetrahedral

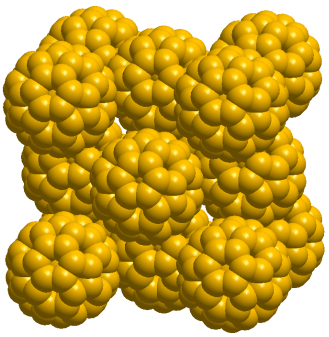

Figure 2.3: Structure of solid face centered cubic C_{60}.

and octahedral interstitial site of size 2.2 Å and 4.2 Å, respectively [16]. These empty sites provide immense opportunities for doping chemistry. The high electronegativity of the C_{60} makes it a potential host for reductive intercalation chemistry. The octahedral sites are large enough to intercalate any alkali ion while the tetrahedral site can only accommodate Li^+ and Na^+ without expanding the lattice. Depending on the number and nature of the intercalated molecule the structure and properties of the solid vary. The most extensively investigated intercalated compounds are the family of alkali metal, alkaline earth metal and rare earth fullerides.

2.4. Group theoretical background

The group theory can simplify the theoretical framework for describing the electronic structure of the icosahedral fullerene. In order to analyze the vibrational and electronic spectra of fullerene-based material, a basic understanding of group theory and transformation of the 180 degrees of freedom of C_{60} by symmetry operation of the I_h point group is important. C_{60} has high symmetry that leads to many degeneracies in the vibrational modes and the electronic levels. The eigenstates of C_{60} are conveniently classified using symmetry in terms of irreducible representations (*irreps*) of the icosahedral point group.

A molecule with N atoms will have $3N - 6$ normal modes, that include vibrational, translational and rotational degrees of freedom. For a non-linear molecule, the translational and rotational motions are ignored to determine the number of normal modes (*i.e.* $3N$ – *the number of the non-vibrational motions*). A *normal mode* vibration of a molecule can be explained as when the atoms in the molecule move with the same vibrational frequency and simultaneously pass through their equilibrium positions with the center of mass remaining in the same position.

According to the group theory the 180 degrees of freedom of C_{60} molecule can be

written as [18]

$$\Gamma_{vib} = 2A_g + 3T_{1g} + 4T_{2g} + 6G_g + 8H_g + A_u + 4T_{1u} + 5T_{2u} + 6G_u + 7H_u \qquad (2.1)$$

The T_{1u} and T_{1g} correspond to translational and rotational modes, respectively and hence omitting these modes we obtain 174 normal vibrational modes [19]. A C_{60} molecule has 120 symmetry operations, as it belongs to the highest symmetry point group allowed in the three dimensional space. High symmetry of the molecule leads to high degree of degeneracy of the molecular orbitals. The group theory notations are useful for describing the symmetry of C_{60} molecule which are as follows:

- The normal modes of the molecules are identified using irreducible representations (*irreps*). Each *irrep* is defined by basic functions that transform among themselves.
- The label A, E, T, G, and H are used to label sets of 1, 2, 3, 4, and 5 degrees of freedom, respectively.
- Additional labels g and u stand for *gerade* and *ungerade*, respectively. These are used to distinguish between irreps that have even and odd natures.
- The electronic states will be labeled using lowercase letters and the vibrational states by the uppercase letters. For example, the $t \otimes H$ system involves a coupling of a triply degenerate electronic state with the fivefold degenerate vibrational state.

2.5. Electronic structure of fullerene

The high degree of symmetry makes the calculation of the molecular orbitals easy which could otherwise be difficult to obtain for such a large number of electrons. For solid C_{60} there are two energy scales: (i) associated to the strong covalent bonds of the cage and (ii) due to the weak Van der Waals inter-fullerene interactions of the solid. The most important electronic states of C_{60} are the highest occupied molecular orbital (HOMO), which is fivefold degenerate with h_u symmetry and the lowest unoccupied molecular orbital (LUMO), which is threefold degenerate with t_{1u} symmetry. The LUMO, which is strongly electronegative has a non-bonding nature. The HOMO is completely occupied by ten electrons. These states can be calculated using Hückel theory of molecular orbitals for C_{60} and are shown in Fig. 2.4 [20]. The neutral C_{60} is a semiconductor with an energy gap of 1.87 eV (between the HOMO and LUMO) [22]. When new electrons are added to the C_{60}, the conduction band fills progressively and

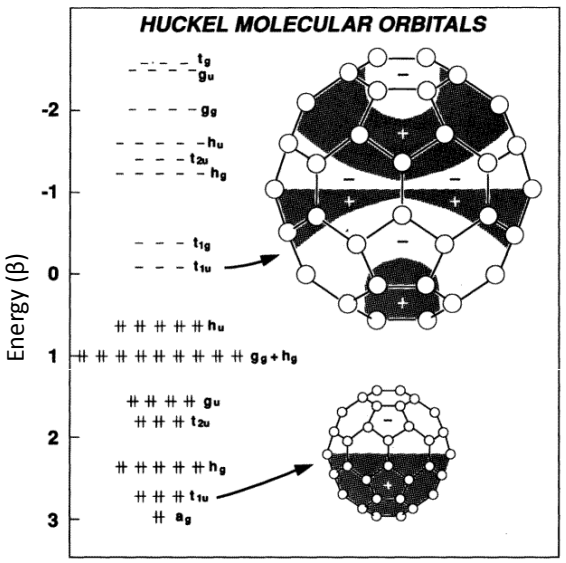

Figure 2.4.: Molecular orbital levels for the C_{60} from a Hückel calculation (unscaled β, where β is the resonance integral). The filled states are represented by $+$ and the empty states by $-$ [20, 21].

in turn it influences the electronic properties of the solid. For isolated C_{60} molecule, the two bond lengths are the only degrees of freedom of its equilibrium structure. The solid C_{60} has additional degrees of freedom of the Bravais lattice, the orientation, the number of molecular units within the primitive cell, and the distortion of the molecule due to the crystal field [23].

When a system has perfect symmetry, the energy levels are characterized by the angular momentum number l. For icosahedral symmetry, l is no longer a good quantum number, whereas the energy levels of C_{60} still preserve the well-defined l character. The second and third highest occupied states g_g and h_g correspond to l=4 states of the spherical symmetry, and highest occupied state h_u and lowest unoccupied state t_{1u} to the $l = 5$ states. The optical transitions from a state characterized by l to the outer state $l\pm1$ are expected to have strong oscillator strengths [24]. Fig. 2.5 shows the energy level diagram of C_{60} molecule and its band structure. The optically-allowed transitions in C_{60} are indicated by arrows in Fig 2.5(a). Table 2.1 summarizes the excitations with its corresponding theoretical energies.

From the bottom of the valence band to 15 eV above the conduction band minimum, C_{60} has nearly 250 bands. Thus it is worth developing a simple model to describe the molecular orbitals as shown in Fig. 2.4 [25]. For fcc C_{60}, the levels between -6 and $+7$ eV are assigned to the π-bond states which have considerable dispersion. As the

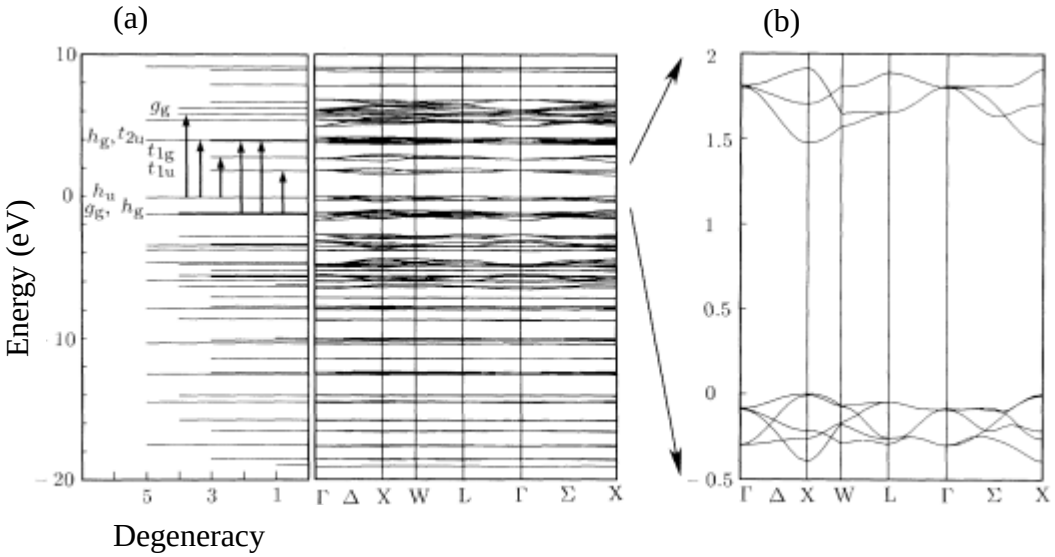

Figure 2.5.: (a) Electronic energy levels of the C_{60} molecule (left) and the band structure of the fcc C_{60} (right), and (b) band structure of fcc C_{60} around the energy gap [26]

π-bonds of C_{60} spreads outside the molecule more than the σ bond thus having a larger intermolecular overlap [26]. The levels above 7 eV are assigned to antibonding σ-states, which has a little dispersion in fcc C_{60}. The rotation of the fullerene in fcc C_{60} affects the dispersion of the energy bands since the fullerene is not perfectly spherical due to the presence of the internal bond network. Furthermore, the rotation of the C_{60} in fcc lattice smears out the detailed dispersion of the energy band.

The electronic properties can be modified even by a weak interaction in fullerene-based materials by lifting the ground state degeneracy. One of the ways to do it is

Optical excitations	energies (eV)
$h_u \rightarrow t_{1g}$	2.87
$h_g \rightarrow t_{1u}$	3.07
$h_u \rightarrow h_g$	4.06
$g_g \rightarrow t_{2u}$	5.09
$h_g \rightarrow t_{2u}$	5.17
$h_u \rightarrow g_g$	5.87

Table 2.1.: Assignment of optical excitations of C_{60} and its energies [26].

by doping. There are three possible doping types: (i) exohedral doping (intercalation in the solid phase), (ii) endohedral doping (doping inside the fullerene cage), and (iii) Hetrofullerene formation (on-ball doping by substituting carbon atoms mainly with nitrogen atoms). Addition of electrons into the LUMO can completely change the properties of C_{60}. For example, C_{60} can be tuned from insulator to metal or even to superconducting state at low temperature by doping. The energy scale of their electron-lattice interaction is comparable to their electronic bandwidth, therefore the interplay between the electronic and lattice degrees of freedom is important in fullerenes [27].

The following sections will introduce different phenomena and terminologies related to C_{60}-based compounds, that will be used in this thesis.

2.6. An introduction to Jahn-Teller effect

The Jahn-Teller (JT) effect can be stated as *all nonlinear polyatomic molecular system in a degenerate electronic state will be unstable and will undergo distortion to form a system of a lower symmetry and lower energy thereby removing the degeneracy.* This was initially articulated in 1934 by L. D. Landau and E. Teller while discussing the stability of CO_2 molecule [28]. In 1937 it was verified by Hermann Arthur Jahn and Edward Teller with the use of the group theory. They showed that any system of linear molecule with degenerate electronic states should be stable with no exceptions. The theorem in other words can be put forward as the stability and degeneracy are not simultaneously possible unless the molecule is colinear. When a system has two or more distinct states with exactly the same energy, nature tries to avoid this by inducing a physical distortion of the molecule so as to split the energy levels apart [29], which is known as the *Jahn-teller distortion* (JTD). In general, the systems with higher symmetry result in large number of symmetry operations in the group, thus the degeneracy of the energy levels will be higher. When a perturbation is applied to lower the symmetry, the degeneracy of the molecule can be reduced. Suppose a molecule or a crystal is squeezed to lower its symmetry, it would most likely lift some of the level degeneracies. The work within this project involves Jahn-Teller active C_{60}-based compounds such as C_{60}^{-} and C_{60}^{4-}, thus the Jahn-Teller effects in fullerene are introduced here. Essentially the starting point is the adiabatic approximation to further understand the Jahn-Teller effect.

2.6.1. Adiabatic approximation

To understand the quantum mechanical treatment of the molecular structure, some simple approximations are made. The most basic of them is the adiabatic or Born-Oppenheimer approximation, which assumes that the nuclear and electronic motions can be separated as their masses are significantly different which in turn give rise to the difference in their velocity. The heavier nuclei move much more slowly than the electrons. Therefore for each instantaneous position of the nuclei, a stationary distribution of the electronic cloud can be attained. The nuclei move in the average field of the electrons, which is thus a function of nuclear coordinates. The Jahn-Teller effect is a most striking deviation from the adiabatic approximation. At the point of electronic degeneracy the adiabatic approximation breaks down and there is vibronic coupling between the electronic states and the nuclear motion. This could otherwise be explained as in a system with Jahn-Teller effect, the electrons do not adiabatically follow the motions of the nuclei, and the nuclear states are determined not only by the average field of electrons, but also by the details of the electronic structure, and their changes under nuclear displacements.

The Hamiltonian of a molecule or crystal can be written as

$$H = H_Q + H_r + M(r, Q) \tag{2.2}$$

where H_Q is the kinetic energy of the nuclei, H_r is the electronic component, and M(r,Q) refers to the vibronic interaction energy (*i.e.* the potential energy between the electron-nuclei, electron-electron and nuclei-nuclei), where r and Q marks the set of electrons and nuclei coordinates, respectively.

2.6.2. Adiabatic potential energy surface

The difference in the timescale of the electronic and nuclear motion leads to the so-called electronic adiabatic approximation. By assuming that the nuclei is fixed in a spatial configuration, the electronic eigenvalues as a function of this chosen nuclear coordinate describes a curve and it is known as the *adiabatic potential energy surfaces* (APES). When the coupling strength is strong, the energy difference between the APES will be much greater than the vibrational energy $\hbar\omega$. Thus, the nuclear motion will be confined to the lowest APES. For linear coupling terms, the APES will have either *trough i.e.* continuous equal energy surface or *wells i.e.* distinct minima. The nature of the Jahn-Teller effect in terms of APES can be explained on the basis of the strength of the coupling. For infinite coupling, the well are infinitely deep, thus the JT system is localized in one of the wells. The eigenstates of the system will be associated

with the well states. Such a condition is termed as the *static JT system*. Similarly the dynamic JT effect can be explained when the system has a finite coupling strength. The height of the barriers between the well are finite, therefore the system can tunnel from one well to the other. The correct eigenstates will be symmetry adapted states which are linear combination of the well states. The tunneling between the wells of the APES is known as the *dynamical JT effect*.

2.7. Jahn-Teller effects in fullerene-based materials

When the Born-Oppenheimer approximation fails, the non adiabatic terms become sizeable which has to be accounted for in the expression for the total energy. These terms couple electronic and nuclear motion, inducing transitions between the electronic states. Typical examples are molecules with degenerate ground state, where transitions between the degenerate states are easily induced by this coupling. The high symmetry of the C_{60} molecule leads to highly degenerate electronic and vibrational levels. According to the JT theorem, the non-linear system with electronic degeneracy is distorted by the coupling of the electrons to some specific molecular vibrations called the JT active modes, so as to lift the degeneracy and lower the total energy. For C_{60} ions the electron(s) of the t_{1u} orbital are spread over the entire surface of the fullerene and can couple to the vibrations of the molecular cage itself. Generally not all the modes can couple to the electronic orbital to give rise to Jahn-Teller interactions. In C_{60} molecule, among the 174 normal vibrational modes, only 2 A_g and 8 H_g modes satisfy the conditions to be JT active modes. Thus, the t_{1u} electronic state is allowed to couple only to these normal mode. The coupling to the A_g mode is usually neglected as it is a breathing mode and thus does not affect the electronic degeneracy but only introduces a constant shift in the energy levels. In C_{60}, the vibronic coupling is due to the t_{1u} mode coupled to the 8 H_g mode and can be expressed as $t_{1u} \otimes 8\ H_g$. The coupling to 8 H_g can be reduced to one effective mode because this reduction does affect much the energy levels. Therefore, $t_{1u} \otimes H_g$ can be used as a good approximation to analyze the vibronic coupling in fullerene molecules [30]. The common notation used for expressing the JT effect in fulleride ions is $p^n \otimes H$ where p^n represents the n number of electron configuration in the atom [31]. Klupp *et al.* have discussed well the theoretical background for the Jahn-Teller active fullerene-based compounds, which is briefly presented here [31].

The Hamiltonian for $p^n \otimes H$ system with linear coupling can be written as [32]

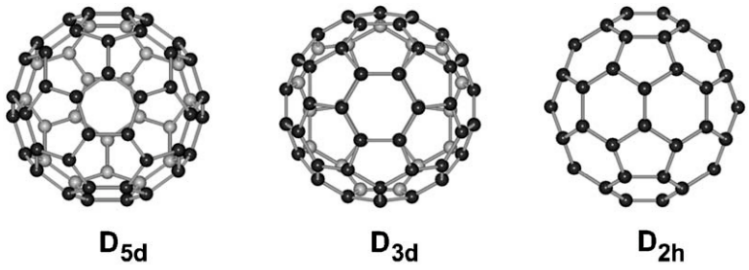

Figure 2.6.: The possible distortion of the fulleride ions. The atoms marked in black are above the plane of the paper and those with grey are below the plane of the paper. [33].

$$\hat{H} = -\frac{1}{2}\sum_{i=1}^{5}\frac{\partial^2}{\partial Q_i^2} + \frac{1}{2}\sum_{i=1}^{5} Q_i^2 + \hat{M}(Q_i) \tag{2.3}$$

where $\hat{M}$ (Q_i) is the vibronic interaction energy and Q_i are normal coordinates spanning a five dimensional space containing the APES. The first term represent the kinetic energy and the second is the potential energy ($\hat{V}$) of the five simple harmonic oscillators, which together transform as the H irrep, with coordinates Q_n (n = 1,...,5). The APES of the potential energy does not have a single minimum but has a three dimensional spherical subspace of the five dimensional Q space. The smallest eigenvalue of the M matrix is -ηkQ where η is the constant that depends on the charged state of fulleride ion [30] and k is the vibronic coupling constant. With this we get,

$$\hat{V} = \frac{1}{2}Q^2 - \eta k Q \tag{2.4}$$

which has a minimum at Q = ηk with the Jahn-Teller energy of $\frac{1}{2}$k^2. This result hold good for all the 8 H_g modes of C_{60}^{n-}. Therefore the APES is a 3D spherical surface with radius ηk.

For example [33], C_{60}^{4-} belongs to $p^4 \otimes H$ system, the allowed Jahn-Teller distortions for isolate ion are predicted to be D_{2h}, D_{3d} or D_{5d} [32]. Fig. 2.6 shows the possible distortions with C_5, C_3, and C_2 axes perpendicular to the plane of the paper for D_{5d}, D_{3d}, and D_{2h}, respectively. This system has a minima at D_{3d} or D_{5d} symmetry and a saddle points at D_{2h} symmetry. The C_{60}^{-} and C_{60}^{2-} molecules are either elongated or compressed along the C_5 axis by D_{5d} symmetry similar to the C_{60}^{4-} ion. The distortion corresponding to the minimum of the APES is prolate in $p \otimes H$ and $p^2 \otimes H$ system *i.e.* in C_{60}^{-} and C_{60}^{2-}, respectively. And an oblate distortion for $p^4 \otimes H$ and $p^5 \otimes H$ system

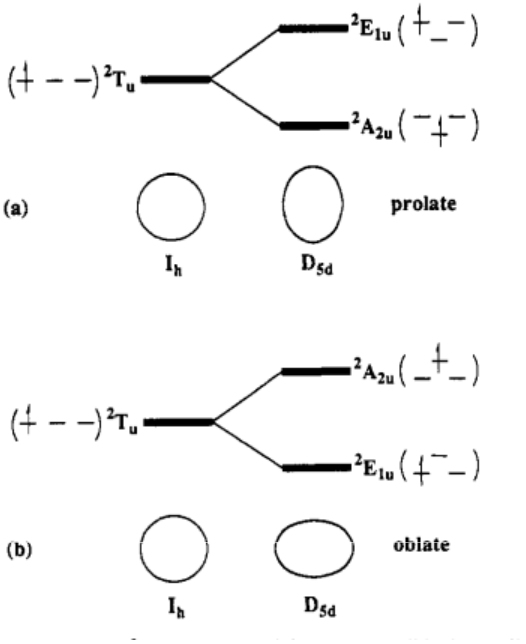

Figure 2.7: Splitting of the T_u orbital scheme of C_{60}^- (a) prolate or (b) oblate distortion from I_h to D_{5d} symmetry with corresponding electronic configurations [35].

[34]. Fig. 2.7 (a) shows a distortion with fivefold symmetry axis in D_{5d} point group for C_{60}^- [35]. Since all points on the APES corresponding to the minimum are equivalent, all distortion corresponding to these points are equally probable. This leads to the continuous change of the main axis, with the molecule undergoing pseudorotation [32, 34].

2.8. Pseudorotation

A system tunnels through the wells and in case of a trough the tunneling is substituted by the rotation of the distortion. For example, in C_{60} anions the Jahn-teller effect can distort in six different directions for D_{5d} symmetry and ten directions for D_{3d} symmetry [36]. If the APES contains wells, the symmetry is restored by tunneling between the wells, and if it contains troughs the symmetry is restored by free or hindered rotations of the distortion around the trough [37]. During pseudorotation the point group of the molecule changes while it remains icosahedral on the average [31].

The pseudorotation is clearly different from the real rotation. The pseudorotation is an intramolecular motion in an angular direction which appears as a fluctuation traveling through the distorted geometrical center of the cluster as shown in Fig 2.8 (a). Real rotation can be explained as when all atoms of the molecule rotates simultaneously around a proper axis as shown in Fig. 2.8 (b) wherein one of the atoms is marked in red to guide the eye. The pseudorotation in C_{60}-based compounds are

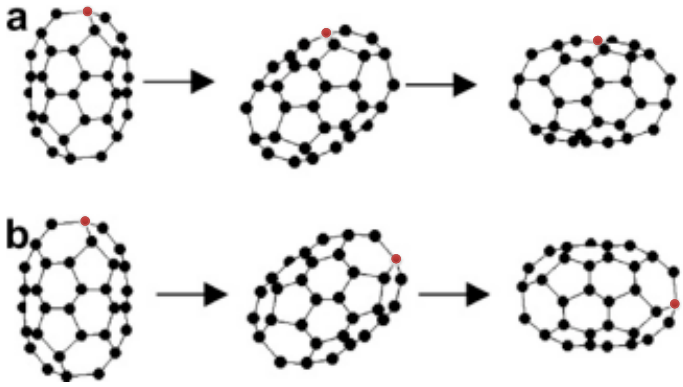

Figure 2.8.: Schematic representation of (a) pseudorotation and (b) real rotation of C_{60}^- ion. One of the carbon atoms has been colored red for reference [37].

expected to occur in the time scale of a few femtoseconds faster than the molecular rotation which itself occurs on a time scale of few picoseconds [38]. The pseudorotation was studied theoretically on E $\otimes$ e for both linear and quadratic JT coupling. E $\otimes$ e system was chosen as it is relatively simple system with low dimensionality and the idea can be extended to more complicated systems. Fig. 2.9 illustrates the pseudorotation pictorially for linear and quadratic coupling in the E $\otimes$ e system. Pseudorotation can be classified as free-rotation, hindered rotation, and pulsating rotation. Free rotation, occurs when the APES has trough and the system is free to rotate among these minimum. The APES of free rotation is illustrated in Fig. 2.9 (b). Hindered rotation has APES as seen in Fig. 2.9 (c), it occurs when there are potential barriers between discrete minima that are small compared to the quanta associated with the radial vibration, then the system can stay in the minima for a longer time than at the maximum of the barrier. The resulting motion appears as slow changes in the nuclear configurations. And pulsating motion takes place if the height of the potential barrier is larger than the quantum of radial vibration. The APES for pulsating or fluctuating type of pseudorotation can be visualized as shown in Fig. 2.9 (a). The dynamical motion of the system is described by the localized vibrations in the minima accompanied by tunneling between them, the motion would appear as periodic change in the orientation of the distorted nuclear configuration and this could lead to tunnel splitting which is a significant observable of the JT effect. Hands *et al.* [38] derives the pseudorotational period T_p for E $\otimes$ e system theoretically which is given by

$$T_p = \frac{2\pi\hbar}{\Delta} \tag{2.5}$$

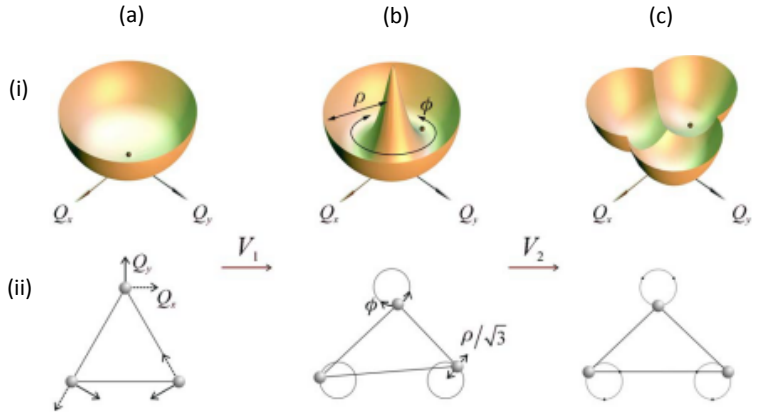

Figure 2.9.: (i)APES of E ⊗ e (black point) in Q space with consecutive inclusion of linear (V_1) and quadratic (V_2) coupling. (ii) representation of the orientation of triatomic molecule in real space. a (i) and (ii) represents the system with no coupling. b (i) illustrates the free rotation around the trough and (ii) represents the corresponding distortion of molecule in real space. (c) (i) shows the system locked in one of the wells giving rise to hindered rotation and (ii) bold points on the circles shows the positions of the wells where the atoms rest for a longer time before moving to another position in real space [38].

and the rate is given by

$$R_p = T_p^{-1} = \frac{\Delta}{2\pi\hbar} \tag{2.6}$$

where Δ is the difference between the energies of the tunneling states and ground state. Experimentally, pseudorotation can be detected by ultra fast spectroscopic techniques.

2.9. Vibronic Coupling

The term vibronic is formed by concatenation of the terms vibrational and electronic, which denotes the coupling between the electronic states and molecular vibrations, that is responsible for the JT effect. The vibronic coupling is one of the fundamental type coupling in molecules and solids, it plays an important role in the JTE, charge transport, superconductivity, etc. The distortion of the molecule is influenced by the

motion of the electrons and results in vibronic interactions in the direction of the distortion.

According to Hückel molecular orbital theory, the extra electrons are added to the t_{1u} molecular orbital. As described in Sec. 2.7, the vibronic coupling problem in fullerene-based ions can be written as $t_{1u} \otimes 8\ H_g$ problem. The first work on vibronic coupling of C_{60}^- was published by Varma *et al.* in 1991 [39]. Gunnarsson *et al.* in 1995 studied experimentally the vibronic coupling in fullerene by photoelectron spectroscopy of C_{60}^- and also evaluated the coupling constants [40].

There are several theoretical approaches to analyze vibronic coupling in fullerene-based compounds by taking into account different interactions and types of coupling (*e.g.* linear/quadratic). The Hamiltonian for simple molecular problem may be written down in different forms, but a simple comparison of the Hamiltonians can be made to relate the alternative forms. As an example the JT Hamiltonian for the $t_{1u} \otimes H_g$ (taking into account only a single vibrational mode) can be written as [41]

$$\hat{H} = \sum_i \left(\frac{P_i^2}{2\mu} + \frac{1}{2}\mu\omega^2 Q_i^2 \right) + V_H \sum_i Q_i C_i \tag{2.7}$$

where V_H is the coupling constant, μ is the reduced mass, ω is the frequency, and P_i is the momenta conjugate to Q_i. The C_i are the electronic operators summed over all the five components of i of the h_g modes. A label (e.g. k) must be added to V_H, ω, and E_{JT} when more than one mode of a given symmetry is included such as in $t_{1u} \otimes 8\ H_g$. For this the JT energy is given by

$$E_{JT} = -\frac{V_H^2}{5\mu\omega^2} \tag{2.8}$$

and the coupling strength according to calculations based on a frozen-phonon technique is given by $g_k = \sqrt{2\mu\omega_k^2 E_{JT}^{(k)}}$ [42].

The coupling strength determines the nature of the Jahn-Teller distortion. If the coupling is very strong, it results in static JT distortion and it can be conceived as the molecule is permanently distorted into a configuration of lower symmetry. If the coupling is weaker, then the situation is described in terms of a dynamic JTE, where the system continually migrates between several equivalent symmetry as a result of quantum mechanical tunneling. The rate of tunneling is directly influenced by the coupling strength.

2.10. Orientational ordering transitions in C_{60}

At room temperature NMR spectra showed a narrow line at characteristic frequency for aromatic carbons. This narrow line is due to the fact that the chemical shift anisotropies are averaged out which demonstrates the rapid rotation of C_{60} molecule isotropically in solid state. The fullerene molecules rotate freely at picoseconds time scale, owing to its spherical shape [43]. Heiney *et al* [17] in 1991 first reported the orientational ordering phase transition at 250 K. It was also confirmed by several experiments for example differential scanning calorimetry (DSC) [17], ^{13}C-NMR [44] measurements, neutron diffraction measurement [45], thermal conductivity [46], and infrared spectroscopy [47,48]. Below the orientational ordering transition temperature, the molecules perform thermally activated jump-diffusion between two nearly degenerate orientations separated by a potential barrier ∼12 meV and an energy barrier of ∼260 meV experimentally (∼300 meV theoretically) [49]. The molecules are orientationally ordered on four different sublattices [50] and the symmetry of the ordered phase was determined by XRD to be simple cubic (sc) with $Pa\bar{3}$ point group [17]. The orientational ordering transition was also well investigated theoretically [51]. The energy bands for the orientationally disordered and ordered phase differ from each other considerably.

Not only temperature lowering of C_{60} can induce orientational ordering transition but also the application of external pressure can have similar effects. The pressure dependent orientational ordering transition on C_{60} molecules was reported by pressure-dependent differential thermal analysis (DTA) [52], XRD [53], etc. The fcc-sc phase transition temperature increased with increase of pressure at the rate of 10.4±0.2 K/kbar. Furthermore, the pressure affects the fluctuations in the ordered low temperature phase with nearly a complete suppression of the fluctuations at about 8 kbar at room temperature [52].

Within this project the orientational ordering transition in $C_{60}{\cdot}C_8H_8$ is investigated under high pressure in order to probe the critical transition pressure and evaluate the driving mechanism of the transition.

2.11. Infrared spectroscopy on C_{60}

Vibrational spectroscopic techniques are powerful tools to investigate C_{60}-based compounds, since they can detect any symmetry changes of the molecule. The degree of the splitting of the phonon modes in infrared and Raman spectroscopy can provide information about the symmetry of the molecule. C_{60} has only 4 T_{1u} IR active modes

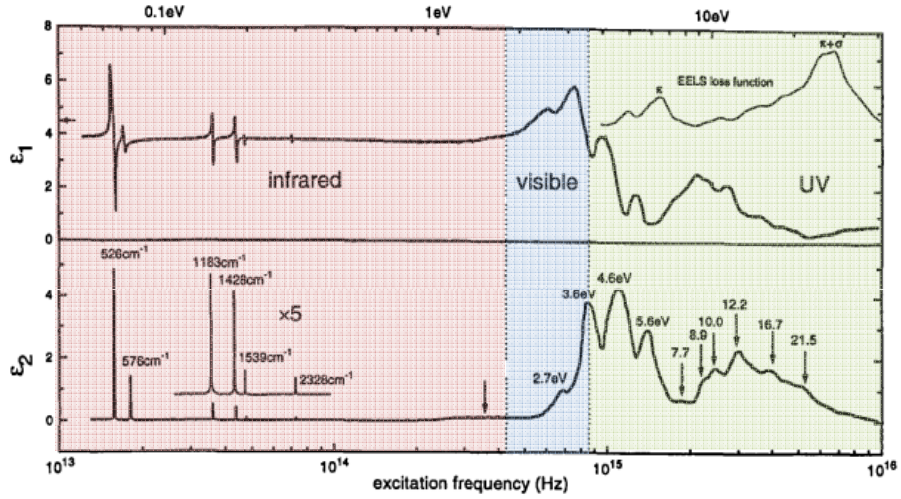

Figure 2.10.: The real $\varepsilon_1(\omega)$ and imaginary parts ($\varepsilon_2(\omega)$) of the dielectric function for C_{60} over a wide frequency range based on FTIR transmission data, variable angle spectroscopic ellipsometry data, and electron energy loss spectroscopy data [54]. The arrow on the left side of the upper panned points to the low-frequency value of the dielectric constant obtained from capacitance measurements ($\varepsilon_1 = 4.4$).

due to the symmetry considerations. The IR spectrum of the solid C_{60} is nearly the same as that of the isolated C_{60} molecule, this reflects the highly molecular nature of the solid C_{60}. By infrared spectroscopy a variety of phenomena can be investigated in fullerene and its ions, such as the orientational ordering transition, insulator-to-metal transition, JT effects, charge transfer, etc. The optical data [$\varepsilon(\omega)$] of solid C_{60} film over a very broad range (about 0.05 to 13 eV) is presented in Fig. 2.10. The upper panel shows the frequency dependence of the dispersive part [$\varepsilon_1(\omega)$; real part] and the lower panel shows the absorptive part [$\varepsilon_2(\omega)$; imaginary part] of the dielectric function of solid C_{60}. The optical properties of solids are often discussed in terms of the dielectric function [$\varepsilon(\omega) = \varepsilon_1(\omega)+\varepsilon_2(\omega)$], that is introduced along with its relation to other optical response functions in Chapter. 3.2. The dielectric function spectra of C_{60} shows the molecular vibrations below 0.3 eV (see Fig. 2.10). The near infrared (NIR) spectrum of the neutral C_{60} is almost featureless while that of anions carry information about the electronic transition between the split LUMO levels due to the presence of additional electrons. This region of the spectra also covers the weak but complex vibronic structure arising from the nature of Jahn-teller effect in fulleride ions. Above 2.5 eV the symmetry-allowed optical transitions are observed. Beyond 7 eV, the

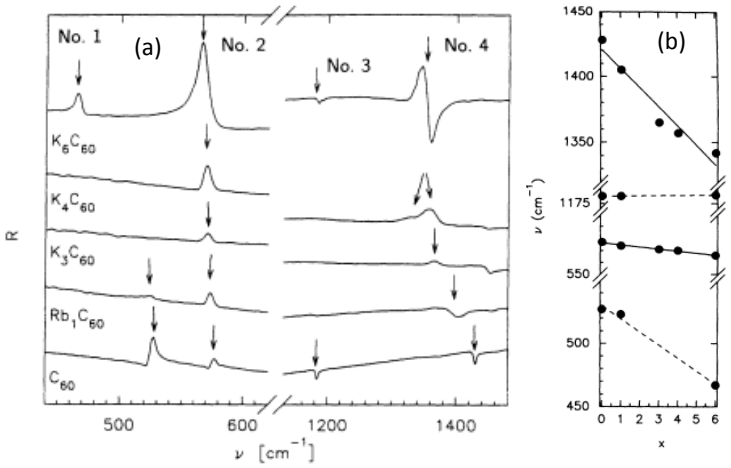

Figure 2.11.: (a) Reflectivity of stable phases of C_{60}, Rb_1C_{60}, K_3C_{60}, K_4C_{60} and K_6C_{60} at room temperature. (b) Frequency shift of corresponding T_{1u} vibrational modes for different valence state x [55].

data from the energy loss spectroscopy studies (see Fig. 2.10) show the higher energy excitations. The electronic properties of the solid fullerides are closely related to the isolated molecules.

The vibrational modes of the C_{60} can serve as a marker to estimate the charge of the doped fullerides. Fig. 2.11 shows the development of the vibrational spectra of C_{60} for different alkali doping at ambient conditions [55].

Within this project orientational ordering, Jahn-Teller effect, insulator-to-metal transitions are the main investigated phenomena on fullerene-based compounds. To probe the consequence of JT effect by spectroscopic technique is not an easy task as most of the C_{60}-based material undergoes a variety of phenomena. Thus, the spectrum has to be analyzed carefully to understand the JT effect on fullerides in addition to the effects of the solid-state environment.

3. Experimental methods

3.1. Introduction

In this chapter, an introduction to the optical response functions and its relation to the measured infrared quantities are presented. The main technique involved in this project is high-pressure infrared spectroscopy and hence a detailed description of all aspects of the high-pressure measurements are given in section 3.3 and infrared spectroscopy is discussed in section 3.4. The models used for the analysis of the infrared data are also discussed. Furthermore, a brief introduction of ATR-FTIR spectroscopy is give as it was used for characterization of the sample.

3.2. Basic concept of infrared spectroscopy

Spectroscopy is a powerful tool to study properties of matter through the interaction of light. By the use of infrared spectroscopy, the microscopic carrier dynamics and electronic structure in organic and inorganic compounds with strong electron correlations can be probed. A variety of phenomena can be addressed by infrared spectroscopy such as low-energy states, impurity levels in semiconductors, interband transitions, resonance, and superconducting gap transitions. Atoms and molecules undergo motions having characteristic energies and when light interacts with these motions it provides information about them. As the light falls on the sample, it causes the charges in the medium to oscillate and hence emits additional light waves that can travel in all direction. Measuring this light can provide a great deal of information about the properties of the sample. Optical experiments of reflectivity, transmission, and refraction provide the way to determine the dielectric function of solid, which is related to the band structure.

From the infrared measurement, complete optical response of the sample can be deduced. The optical response functions related to the properties of material such as the complex dielectric function $\varepsilon(\omega)$, the complex optical conductivity $\sigma(\omega)$ or the fundamental excitation frequencies are introduced briefly in this subsection. These functions can be deduced from the Maxwell's equation with an assumption that the

charge density is zero and are written as [56]:

$$\varepsilon_1(\omega) = n(\omega)^2 - k(\omega)^2 \tag{3.1}$$

$$\varepsilon_2(\omega) = 2n(\omega)k(\omega). \tag{3.2}$$

$$\sigma_1(\omega) = \frac{\omega}{4\pi}\varepsilon_2(\omega) \tag{3.3}$$

and

$$\sigma_2(\omega) = \frac{\omega}{4\pi}(\varepsilon_\infty - \varepsilon_1(\omega)). \tag{3.4}$$

where $\varepsilon_1(\sigma_1\ )$ and $\varepsilon_2(\sigma_2)$ are the real and imaginary parts of the dielectric fuction (optical conductivity), respectively.

The complex dielectric function is related to the complex optical conductivity by the expression

$$\tilde{\varepsilon}(\omega) = 1 + \frac{4\pi i}{\omega}\tilde{\sigma}(\omega). \tag{3.5}$$

The dynamical conductivity σ(q,ω) is the linear response function that relates current density to the electric field. The optical conductivity [$\sigma(\omega)$] can be defined as the response of the material to electromagnetic waves with wavelengths much longer than the characteristic length scales of the condensed electronic systems. The dissipation of electromagnetic energy in the medium is given by the real part of the optical conductivity $\sigma_1(\omega)$ and the screening of the applied field is given by the imaginary part $\sigma_2(\omega)$. The complex index of refraction of the medium N is represented by $N = \sqrt{\varepsilon} = n + ik$, where n is the refractive index and k the extinction coefficient. The Kramers-Kronig relation connects the real and imaginary parts of complex functions such as dielectric function, optical conductivity, or refractive index [56]. In infrared spectroscopy it is not possible to directly measure the optical response function such as n, k, σ_1, or ε_1. The possible measurable quantities are the reflectivity R and transmission T.

Transmission

The transmission or transmittance (T) of the samples can be obtained by the ratio of intensity of the beam transmitted by the sample (I_s) to that of the reference (I_r) as given by:

$$T(\omega) = I_\mathrm{s}/I_\mathrm{r} \tag{3.6}$$

Reference (I_r) is the light transmitted through the same optical path of the measurement without the sample. Generally, transmittance data is converted into absorbance (A) for performing further analysis by using the relation:

$$A(\omega) = -log_{10}T(\omega)$$

Absorbance of the light by the sample can be quantified by absorption coefficient (α). It is defined as the fraction of the light absorbed in a unit length of the medium. If the light is propagating through a medium of thickness z, then the intensity is $I(z)$. The intensity of the beam decreases with increasing thickness of the medium. According to the Beer's law, $I(z)$ can be written as:

$$I(z) = I_0 e^{-\alpha z},$$

where I_o is the intensity at $z = 0$. The absorption coefficient is related to imaginary part of the refractive index (k) by the relation

$$\alpha = \frac{2\omega}{c}k \tag{3.7}$$

In the latter part of the thesis, the relation between the absorption coefficient (α) and the optical conductivity will be used and it is given by

$$\sigma_1(\omega) = \frac{nc}{4\pi}\alpha. \tag{3.8}$$

Reflection

Reflectivity $R(\omega)$ can be defined by the ratio between the intensity reflected by the sample (R_s) to that reflected from a reference (R_r)

$$R = \frac{R_\mathrm{s}}{R_\mathrm{r}} \tag{3.9}$$

In case of the free standing sample, a 100 % reflecting mirror (silver or aluminium) can be used as reference (R_r). $R(\omega)$ is related to the complex index of refraction (N) and therefore n and k according to Fresnel's equation is given by;

$$R(\omega) = |\tilde{r}|^2 = \frac{(n-1)^2 + k^2}{(n+1)^2 + k^2}, \tag{3.10}$$

where $\tilde{r}$ is the reflection coefficient. This relation holds good when the reflectance is measured at the sample-vacuum interface.

Any spectroscopic technique is best utilized in combination with external tuning parameter such as pressure, temperature or magnetic field. The main external tuning

parameter in this project is high pressure. Spectroscopy under high pressure can be used to determine the equation-of-state of materials. The pressure induced shift of the optically active electronic transition can directly provide information about its nature. The high pressure technique is itself a vast field. Some important technical details related to the high pressure experimental methods will be discussed in the next section.

3.3. High pressure technique

High pressure technique originally developed for geophysical research is now a very important method in condensed matter physics research. Diamond anvil cells (DAC) enable us to achieve pressure range of gigapascals in the laboratory, which matches the characteristic electronic and magnetic energy scale in a broad range of materials. By external pressure application, the lattice is compressed and a variety of phenomena can be tuned such as insulator-to-metal transition, orientational ordering, etc. External pressure application is a clean way to study material properties compared to chemical substitution. In the upcoming section, all details related to DACs required for high-pressure infrared spectroscopy are presented.

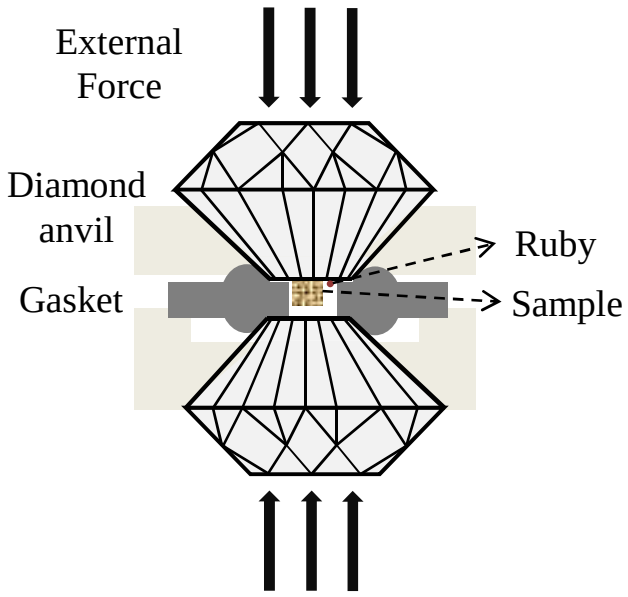

Figure 3.1.: Schematic representation of the working principle of a DAC.

3.3.1. Diamond anvil cell

The diamond anvil cell is a simple device that allows application of pressure on samples. The transparency of diamond over a broad frequency range in the electromagnetic spectrum permits sophisticated measurements using the DAC, *e.g.* X-ray diffraction on powder and single crystals and optical spectroscopy.

A DAC essentially consists of a pair of diamonds which are held tight with its anvils aligned perfectly parallel to each other. The underlying principle of the DAC is illustrated in Fig. 3.1. A metallic plate (gasket) with a small hole is placed between two opposite diamonds which serves as a sample chamber. The basic physical relation between pressure (P), force (F), and area (A) [P = F/A] is employed in working of DAC. A sample is placed in the gasket hole and the flat faces of two opposite diamond anvils are forced towards each other to create high pressure. The large ratio between the area of external and internal face of the diamond multiplies the effect of the applied force, leading to high pressure on the sample. The gasket exerts a force that compensates the internal pressure which prevents failure of anvil and sample loss.

Diamonds

The commercially available diamond anvils are made from the gem-quality and inclusion free single crystals with low birefringence (low internal strain). These diamonds usually have 8 or 16 faces, and the working plane is produced at the anvil flat named culet. The culet is usually set parallel to the (100) or the (110) plane of the diamond [57]. The choice of diamonds and their size for the DAC depend on the maximum pressure to be achieved and the nature of investigation. Diamond anvils can also be replaced by various gem anvils, for example cubic zirconia and sapphire anvils can achieve pressure up to 16.7 GPa and 25.8 GPa, respectively [58].

Natural diamonds contain a significant concentration of defects which can dramatically affect their optical properties. The rarely occurring Type IIa diamonds are pure form of natural diamonds. They are almost free of impurities, which make them colorless and transparent in a broad range of the infrared spectrum. The transmission and reflectivity of diamond is constant from the far infrared (FIR) to the visible range with an exception in the spectra range between 1700 to 2700 cm^{-1}, where strong multiphonon absorptions are present as shown in Fig. 3.2. Hence this region of the data should be ignored. The refractive index of diamond is taken to be nearly constant except for this spectral range.

The maximum pressure that can be reached by the DAC depends on several factors [59]:

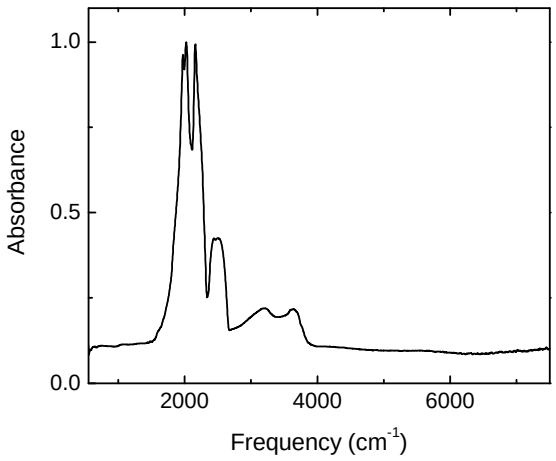

Figure 3.2.: Multiphonon absorbance of diamond in the midinfrared (MIR) region.

- culet size - the smaller the culet diameter, the higher is the pressure that can be achieved,
- gasket material - harder material helps to achieve high pressure range,
- quality of gasket hole - it has to be made without burrs, to avoid instability.

Different pressure ranges either in few tens of Pa or tens of GPa can be easily achieved with suitable choice of DACs in the laboratory.

There are three main mechanisms governing the proper working of the DAC [60]: (i) Mechanism of alignment: Perfect alignment of the anvil is very important due to brittleness of the diamond. A good alignment is achieved with the help of the translational and/or tilting screws. To align the diamond perfectly parallel to each other, the diamonds are placed directly on top of each other and the tilting screws are adjusted while viewing the DAC under the optical microscope until the air wedge (interference fringes) disappears between the diamond. (ii) Guiding system: The piston-cylinder mechanism is employed in many types of DACs. The piston should fit well in the cylinder with a tolerance of $\sim$5 μm, to avoid swinging of the anvils. Care has to be taken to keep this area free of any sample or dust particles. (iii) Load application mechanism: DACs can be classified based on how the load is applied to the DAC such as clamped cells, pneumatic or hydro-loading cells, and lever-arm driven ones. Various types of DACs have evolved based on the method of pressure generation and anvil alignment mechanisms. For instance, NBS cell [61], Basset cell [62], Mao-Bell cell [63], Syassen-Holzapfel cell [64], Merrill-Basset cell [65].

3.3.2. Gasket material and preparation

The use of gasket for containment of the hydrostatic pressure medium was first introduced by Van Valkenburg [66]. Gaskets are indented by pressing it in between the anvils to a desired thickness (75-85 μm) depending on the pressure range to be achieved and the pressure transmitting medium to be used. Indentation has the following advantages:

1. easy loading of the cell,
2. separating the two delicate operations of centering the gasket hole and positioning the sample in the diamond face,
3. avoid large deformation, and
4. stability of the hole.

A sample hole is drilled in the center of the indentation with the help of a EDM (Electric Discharge Machine). Tungsten carbide rods of various diameters are used as the needles to drill the hole in the indented gasket. The purpose of EDM is to precisely center the hole to be drilled on the gasket. The gasket with the hole is placed on the lower diamond for filling with samples, with the same orientation as it had when making the indentation. For relatively incompressible media like argon, the hole may be made one-third to two-fifth of the culet diameter as it may slightly shrink during pressure application. On the other hand, with the use of helium as pressure transmitting medium, the hole shrinks by a factor of two or more. To avoid damage to the sample, the hole can be made larger. During pressure application, the part of the gasket between the culets undergo plastic deformation as the diamonds advance. The hydrostatic pressure within the metal decreases linearly in the direction of extrusion. Extrusion may be entirely outwards or inwards collapsing the sample hole during the experiment, which is an highly undesirable situation. Also any initial asymmetry such as non central hole, non parallel culets can cause the failure of the gasket.

For this project, the gaskets used were CuBe and stainless steel for Cryo DAC mega and Syassen–Holzapfel DAC, respectively. CuBe sheet with initial thickness of 360 μm was used to reach pressures up to 10 GPa with Cryo DAC Mega and stainless steel sheets of thickness 200 μm to reach pressures up to 20 GPa with Syassen DAC. The indentation thickness of the gaskets were in the range 75-90 μm. The hole sizes on CuBe gaskets were 300-400 μm and in case of stainless steel were in the range 120-200 μm which is determined based on the culet size of the DAC (for more detail see Sec. 3.3.4).

3.3.3. Pressure transmitting medium

A medium is required to transmit the external thrust applied on the DAC to the sample as uniform stress. It is necessary that the medium provides hydrostatic pressure on the material under investigation, so as to record accurate intrinsic material properties. The choice of the pressure transmitting medium is done taking into account the following criteria: chemical inertness, good hydrostaticity, zero shear strength, zero compressibility, non penetrative, low viscosity, and transparency in the measured spectral region. Various solids, liquids, and gases are being used as pressure transmitting medium, for example, silicon oil, nitrogen, helium, CsI, etc. The pressure transmitting media used in this project are CsI, NaCl, argon and helium.

3.3.3.1. Filling of the DAC

The sample is filled in the DAC after careful cleaning of the diamond and gasket. The gasket with the hole is glued to the seat of the lower diamond. The sample and ruby balls are placed in the diamond face carefully, followed by the pressure transmitting medium.

The solid pressure medium like CsI are ground into fine powder and filled over the sample and the ruby ball in the gasket hole. All measurements on air sensitive samples were carried out using CsI and filling of the DAC was done inside the glove box. CsI which had to be used inside the glove box was pretreated for 3 hours at 200° C under dynamic vacuum in order to remove air and any traces of moisture as it is hydroscopic.

For fillings with cryogenic liquid, the DAC can be immersed in the cryogenic fluid for trapping the condensed gas. The filling of liquid helium or liquid argon into the sample chamber of the DAC needs specially designed equipments and a facility that incorporates remote sealing of the DAC.

3.3.3.2. Cryogenic pressure transmitting medium and loading in the DAC

The noble gas argon can be used for high pressure infrared experiments as pressure transmitting medium. But it has a limitation of low solidification pressure (1.4 GPa at 300 K) [67]. Recent works have suggested a hydrostatic limit of 1.9–2 GPa [67,68] against the previous claim of 9 GPa [69].

Argon is filled in DAC with the help of a home-built cryogenic-filling setup. After placing the sample and ruby balls in the DAC, it is partially closed so that the fluid medium can flow in and fill the sample chamber. The gaseous argon is passed into a metal tube that is immersed in liquid nitrogen so that the gaseous argon can be liquefied. The DAC can be sealed by a remote access mechanism after it has remained in

liquid argon for about 5 minutes to ensure that argon has entered the sample chamber. The DAC is then taken out of the setup once it reaches the room temperature.

Helium is the best pressure transmitting medium even as a solid above 12.1 GPa at 300 K. The pressure gradient measured on many ruby balls filled in the DAC with helium as pressure medium was nearly none up to ∼23 GPa and has a deviation of only 0.4 % for higher pressures up to 40 GPa [67]. Unfortunately helium poses a very important limitation due to its diffusion into diamond anvils which can lead to embrittlement and eventually failure of the anvils. [70].

Filling helium in the DAC is laborious procedure compared to the argon filling. Filling helium in the DAC was done with a bath cryostat which essentially consists of a vacuum and a liquid nitrogen shield. When the liquid helium rises above the DAC, it can be sealed with the help of the mechanical remote access system. The DAC can be retrieved when the cryostat reaches the room temperature.

3.3.4. DACs used for this project

Syassen–Holzapfel type DAC and CryoDAC Mega were used for high-pressure infrared measurements within this project. The working principle of both these DAC are very similar. The air sensitive samples were measured with CryoDAC Mega as it is relatively easier to handle this DAC inside the glove box due to the working distance of the microscope in it. Both DACs are described in the following sections.

3.3.4.1. Syassen-Holzapfel type DAC

It is a piston-cylinder type high pressure cell designed by Syassen and Holzapfel [64]. Photos of this DAC are shown in Fig. 3.3. One of the diamonds is mounted on the piston part with tilt adjustments for diamond alignment. The other diamond is fixed on backing plate that has a x-y translational stage. The force is applied onto the diamonds with the help of thread-and-knee mechanism. Two threaded rods connect the front and back sides of the brackets. By concurrently turning these rods, the clamps thrust the piston into the cell body and decreases the distance between the anvils to generate the required pressure. The special geometry of brackets, levers and threads results in generation of very high pressure. This DAC has an excellent alignment stability due to the well fitting combination of the long piston and cylinder, as the cylinder directs the movement of the piston strictly parallel to its axis. The numerical aperture on the backing plate side is 36° and that of the piston side is 24°. Optical measurements are performed on the backing plate due to the large numerical aperture and narrow depth of field. The diamonds used in this DAC are type IIa with

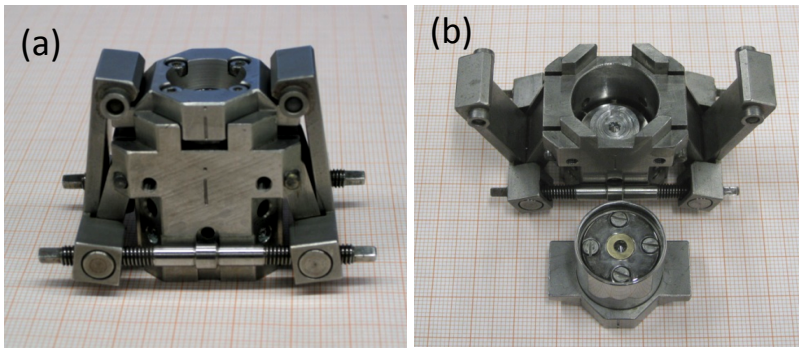

Figure 3.3.: Photo of Syassen-Holzapfel DAC (a) closed DAC and (b) opened DAC showing both diamonds.

a height of 1.5 mm and culet size of 400 μm. A maximum pressure of about 25 GPa can be achieved with a stainless steel gasket.

3.3.4.2. CryoDAC Mega

The CryoDAC Mega is a non magnetic DAC which is appropriate for optical and X-ray diffraction measurements. As the numerical aperture is high (50°), this DAC is well suited for FTIR spectroscopy. A photo of the DAC along with its parts is shown in Fig. 3.4. The diamond anvils are mounted within the force fitted CuBe rings and are mechanically fixed to the tungsten carbide support plates, thereby avoiding the use of epoxy resins or other adhesives which are not reliable at low temperature. The DAC itself is held within two CuBe blocks as seen in the Fig. 3.4 (c). The piston-cylinder assembly can be fixed to the CuBe body by means of screws. Load is applied with the help of four Â$\frac{1}{4}$ inch UNF [1] cap head bolts. The DAC has to be checked for anvil alignment after few high-pressure measurements. To align the diamonds perfectly parallel to each other, the top diamond is provided with three screws for tilt adjustments. The culet diameter is 600 μm and a maximum pressure of 9 GPa can be achieved with the use of CuBe gasket. The length of the complete assembly is 38 mm. The gaskets are indented to a thickness of about 80 μm and holes of diameter 400 μm can be made to reach pressure up to 8 GPa. The larger hole size makes sample loading relatively easy.

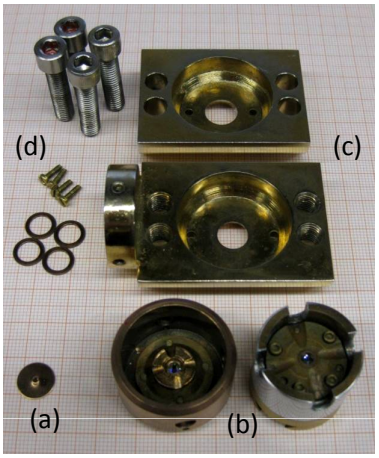

Figure 3.4: A photo of Cryo-DAC showing its parts (a) CuBe gasket, (b) piston-cylinder with diamonds, (c) body of the DAC, and (d) screws for clamping the cell.

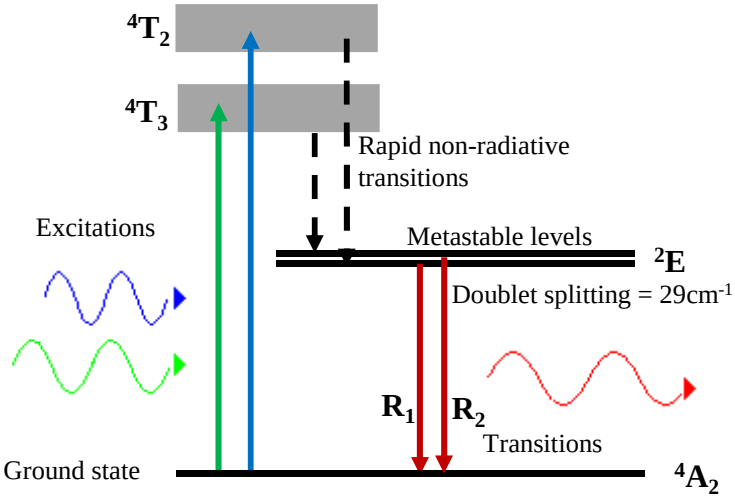

Figure 3.5.: Energy levels of Cr^{3+} of ruby crystal.

3.3.5. Ruby scale for pressure calibration

The ruby fluorescence method was invented by Forman [71] in 1972. The use of ruby fluorescence technique for pressure determination inside the DAC became a convenient method after further research by Barnett *et al* [72] and Piermarini *et al.* [61]. Ruby balls of size 20-50 μm were used in this work. Ruby is Cr^{3+} doped corundum crystals with free Cr^{3+} ions that contain three electrons in the 3d shell. Ruby crystal has a strong crystal field that leads to a cubic and trigonal splitting of the energy levels. At room temperature, all electrons are in the ground state A_2. Fig. 3.5 shows the energy levels of chromium ions in ruby. When the ruby is illuminated with green laser (λ=523 nm and power of 6 mW) the electrons get excited to T_2 and T_3 levels, which undergo

[1]UNF(Unified National Fine Thread Series) is the American standards for fine thread

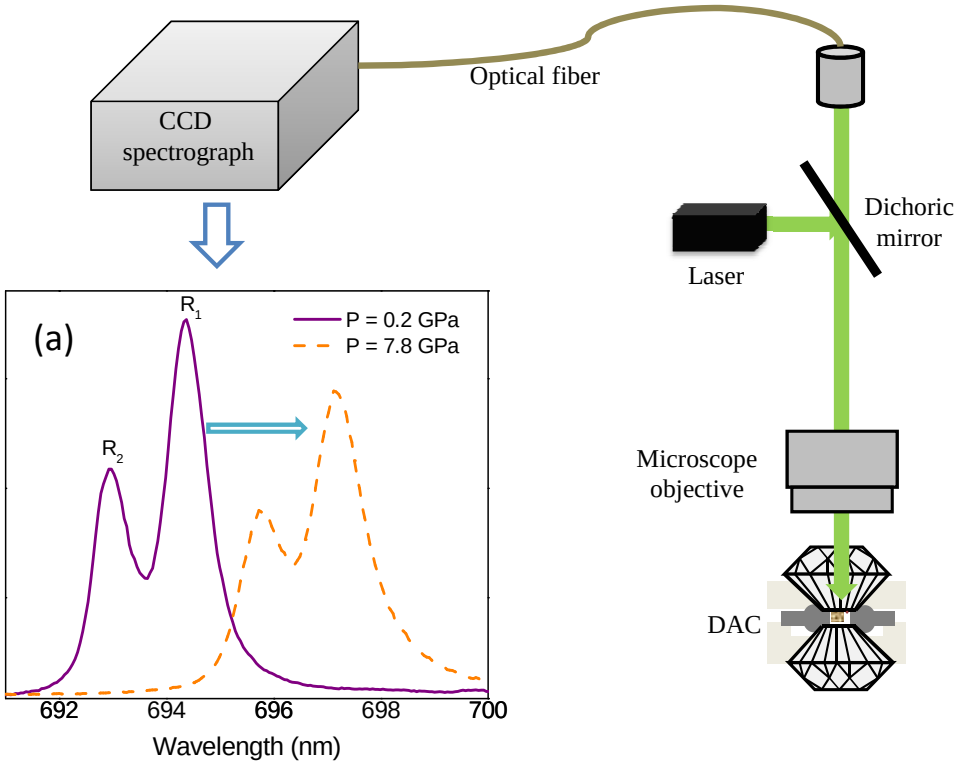

Figure 3.6.: Schematics of ruby luminescence setup used for pressure calibration. The graph shows the luminescence spectra of ruby excited by green laser for selected pressures at room temperature.

fast non-radiative decay to the metastable ^{2}E level. From this level, the electrons relax to a lower energy level with the emission of characteristic radiations, R_1 and R_2 lines at 694.2 nm and 692.8 nm, respectively at ambient conditions. On application of pressure on the ruby, the lattice compresses and reduces the Cr and O ion distance. This affects the energy level splitting causing a decrease in the energy gap between ^{2}E and the ground state. This in turn shifts the R_1 line linearly to higher wavelength, with a coefficient $dP/d\lambda = 2.746$ kbar Å^{-1} or $d\lambda/dP = 0.364$ Å kbar^{-1}. The R_1 and R_2 lines shift is also temperature dependent. In the temperature range 120 – 300 K the R_1 and R_2 lines show a linear temperature dependence with a shift of 0.0068 nm/K. Mao *et al.* [63] calibrated ruby fluorescence up to 100 GPa in a non-hydrostatic medium. For pressures below 30 GPa, it can be assumed that the pressure-dependent line shift can be described by the equation:

$$P(d\lambda) = \frac{A}{B}\left[\left(1 + \frac{d\lambda}{\lambda_o}\right)^B - 1\right], \tag{3.11}$$

where A = 1904 GPa, B = 7.665, $d\lambda$ is the shift in the frequency of R_1 line with

increasing pressure, and λ_o is the wavelength at ambient pressure (694.23 nm at 298 K).

In order to determine the pressure generated in the DAC *in-situ* during the experiment, a high resolution charge coupled device (CCD) spectrograph was coupled to the IR microscope via an optical fiber as shown in Fig. 3.6. The MS260i^{TM} CCD spectrograph is a commercial grating-type imaging spectrograph with asymmetrical in-plane Czerny-Turner optical configuration. The spatial resolution of the spectrograph is about 40 μm.

A solid-state laser is directed through dielectric-Coated Plane Mirror (532 nm) towards the DAC placed under the infrared microscope. The dichoric mirror acts as a color filter, with maximum reflection in the range 480–600 nm and transmits light of other wavelengths. The green laser is reflected by the dichoric mirror mounted in the special assembly on the IR microscope and illuminates the ruby in the DAC. The characteristic lines of the ruby is transmitted by the mirror towards the CCD spectrograph. In the luminescence spectrum, the position of the R_1 line is fitted with Lorenztian function to precisely extract the peak position. A Java applet is used to calculate the corresponding pressure with the formula from Eq. 3.11. The accuracy of pressure determination with this setup is about 0.1 GPa.

Now with this detailed information regarding the high pressure technique, the main spectroscopic technique used for this project namely the infrared spectroscopy will be discussed. Also the aspect of combining the high pressure technique with infrared spectroscopy will be presented.

3.4. Fourier Transform Infrared spectroscopy

3.4.1. Principle of FTIR

The FTIR is typically based on the Michelson interferometer designed by Michelson in 1891. The working principle of the interferometer is illustrated in Fig. 3.7. The interferometer consists of a beamsplitter, fixed and moving mirrors. The beamsplitter is made of a special material which can partially transmit and partially reflect the incident radiation. The radiation from the source falls on the beam splitter which splits the beam into two paths. The beam gets reflected back from the moving mirror and the fixed mirrors on to the beamsplitter, with an optical path difference. These beams recombine to produce an interference and then the beam passes through the sample and falls on the detector. A plot of light intensity *versus* optical path difference is called an *interferogram*. The interferogram can be converted to frequency domain (the spectrum is signal as a function of frequency) using Fourier transform (FT). The

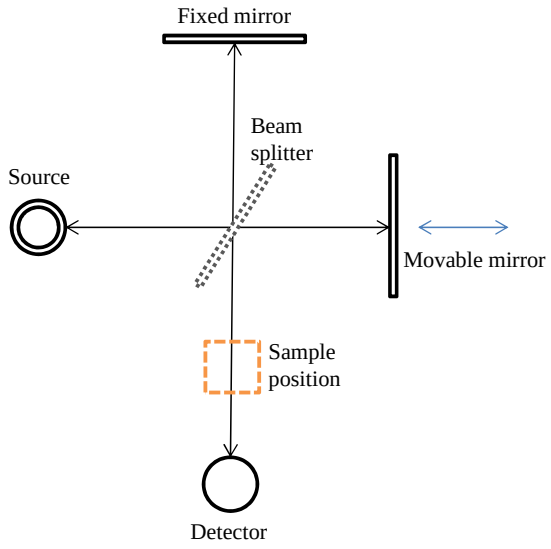

Figure 3.7: Schematic diagram of Michelson interferometer.

interferogram obtained by FTIR and the converted spectrum using FT is illustrated in Fig. 3.8. Almost all modern IR spectrometer are FTIR.

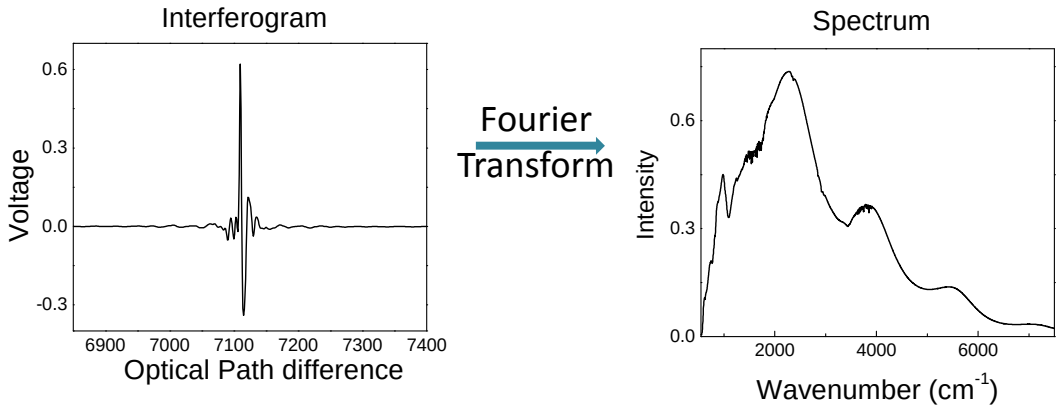

Figure 3.8.: Conversion of interferogram to spectrum by Fourier transformation.

3.4.2. FITR Bruker 66 v/S

The layout of Bruker IFS 66 v/S is shown in Fig. 3.9. The infrared frequency spans a section of electromagnetic spectrum from 10 – 12000 cm^{-1} and visible region from 10000 – 24000 cm^{-1}. The various frequencies can be realized with various combinations of source, detectors, and beam splitter. The frequency range between 10 – 700 cm^{-1} which is generally referred to as far-infrared region can be realized with a Hg discharge lamp and mylar beam splitter. A silicon-based helium cooled bolometer is used as the

detector for this range mounted at the detector position 3. The mid-infrared range (500 – 8000 cm^{-1}) can be achieved with globar source, KBr beam splitter and MCT (liquid nitrogen cooled) detector. The detector compartment contains two detector positions as in Fig. 3.9, one for the liquid nitrogen cooled MCT/InSb (detector 2 position) detectors and another for DTGS (FIR/MIR) detector (detector 1 position) which works at room temperature. The high frequency range can be covered with tungsten lamp as source and CaF_2 beam splitter. Liquid nitrogen cooled InSb is used as the detector for the NIR region from 2000 – 12000 cm^{-1}. The visible region from 10000 – 26000 cm^{-1} can be measured using Si diode and GaP detectors that works at room temperature. Bruker IFS 66 v/S works under vacuum in order to eliminate the water vapor and carbondioxide absorption during measurement. The Bruker spectrometer is vented with nitrogen purge.

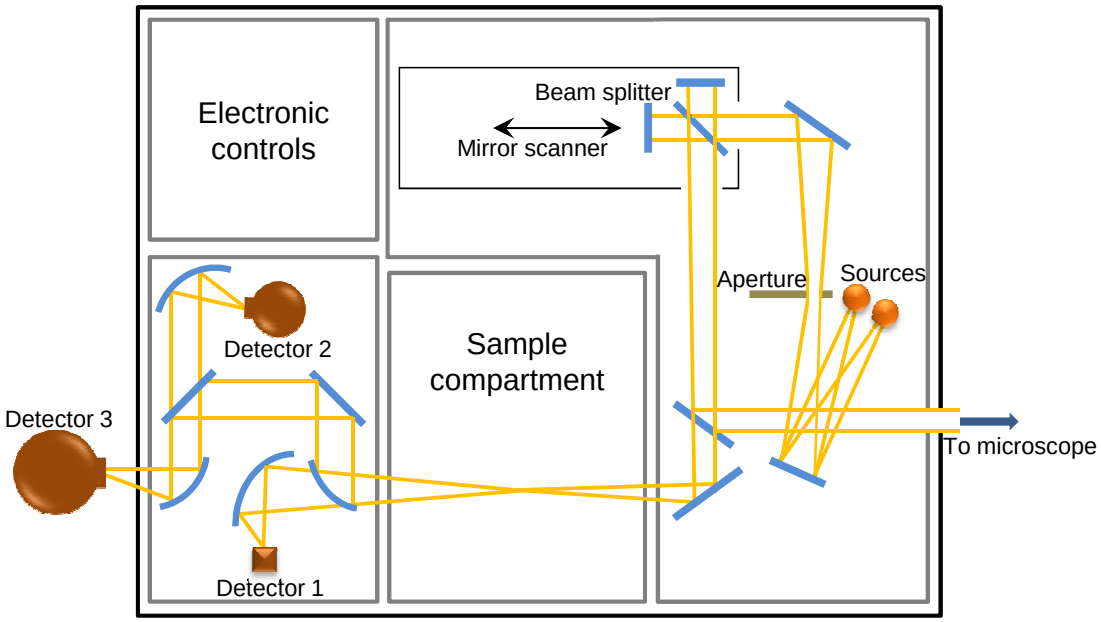

Figure 3.9.: Optical layout of Bruker IFS 66v/S spectrometer.

3.4.3. Infrared micro-spectroscopy for high pressure studies

For carrying out high pressure measurements, the spot size of the beam in the spectrometer is too large to be focused on the sample in the DAC (sample size ∼100–200 μm). Therefore, an infrared microscope (IR scope II) which can produce smaller spot size, of the order of the sample size in the DAC, is coupled to the spectrometer. The

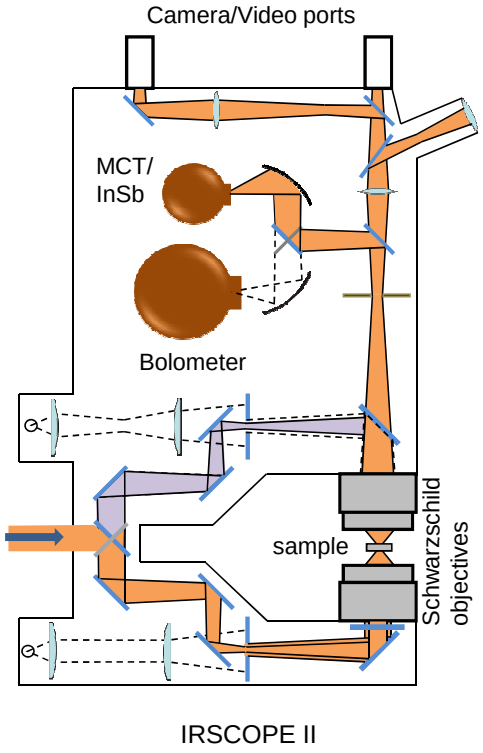

Figure 3.10: Optical layout of the IR Scope II that can be connected to the Bruker IFS 66 V/s spectrometer. Orange beam path shows the transmission path and the violet shows reflection path only in the region that differs from the former.

IR scope II has a pair of Schwarzschild IR objectives with 15× magnification and viewing objective of 4× magnifications. As lenses cannot be used in the infrared region all-reflecting optics are used such as the mirrors or the Schwarzschild objective which is also known as Cassegrain objective. The Schwarzschild objectives are positioned on the top and bottom of the sample stage. The top objective is used to focus the beam on the sample and the second one serves as the condenser during transmission measurements. The Schwarzschild objective is a convex-concave mirror system that can eliminate spherical aberration, coma, and astigmatism. The optical beam path of the microscope is illustrated in Fig. 3.10. The entire infrared beam path in the microscope is purged with nitrogen to avoid absorption due to water vapor and carbondioxide. The microscope can be operated both in reflection and transmission mode from FIR to visible range. The low frequency limit depends on the size of the sample. The resolution limit due to diffraction is given by Rayleigh's relation:

$$\Delta r = \frac{0.66\lambda}{sin\theta/2}$$

where Δr is the lateral resolution, λ is the wavelength of light, and θ is the full opening angle of the objective [73]. According to this relation, the Syassen-Holzapfel cell has a lower bound for frequency around 150 cm^{-1} for a sample size of 100 μm.

The CryoDAC Mega can accommodate a bigger sample ($\sim$ 200–250 μm) due to its large culet size, thus extending the low frequency limit down to 100 cm^{-1} depending on the sample size. The diameter of the infrared beam can be varied between 20 and 200 μm by standard apertures. The IR microscope has a visible lamp to examine the sample. A camera/video port is positioned on the top of the microscope and a port to collect the ruby luminescence signal during pressure calibration (see section 3.3.5 for more details). All high-pressure measurements in this project were carried out with Bruker IFS 66 v/S coupled to the IR scope II.

3.4.4. Transmission and reflection measurements as a function of pressure

High pressure infrared measurements can be performed either in transmission or reflection mode depending on the sample type and form.

Transmission

The transmittance (T) of the samples in DAC can be obtained from the same formula introduced earlier,

$$T = I_{\mathrm{s}}/I_{\mathrm{r}} \tag{3.12}$$

In case of high pressure measurements, the reference is usually measured through the DAC filled with pressure transmitting medium. While carrying out transmission measurements, the important issue to be address are the interference fringes. Interference is caused by the multiple reflections within the DAC. However, sometimes it is difficult to get rid of these fringes during the measurement and also by post treatment as they are pressure dependent (*i.e.* the distance between the two diamond faces decrease with pressure and thus the fringes). The fringes are more pronounced in the lower frequency region. Care can be taken to minimize the effect by measuring the reference for every sample measurement.

Reflectivity

High-pressure reflectivity measurements with the DAC is not straight forward as the transmission measurements. The Fresnel's equation introduced earlier holds good for vacuum-sample or sample-air interface, whereas in case of high pressure measurements, the sample-diamond interface has to be taken into account. Thus near normal incidence

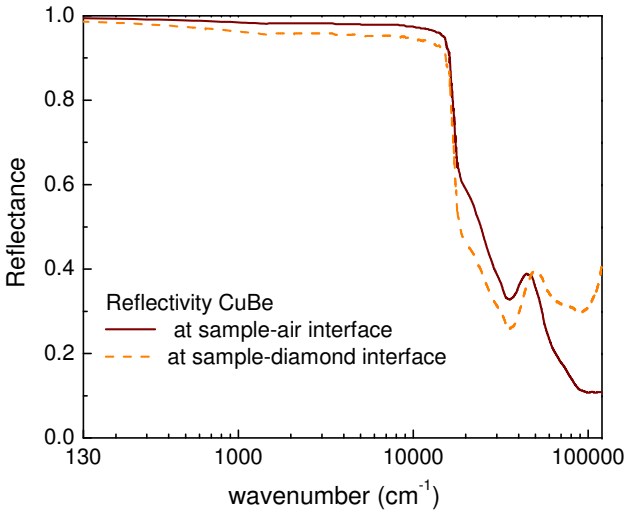

Figure 3.11.: Infrared reflectivity of Cu in air [74] and the simulated reflectivity of Cu inside the DAC (at sample-diamond interface) in a broad frequency range.

reflectance of a sample with respect to the diamond (refractive index n_{dia}) is given by the modified Fresnel's equation;

$$R(\omega) = |\tilde{r}|^2 = \frac{(n - n_{dia})^2 + k^2}{(n + n_{dia})^2 + k^2}.$$

Hereafter, any reference to $R(\omega)$ denotes the sample-diamond interface. All high-pressure reflectivity measurements for this project were carried out with CyroDAC Mega in the FIR and MIR frequency range. The gasket material for this DAC is CuBe and Copper has a constant reflectivity up to 12000 cm^{-1}, as shown in Fig. 3.11. A clean spot on CuBe gasket inside the DAC can be measured as the reference (I_r). This method holds good only with the use of CuBe as gasket material in the DAC.

3.4.5. Drude-Lorentz model

The analysis of the measured reflection or transmission spectra are done in terms of the dielectric function using the Drude-Lorentz model for this project and additionally a Fano approach is applied to the reflectivity spectra of Rb_4C_{60}. Drude-Lorentz model gives the linear response functions of both metals and insulators as sum of several contributions related to different charge excitations, lattice vibrations, etc. The Drude term explains the response of the electron in a metal to the electromagnetic radia-

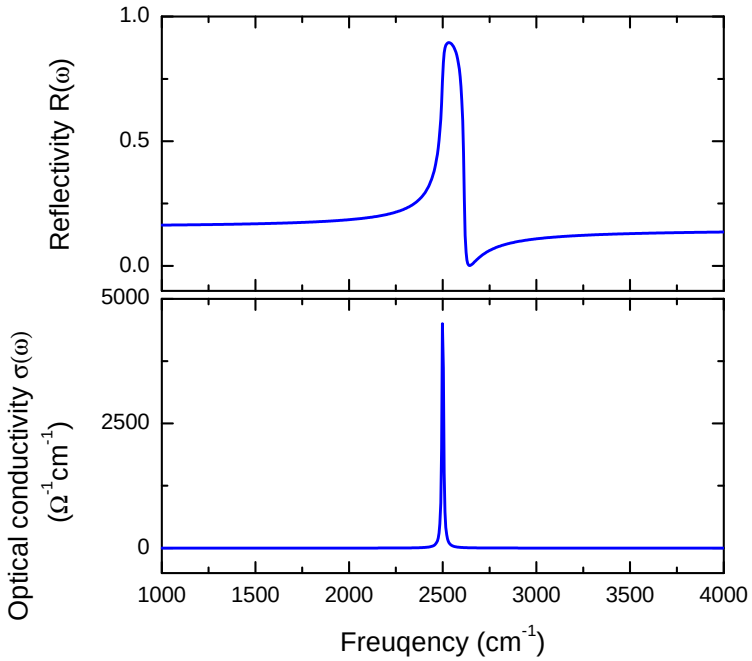

Figure 3.12.: Frequency-dependent reflectivity and corresponding real part of the optical conductivity calculated using the Lorentz model.

tion. The Lorentz term describes the response of the localized carriers. In general experimental infrared spectrum of insulator or semiconductor containing phonons and interband transitions can be described with the Lorentz model. The metallic spectrum is described with the help of a Drude oscillator in the low frequency region.

Lorentz oscillator model

Lorentz oscillator model is purely classical and elegant tool to visualize atom-field interactions although it is the simplest picture. According to the theory the atoms vibrating in the solids can be represented by a series of damped oscillators. The valence electrons are bound to the specific atoms in the solid by Coulombic attraction (harmonic forces). This Coulomb force tends to restore the valence electrons into specific atomic orbital. Thus, solids can be considered as a collection of atomic oscillators. These atomic oscillators would have their characteristic natural frequency (ω_o) resulting in a resonance process. The motion of a valence electron bound to a nucleus can be written by the expression [75].

$$F = e(\mathbf{E} + v \times \mathbf{B}) \tag{3.13}$$

The effect of magnetic field **B** is negligible and therefore it is typically dropped out from analysis for non relativistic light field. Thus the motion of the electron bound to the nucleus is described by the Lorentz model for harmonic oscillator which is written as:

$$\mathrm{m}\frac{d^2\mathbf{r}}{dt^2} + \frac{m}{\tau}\frac{d\mathbf{r}}{dt} + m\omega_0^2\mathbf{r} = \text{-e}\mathbf{E}(t) \tag{3.14}$$

where **r** is the position vector of the electron, $\gamma = 1/\tau$ is the damping effects, m is the mass of the electron, ω_0 $(= \sqrt{K/m})$ is the natural frequency, and e is the charge of the electron. The harmonic term by the Hooke's law is given as $\mathrm{m}\omega_0^2\mathbf{r}$, which gives the restoring force of the valence electron. This term vanishes in case of metal where the electrons are free.

The solution of Eqn. 3.14 can be given by

$$\mathbf{r}(\omega) = \frac{-e}{m}\frac{\mathbf{E}(\omega)}{(\omega_o^2 - \omega^2 - i\Gamma\omega)} \tag{3.15}$$

The permeability $\mu(\omega)$ of the medium is

$$\mu(\omega) = \alpha(\omega)\mathbf{E}(\omega) \tag{3.16}$$

where $\alpha(\omega)$ [2] is the atomic or molecular polarizability and is given by

$$\alpha(\omega) = \frac{e^2}{m}\frac{1}{(\omega_o^2 - \omega^2 - i\Gamma\omega)} \tag{3.17}$$

The atomic polarisability can be related to dielectric constant (ε) with some assumption related to the local field. With N atoms per unit volume, the Lorentz model can describe the frequency response in terms of the material polarization and driving electric field. The complex dielectric function is given by the following expression according to the Lorentz model,

$$\tilde{\varepsilon}(\omega) = 1 + \frac{4\pi Ne^2}{m}\frac{1}{(\omega_0^2 - \omega^2) - i\omega/\tau} = 1 + \frac{\omega_p^2}{(\omega_0^2 - \omega^2) - i\omega/\tau} \tag{3.18}$$

$\omega_p = \left(\frac{4\pi Ne^2}{m}\right)^{1/2}$ describes the oscillator strength.

The complex conductivity follows from the Eq. 3.18 and can be written as

$$\tilde{\sigma}(\omega) = \frac{Ne^2}{m}\frac{\omega}{i(\omega_0^2 - \omega^2) + \omega/\tau} \tag{3.19}$$

[2]Note: atomic/molecular polarizability must not be confused with the absorption coefficient as both are generally denoted by α

In insulators the valence and conduction bands are full and empty, respectively at $T = 0$. The Fermi energy lies between these bands, leading to the zero dc conduction at $T = 0$, and has a finite static dielectric constant. Fig. 3.12 shows the frequency dependent reflectivity and corresponding optical conductivity to illustrate the Lorentz oscillator model.

Drude conductivity of metals

The Drude model considers metals as classical electron gas under motion. The main assumption of the model is that the collision time is independent of the electron's position and velocity. In other words the existence the average relaxation time τ. The optical properties of a complex material could have Drude contribution from free electron in partly filled bands in addition to Lorentz oscillator contributions.

In the presence of the electric field $[\mathbf{E}(t)=\mathbf{E}_o e^{-i\omega t}]$, the motion of a free electron is not bound to a nucleus (i.e., $\omega_0 = 0$) in metals. The derivation of Drude term is analogous to the Lorentz term except that an induced current (J) rather than induced polarization (P) is involved. The Drude model can thus be obtained from the Lorentz model by equating ω_0 to be zero. The equation of motion of free electrons can then be written as;

$$m\frac{d^2\mathbf{r}}{dt^2} + \frac{m}{\tau}\frac{d\mathbf{r}}{dt} = -e\mathbf{E}(t). \tag{3.20}$$

and the dielectric constant for Drude model is given by

$$\tilde{\varepsilon}(\omega) = 1 - \frac{\omega_p^2}{\omega^2 + i\omega\gamma} = \left(1 - \frac{\omega_p^2}{\omega^2 + \gamma^2} + i\frac{\omega_p^2\gamma}{\omega^3 + \omega\gamma^2}\right) \tag{3.21}$$

and the ω_p^2 by definition plays the role of oscillator strength but by convention it is known as plasma frequency and is given by

$$\omega_p^2 = \frac{Ne^2}{m\varepsilon_0} \tag{3.22}$$

N is the carrier density, and m is the effective mass. The width of the Drude term reflects the carrier scattering rate $1/\tau$. Fig. 3.13 shows the Drude reflectivity and its corresponding dc conductivity.

Drude-Lorentz mode

In many complex materials, the combination of Drude and Lorentz terms are needed to describe the complex optical response of various contributions. Therefore various

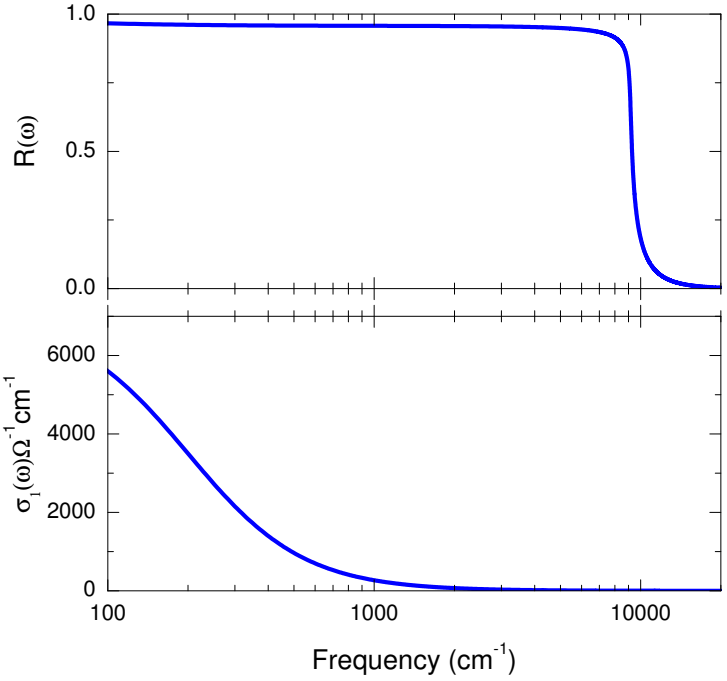

Figure 3.13.: Frequency-dependent reflectivity and respective real part of optical conductivity calculate using the Drude model. The parameter used for the simulation are $\omega_p = 9165$ cm^{-1}, $\sigma_{dc} = 7000$ Ω^{-1} cm^{-1}, and damping = 200 cm^{-1}.

contributions can be summed up to the complex dielectric function of the material and is given by

$$\varepsilon(\omega) = \varepsilon_\infty - \frac{\omega_p^2}{\omega^2 + i\omega\gamma} + \sum_i \frac{\omega_{p,i}^2}{(\omega_i^2 - \omega^2) - i\omega\gamma_i} \tag{3.23}$$

where ε_∞ stands for the dielectric constant at high energy, the second term is the Drude component and the last term is the Lorentz component.

3.4.6. Fano resonance model

According to the Fano theory [76] the interaction of one or more discrete levels with a continuum of states would result in asymmetric optical absorption peaks. After subtraction of the continuous electronic background the Fano profile [77] can be written as

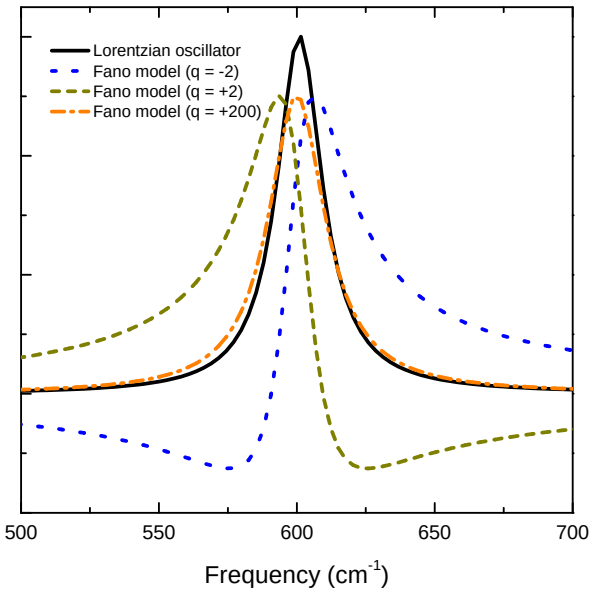

Figure 3.14: Illustration of the Fano line shape in comparison to harmonic lorentz oscillator.

$$\tilde{\sigma}(\omega) = \sum_j i\sigma_{0j}\frac{(q_j + i)^2}{i + x(\omega)}, \tag{3.24}$$

with $x(\omega) = (\omega_{0j}^2 - \omega^2)/\gamma_j\omega$, where ω_{0j} is the resonance frequency, γ_j is the damping, and $\sigma_{0j} = \omega_{pj}^2/\gamma_j q_j^2$ with ω_{pj} as the oscillator strength, and q_j is the asymmetry factor (dimensionless) of the j^{th} absorption. The Fano parameter reflects the asymmetry of the peak and when $|q| \to \infty$, a harmonic Lorentzian oscillator line shape is recovered. Depending on the value of q, the absorption can assume resonance ($|q|$»1, phonon dominates), dispersive ($|q|$∼1, comparable phonon and electron contribution), or antiresonance lineshapes ($|q|$«1, electrons dominate) [78]. Fig. 3.14 shows a comparison between the harmonic Lorentz oscillator and the Fano profile for different Fano parameters (q). For a large q value Lorentzian shape can be retrieved from Fano profile. Furthermore, the sign of the asymmetry factor is significant for interpretation of the results, as it points out to which electronic background the phonon is coupled.

3.4.7. Infrared test measurements on Alkali fullerides

Obtaining reasonable infrared spectra on the powder A_4C_{60} was not easy. Several test measurements had to be carried out to obtain good spectrum in FIR and MIR region. The highly air sensitive A_4C_{60} had to be handled in the glove box while filling the DAC for high pressure measurements. To obtain a good infrared spectrum, several test measurements on A_4C_{60} filled in the DAC were carried out. Both transmission and reflection measurements were tested in the FIR and MIR range.

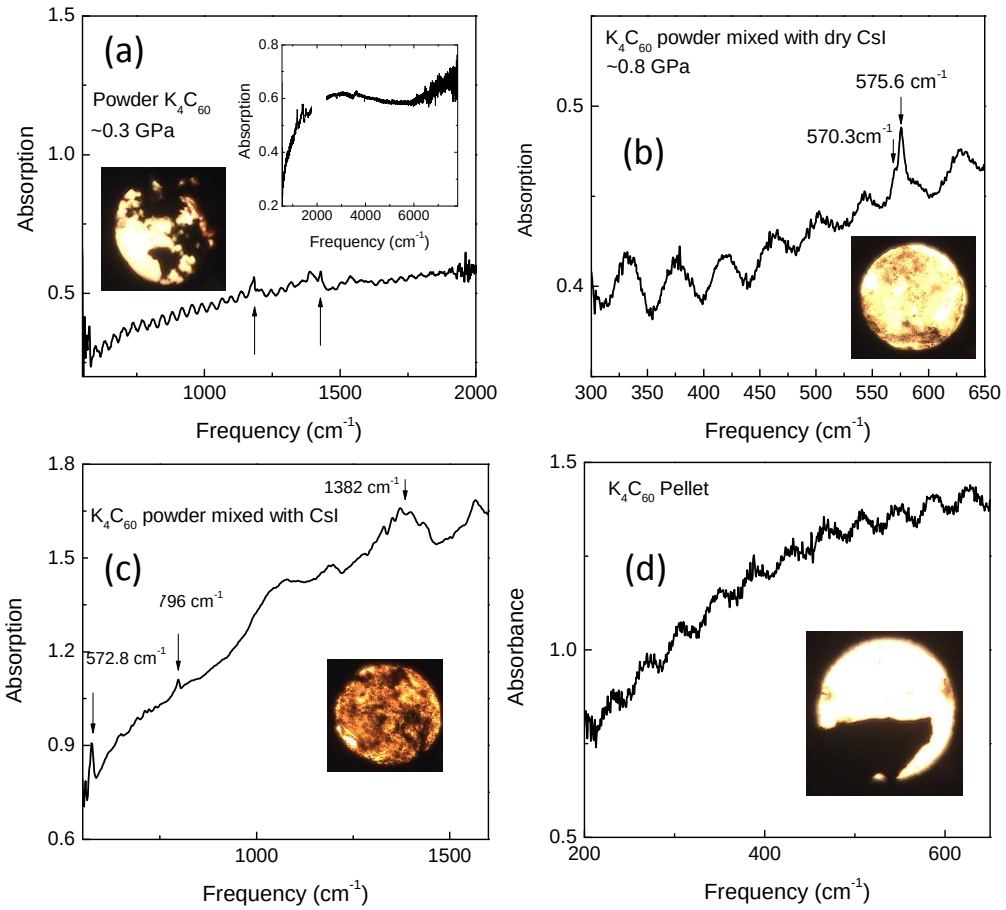

Figure 3.15.: Infrared spectra of the A_4C_{60} measured on different types of filling; (a) sample filled in DAC, (b) sample mixed with CsI, (c) sample mixed with CsI with higher sample concentration, and (d) sample pellet made with a pellet maker. Insets: microscopic view of the DAC for the respective fillings.

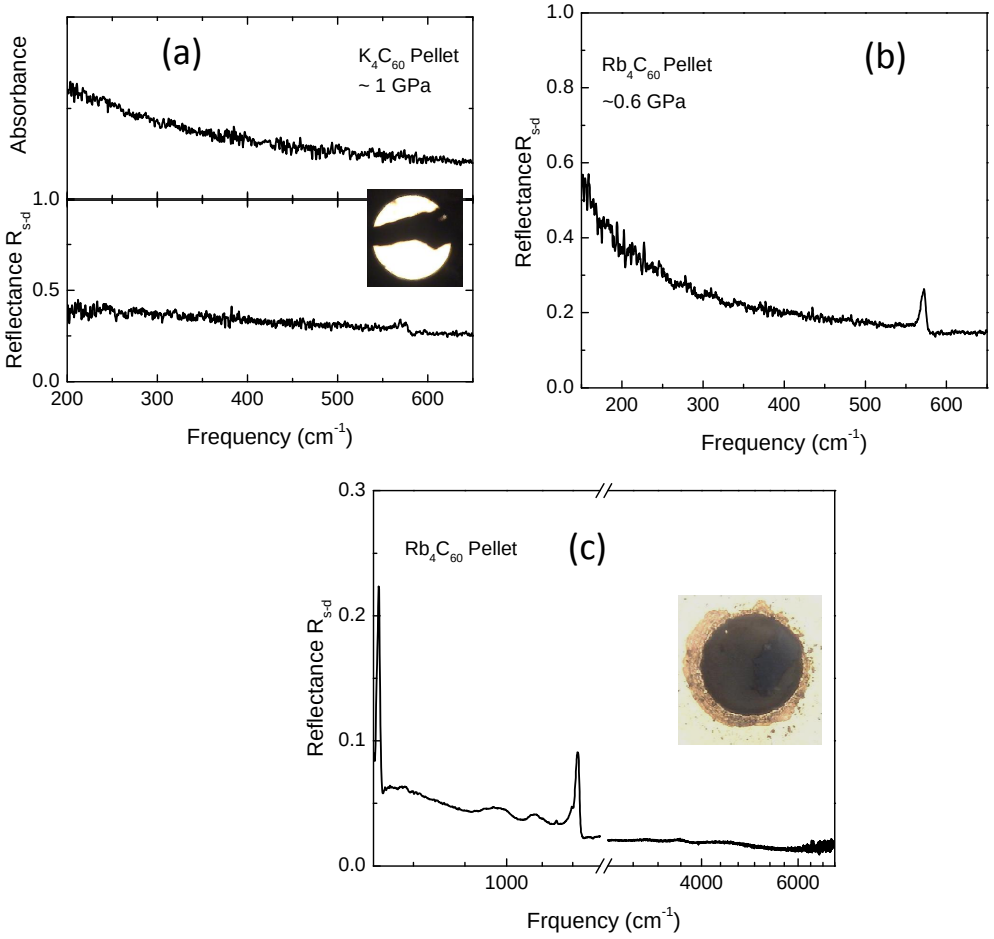

Figure 3.16.: Infrared spectra of A_4C_{60} pellets, Inset: the microscopic view of the DAC filled with A_4C_{60} pellet and pressure medium. (a) FIR absorbance and reflectance. Reflectance in (b) FIR and (c) MIR regions.

For transmission measurements, various types of fillings were tested: (i) placing powder sample over the diamond and toping it with the pressure medium (Fig. 3.15(a)), (ii) sample-CsI mixture with different concentrations (Fig. 3.15(b) and (c)), (iii) making pellet (few micrometer thick) of the sample with the pellet press (Fig. 3.15(d)), and (iv) making a pellet by pressing it in between the diamond and a pristine gasket (Fig. 3.16). The transmission measurements on the sample or sample/CsI mixture gave an infrared spectrum with the expected phonon, but it had fringes in the FIR and MIR spectra (see Fig. 3.15). Treating the fringes post measurements are extremely laborious. Thus, the measurements on the pellet were tried in transmission mode to get rid of the wiggles (Fig. 3.15 d). The pellets that were too thick for transmission

measurements, but were promising for reflection measurements (see Fig. 3.16 a).

For reliable reflection measurements in the FIR and MIR region of the spectrum different types of pellets were tested. The best method was to place a preindented gasket without the hole on the lower diamond, then a small quantity of sample was added on the center of the gasket and pressed the sample with the top diamond. This gave a good pellet that could be cut and filled in the DAC. Also, the diamond-pressed side of the pellets were more shiny and optically smoother than the gasket side. Therefore care was taken to measure on the diamond-pressed side of the pellet. A good infrared reflection spectrum in far- and mid-infrared was achieved with such a filling and is shown in Fig. 3.16 (b) and (c), respectively. The near-infrared and visible frequency regions were always measured in transmission mode.

3.5. Attenuated total reflection spectroscopy

Attenuated total reflection (ATR) measurements were carried out at Institute for Solid State Physics and Optics, Wigner Research Centre for Physics, Hungarian Academy of Sciences. A Helios ATR accessory in combination with the Bruker FTIR spectrometer (Tensor 37) was used. The spectra were recorded with 2 cm^{-1} resolution in transmission mode for MIR and NIR range. ATR spectroscopy has wide range of applications. The principle and working of ATR FTIR spectroscopy is explained briefly.

Principle of ATR

The concept of internal reflection is illustrated in Fig. 3.18 (a) and it is necessary to explain evanescent wave [79]. When the beam is passed through an optically dense crystal (n_1) at an angle on to a less dense medium (n_2), it undergoes total internal reflection at the interface, where a wave propagates along the interface and extends into the less dense medium. This wave is called as evanescent and it originates from the Latin word *evanescere* meaning 'tend to vanish'. This occurs only when the angle of incidence exceeds a critical angle (θ_c) which can be given by:

$$\sin\theta_c = \frac{n_2}{n_1} \tag{3.25}$$

The beam acts as if it penetrates a small distance beyond the reflecting surface and into the less dense medium before reflection occurs. The depth of penetration, which ranges from fraction of a wavelength up to several, depends on the index of refraction of the crystal and the angle of the incident radiation with respect to the sample-ATR crystal interface. This has the consequence that if the less dense material selectively

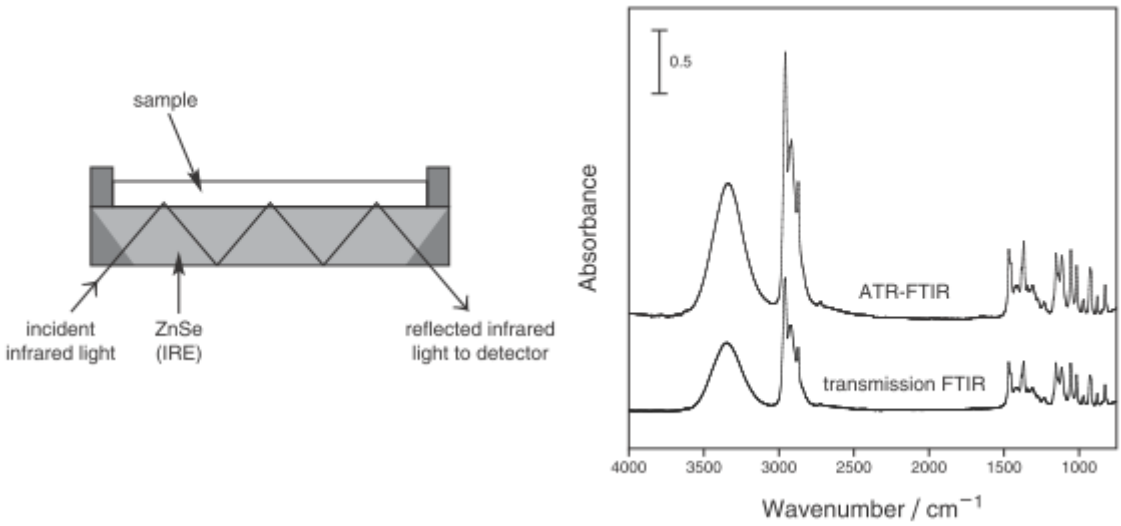

Figure 3.17.: (a) Schematic of the internal reflections through a high refractive index sample and (b) comparison of infrared spectrum of 4-methyl-2-pentanol using ATR-FTIR with conventional FTIR [80].

absorbs certain wavelength components of the evanescent radiation, then attenuation of the reflected beam occurs preferentially at the wavelength of absorbance band. This phenomenon is known as *attenuated total reflection*. By the use of FTIR spectrometer in combination with ATR, the spectral absorption characteristics of the sample can be studied. Fig. 3.18 (b) shows the comparison of the infrared spectrum measured by conventional transmission FTIR method and by ATR-FTIR.

The exponential decay of the electric field amplitude (E) within the rarer medium can be described as:

$$E = E_0 \exp \frac{-2\pi}{\lambda_1} \left(sin^2\theta - \left[\frac{n_2}{n_1} \right]^2 \right)^{1/2} z \tag{3.26}$$

where E_0 is the initial electric field amplitude, λ_1 is the wavelength of radiation in denser medium $= \lambda/n_1$, λ is the wavelength of radiation in free space, θ is incident angle, and z is the distance from the surface. By assuming low absorption by the sample medium, it can be further treated in terms of the intensity loss per reflection. The amount of energy transmitted (T) is given by $T = e^{-\alpha z}$ where α is the absorption coefficient and z thickness of the sample. The expression for reflection of a weakly absorbing sample can be written as $R = e^{-\alpha z_e} \approx$ (1-A) where z_e effective thickness.

The evanescent wave is non-transverse and therefore has components in all spatial directions. This allows its vector components to interact with the dipoles in all orien-

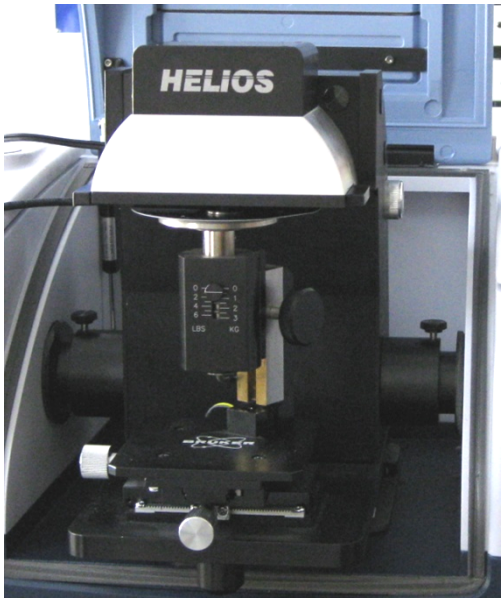

Figure 3.18: Helios ATR attached suitable to be placed in the sample chamber of Bruker FTIR spectrometer.

tations and makes it a more informative tool to probe materials. The assumption of weakly absorbing medium is true for most organic materials.

In order to obtain an ATR spectrum, the sample is placed in close contact with the crystal transparent to the infrared beam and that has high refractive index, such as type II diamond or Ge crystal. An ATR accessory mounted in the sample chamber of the spectrometer (see Fig. 3.18) was used to measure the changes that occur in a totally internally reflected beam as the beam comes in contact with the sample.

4. Synthesis of fullerene-based compounds and their characterization

4.1. Introduction

This chapter is dedicated to the synthesis and characterization of alkali fullerides and tetraphenylphosphoniumiodide samples. Specially designed instrumentations are described for the synthesis procedure of A_4C_{60}, as it is extremely air sensitive and the procedures to analyze the XRD data. The elaborate synthesis procedure of $(Ph_4P)_2IC_{60}$ single crystals is presented along with its characterization by ATR-FTIR spectroscopy.

4.2. Synthesis of alkali fullerides A_4C_{60} (A = K and Rb)

A_4C_{60} (A = K and Rb) can be synthesized by solid-state reaction [33,81–83] or by using liquid ammonia in case of Cs_4C_{60} synthesis [84]. Recently, preparation of Rb_4C_{60} single crystals were demonstrated by Hoffmann et al [85] at 937 K in a closed niobium ampule. For this project the solid-state synthesis procedure was followed. C_{60} with purity more than 99.98 % was procured from the company Term USA and purified by heating under dynamic vacuum at 200^{o}C for 2 days to remove any traces of moisture and oxygen. This purified C_{60} was carefully transferred to the glove box without exposing to air and was stored for further process. Potassium chuck in mineral oil (98 %) from Aldrich chemicals and rubidium (99.75 % metals basis) from Alfa Aesar were used. Alkali fulleride compounds are highly air sensitive. Hence all the synthesis and further handling of these compounds were carried out in the argon glove box. Stoichiometric amount of fullerene and alkali metal were added together in a glass tube. This tube was sealed under vacuum and heated for several weeks with intermediate grinding of the sample for good homogeneity. Since the alkali metals are highly reactive with air

and moisture, the following precaution are important during synthesis:

- alkali metals are highly reactive even with the trace amount of O_2 and H_2O in the glove box atmosphere. So the outer layer of the alkali metals are scraped out to expose the fresh surface just before the synthesis.
- The fullerene and alkali metals should be precisely weighed to obtain the right stoichiometry.
- While working, the pressure in the glove box changes quite frequently and hence extra care has to be taken to maintain the same pressure when weighing.
- Alkali metals like potassium and rubidium are sticky, therefore the weighed quantity has to be transferred into the reaction tube with additional attention without leaving any metal in the weighing dish.

4.2.1. Handling and manipulation of air sensitive samples

The preparation, handling and manipulation of air sensitive alkali fulleride samples require an inert atmosphere. The mBraun lab star argon glove box that is capable of maintaining a low O_2 and H_2O levels (< 0.1 ppm) was used. The glove box was equipped with optical microscope for easy filling of the DAC with air sensitive samples. The synthesis of alkali fulleride samples requires heat treatment of the sample. In order to achieve the right stoichiometry, the samples were sealed in quartz tube under vacuum with assistance of a turbo pump and then heat treated. The sealing of the quartz tubes were done with the hydrogen-oxygen welder which generates a clean high temperature (3000^oC) flame from a hand torch. A homebuilt adaptor was used to safely transfer to the sealing facility and seal the samples in the quartz tube without exposing to air.

Several technical difficulties were faced during the solid-state synthesis procedure. Many batches of A_4C_{60} samples were synthesized and approximately 300 mg for each batch of A_4C_{60} sample was the targeted quantity. The vacuum sealing of the reaction tube plays an important role in obtaining good quality A_4C_{60}. The reaction tube was sealed in vacuum with a turbo pump to achieve a vacuum of 10^{-6} mbar. Hydrogen-oxygen welding torch was used for sealing the reaction tubes (glass or quartz).

Initial batches of alkali fulleride samples always showed a loss of alkali metal and the samples were either mixture of A_3C_{60} and A_4C_{60} or purely A_3C_{60}. Glass tubes of 0.9 mm diameter and 120 mm long were used for these synthesis (shown in Fig. 4.1 (a)). With the use of such glass tubes there can be loss of alkali metal as it might

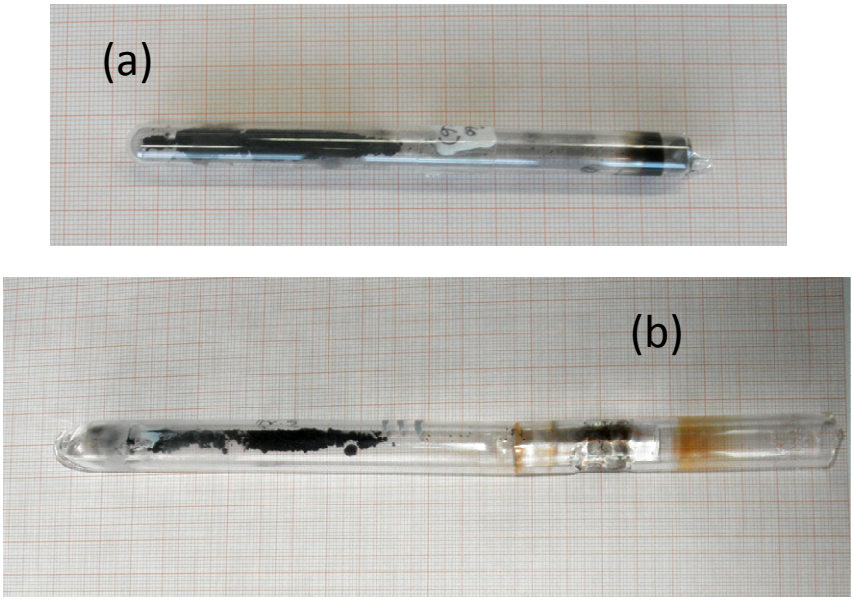

Figure 4.1.: Reaction tubes used for preparation of alkali fullerides (a) glass and (b) quartz.

diffuse into the glass, either alkali metal or C_{60} can stick to its wall and not take part in the reaction due to the length of the tube. So the glass tubes were replaced with quartz tubes (see Fig. 4.1 (b)) with a larger diameter of 14 mm and length up to 140 mm. Slightly larger diameter was chosen so that the alkali metal and C_{60} can be transferred directly at the bottom of the reaction tube. Several samples were synthesized with quartz tube. Nevertheless, the quality of the samples improved only slightly and the stoichiometry was not satisfactory. The possibilities could be that the tubes were about 120–140 mm long and the reaction was not homogenous as the fullerene and alkali metal were spread over a large reaction tube. But sealing shorter tubes can burn C_{60}. Hence there was a lack of alkali metal in the synthesized samples. Overdoped samples of stoichiometry $A_{4.5}C_{60}$ were synthesized but without much success to achieve the right stoichiometry. As an effort to improve the reaction, the reaction tubes were made compact to hold exactly about 350–400 mg of alkali fullerides. The tube was made of stainless steel as shown in the Fig. 4.2 thereby reducing the risk of any reaction of the alkali metal with the tube itself. The finely ground C_{60} and alkali metal with right stoichiometry was loaded in the stainless steel reaction tube and was then sealed inside a quartz tube under vacuum. This was heat treated at 400 – 450°C for 20 days with intermediate grinding for good homogeneity. The Rb_4C_{60} requires at least two

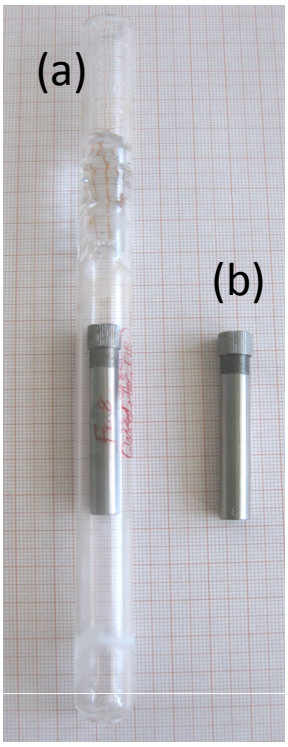

Figure 4.2: Stainless steel reaction tubes for alkali fulleride preparation: (a) stainless steel tube sealed inside a quartz tube and (b) stainless steel tube with screw cap.

intermediate grinding and K_4C_{60} requires one intermediate grinding. By this way, it was possible to achieve a good quality of alkali fulleride samples.

4.2.2. Characterization by XRD

4.2.2.1. X-ray powder diffractometer details

The powder X-ray diffraction measurements on alkali fullerides were performed in collaboration with Experimental Physics V with the STOE STADI MP powder diffractometer. The diffractometer can be operated in flat plate, Transmission-Debye-Scherrer and Variable Bragg-Brentano geometry. The data were recorded with strictly monochromatic Cu $K_{\alpha 1}$ radiation ($\lambda = 1.540598$ Å) and a position sensitive detector (PSD) was used. All measurements were carried in the range between $0 - 100°$ at room temperature. Alkali fulleride samples were characterized by powder XRD measurements to identify the phase(s) present.

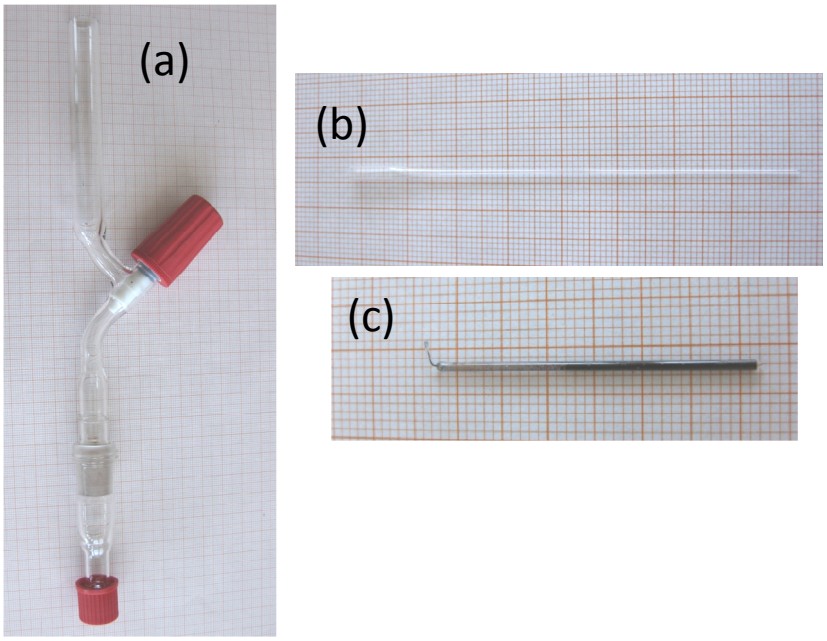

Figure 4.3.: Capillary for XRD of alkali fulleride samples (a) homebuilt adaptor to seal capillary in vacuum, (b) empty capillary and (c) sealed capillary with alkali fulleride samples.

Sample preparation for XRD measurements

To carry out the XRD on alkali fullerides, the samples must be sealed in capillaries under vacuum without exposure to the atmosphere. Kratky-Mark XRD capillaries [1] of 0.7 mm diameter (shown in Fig. 4.3 (b)) purchased from Hilgenberg company were used. A home built adapter were used to seal the sample in the capillaries under vacuum without exposure to air with a mild flame from a simple lighter (see Fig. 4.3 (a)).

XRD indexing to identify the phase

Jana 2006 program was used for analysis of the diffraction pattern. The possible parasitic phases that can occur along with the A_4C_{60} are A_3C_{60} and A_6C_{60}. By using the cell parameters from the literature [86] which is listed in the Table 4.1 for different possible parasitic phases for A_4C_{60}. The peak position were simulated by taking into account the experimental parameters such as wavelength of the X-ray, sample

[1] made from special glass no.0140

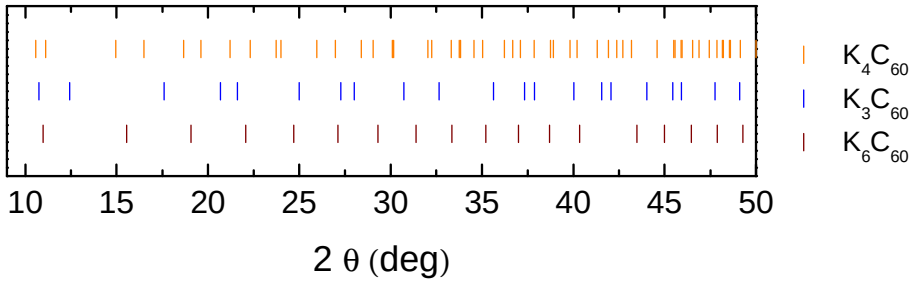

Figure 4.4.: Calculated 2θ values for K_3C_{60}, K_4C_{60}, and K_6C_{60}

A_xC_{60}	Space group	Cell parameters
K_3C_{60}	$Fm\bar{3}m$	a = 14.24 Å
K_4C_{60}	$I4/mmm$	a = 11.84 Å; c = 10.75 Å
K_6C_{60}	$Im\bar{3}$	a = 11.39
Rb_3C_{60}	$Fm\bar{3}m$	a = 14.42 Å
Rb_4C_{60}	$I4/mmm$	a = 11.96 Å; c = 10.98 Å
Rb_6C_{60}	$Im\bar{3}$	a = 11.54

Table 4.1.: Space group and cell parameters used for the simulation of the XRD peak positions for different stoichiometry of A_xC_{60} [86].

geometry, etc.

Fig. 4.4 shows the simulated *2 θ* values for the K_3C_{60}, K_4C_{60} and K_6C_{60}. Similarly Fig. 4.5 shows the *2 θ* values for Rb_3C_{60}, Rb_4C_{60}, and Rb_6C_{60}. The measured X-ray spectrum can be compared to the simulated peaks of different phases and this would enable easy identification of the phase(s) present in the sample. As an example, Rb_4C_{60} (sample no[2]: *Fr8-*Rb_4C_{60}) is shown in Fig. 4.6, this was the best Rb_4C_{60} sample that was synthesized with no detectable amount of the parasitic phase in the XRD spectrum. Among the K_4C_{60} samples that were synthesized, *Fr1-*(K_4C_{60}) was the best sample with about $\sim$ 5 % K_3C_{60} and the XRD spectrum of it is presented in Fig. 4.7. Appendix A presents the X-ray diffraction patterns of all the synthesized A_4C_{60} samples with brief explanation.

[2]Samples were named as Fr.n-A_4C_{60}, where n denoting the batch number and A being either K/Rb

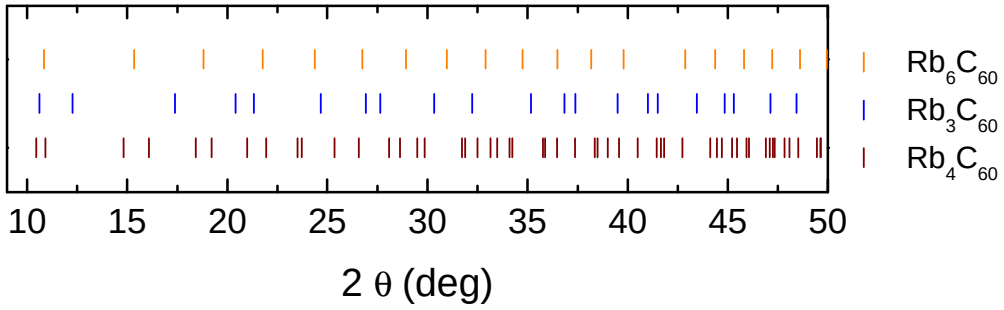

Figure 4.5.: Calculated 2θ values for Rb_3C_{60}, Rb_4C_{60}, and Rb_6C_{60}

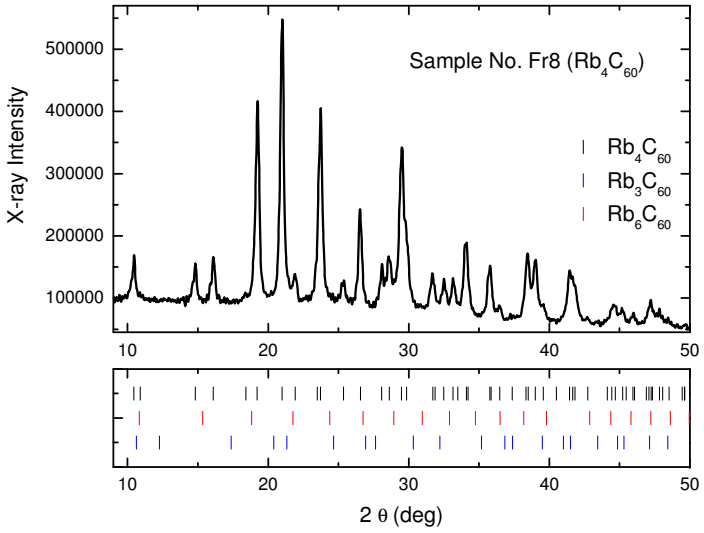

Figure 4.6.: X-ray spectrum of phase pure Rb_4C_{60} of *Fr8* sample.

4.3. Synthesis of $(Ph_4P)_2IC_{60}$

Tetraphenylphosphonium halide-C_{60} were the first fullerene salts to be synthesized in 1991 in powder form [87]. The originally proposed salts for the synthesis were $(Ph_4P)_3C_{60}(X)_2$ instead of $(Ph_4P)_2C_{60}(X)$ where X stands for halogen. Single crystals were reported by electrocrystallization technique after two years [88].

Synthesis of $(Ph_4P)_2IC_{60}$ single crystal samples and characterization by ATR-FTIR spectroscopy were done in collaboration with Dr. K. Kamarás's group at Institute for Solid State Physics and Optics, Wigner Research Center for Physics, Hungarian Academy of Sciences, Budapest, Hungary especially with the help of Ms. Katalin Németh. Single crystal samples are the best for infrared measurements, therefore $(Ph_4P)_2IC_{60}$

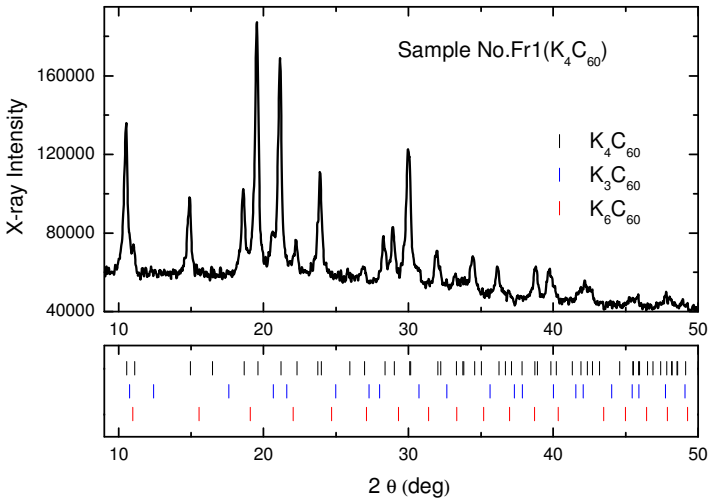

Figure 4.7.: X-ray spectrum of K_4C_{60} of *Fr1* sample.

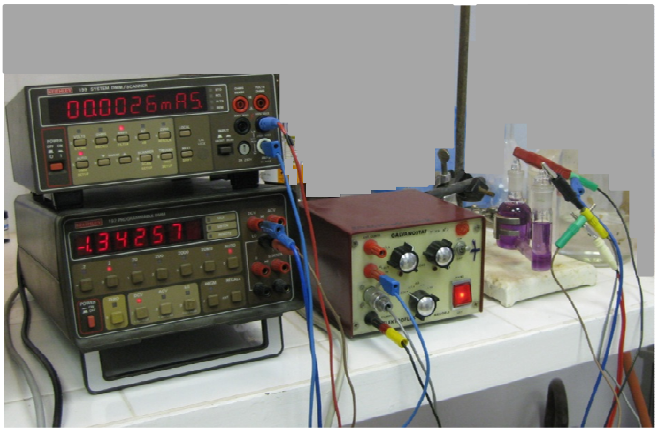

Figure 4.8.: Setup used for synthesis of $(Ph_4P)_2IC_{60}$ samples.

were made by the electrochemical synthesis method. The electrolysis were performed over platinum cathode at a constant current of 30 μA. The setup used for the synthesis is shown in the Fig. 4.8. Electrolysis was carried out in the solution of Ph_4PI and C_{60} which was dissolved in 1:1 mixture of dichloromethane and toluene at ambient conditions. The solution was purged with nitrogen gas. The schematic diagram of the reaction tube is illustrated in Fig. 4.9 (a) and the crystals grown over the Pt electrode are shown in Fig. 4.9 (b). Black shiny crystals of 100–300 μm size were seen on the electrodes after about 5 days and were removed from the Pt electrode very gently (see

Fig. 4.9 (c)).

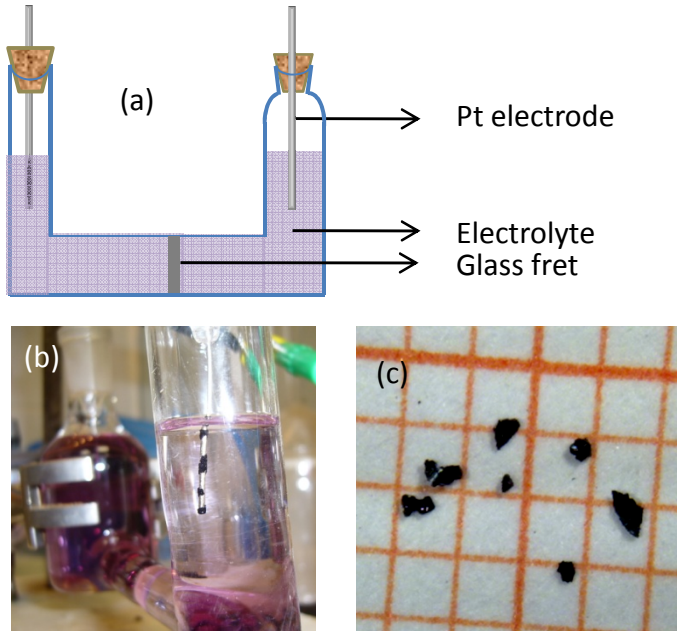

Figure 4.9.: (a) Schematic diagram of the reaction tube used for electro-chemical synthesis of $(Ph_4P)_2IC_{60}$ samples, (b) photo of the Pt-electrode with as-grown samples inside the electrolyte, and (c) photo of $(Ph_4P)_2IC_{60}$ single crystal on a millimeter paper.

4.3.1. Characterization by ATR spectroscopy

The ATR attachment described in section 3.5 was used to measure the $(Ph_4P)_2IC_{60}$ single crystals in MIR and NIR range to verify the quality of the sample and the spectra are presented in Fig. 4.10. The MIR region of the spectrum presented in Fig. 4.10 (a) shows the vibrational modes of the C_{60}^- ion and $(Ph_4P)_2I^+$ that is in good agreement with the literature spectrum of $(Ph_4P)_2IC_{60}$ [2]. The main advantage of the ATR measurements was the ability to get the absorbance spectrum directly from the as-grown single crystal without any sample preparations. The ATR NIR spectrum in Fig. 4.10 (b) shows the electronic transition and is also in agreement with the spectrum of C_{60}^- [89]. Thus confirming the quality of $(Ph_4P)_2IC_{60}$ single crystals.

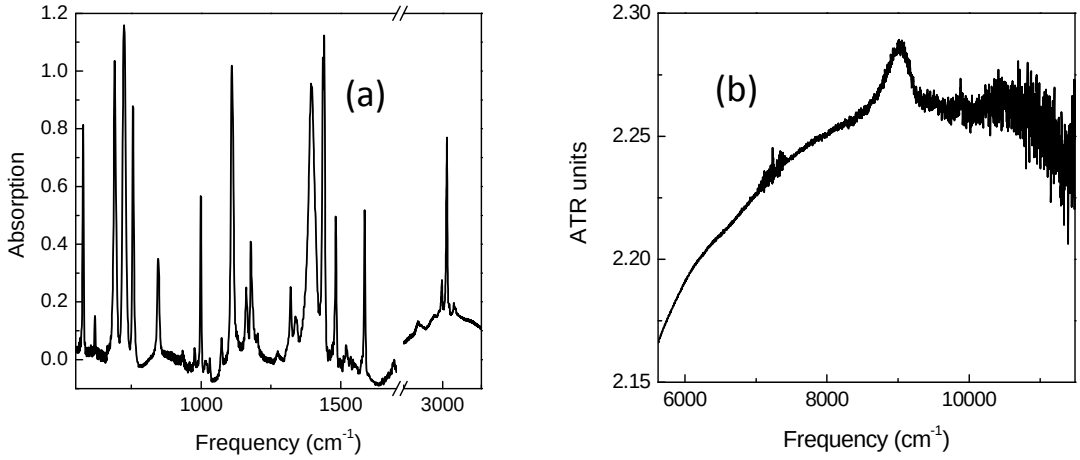

Figure 4.10.: ATR spectra of $(Ph_4P)_2IC_{60}$ in (a) MIR and (b) NIR region.

5. Jahn-Teller effect in fullerene ion C_{60}^{-}

5.1. Introduction

In this chapter, the pressure-dependent investigation of C_{60}^{-} in $(Ph_4P)_2IC_{60}$ is presented. The crystal structure of $(Ph_4P)_2IC_{60}$ and its properties are briefly discussed. An introduction to Jahn-Teller effect on fullerene anion is given. The results of high-pressure infrared studies on $(Ph_4P)_2IC_{60}$ are discussed in terms of the Jahn-Teller effects in C_{60}^{-}. Finally, an elaborate discussion regarding the symmetry changes under pressure is presented.

The goal of this work is to understand the Jahn-Teller dynamics of C_{60}^{-} under high pressure. C_{60}^{-} can serve as a model system to probe the JTE in highly symmetrical molecules. C_{60} distorts from highly symmetrical I_h to D_{3d}/D_{5d} or lower symmetry on addition of an electron. $(Ph_4P)_2IC_{60}$ (Tetraphenylphosphonium iodide-C_{60}) is a prototype to study C_{60}^{-} radical anion in a solid state environment due to its large cation. The Phenyl cation is so well positioned that it separates the C_{60}^{-} from each other. The time scale of infrared measurements (10^{-11} s^{-1}) is of the order of the Jahn-Teller pseudorotation frequency (between 10^{-9} and 10^{-13} s^{-1} [31]) of the C_{60}^{-} ion. In other words, the pseudorotation of the C_{60}^{-} molecule could be observed from the infrared vibrational modes as splitting and also its symmetry could be deduced. Thus infrared spectroscopy is a very powerful tool to investigate the JT dynamics.

The far-infrared temperature dependence on $(Ph_4P)_2IC_{60}$ was studied by Long *et al* [1, 2]. Similar effects are exhibited by C_{60} and several fullerene-based compounds with lowering the temperature and increasing the pressure [90–92]. In case of $(Ph_4P)_2IC_{60}$ temperature induced dynamic-to-static Jahn-Teller transition is caused by decrease of both the lattice constants and the thermal energy. The increase in pressure can compress the lattice but does not change the thermal energy of the system, therefore the JT effect does not necessarily need to be similar for lowering temperature and

increasing pressure. By investigating the vibrational properties, the electronic, and vibronic interaction as a function of external pressure the changes in the symmetry of the molecule can be addressed. Also a comparison between the effect of pressure and temperature lowering [1, 2] on the vibrational properties of $(Ph_4P)_2IC_{60}$ can be done.

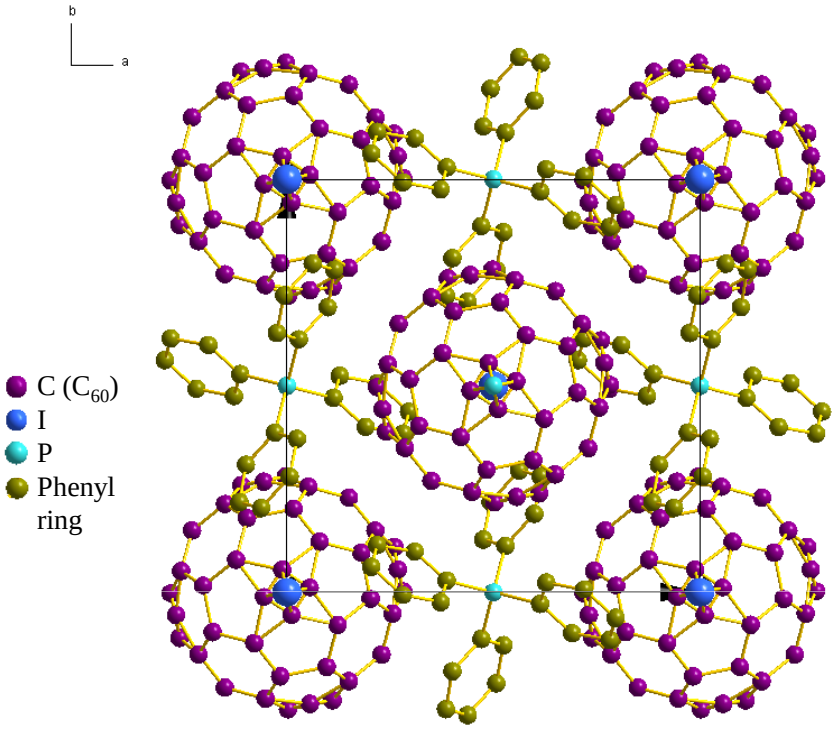

Figure 5.1.: Crystal structure of $(Ph_4P)_2IC_{60}$. The lattice parameters were adopted from Ref. [88, 93, 94].

5.2. Crystal structure

$(Ph_4P)_2IC_{60}$ can be grown as single crystals in contrast to the powder form of several other fullerene anions. The details about the synthesis of $(Ph_4P)_2IC_{60}$ for this project is described in section 4.3. The structure was independently determined by Pénicaud *et al.* [88] and by Bilow and Jansen [94]. At ambient conditions $(Ph_4P)_2IC_{60}$ crystallizes in a tetragonal structure with unit cell parameters a = b $\sim$ 12.5 Å and c = $\sim$ 20.3 Å, and I4/m space group [88,93,94]. The structure of $(Ph_4P)_2IC_{60}$ is similar to a distorted CsCl-type structure in which Cs^+ is replaced by $(Ph_4P)_2{}^+$ and Cl^- alternatively with halogen or C_{60}^- [95]. Fig. 7.1 shows the crystal structure of $(Ph_4P)_2IC_{60}$. The host

lattice is formed by $(Ph_4P)^+$ cations which are stabilized by multiple phenyl rings. $(Ph_4P)_2XC_{60}$ with X = Cl or Br has a homopolar lattice along (011) plane [95]. It can be noted that this compound has two counterions for one C_{60}^-, the charge neutrality is preserved by one halide ion per C_{60}^-. $(Ph_4P)_2IC_{60}$ compound has the advantage of being air stable unlike many other fullerene anions.

5.3. Jahn-Teller effect in $(Ph_4P)_2IC_{60}$

The best way to investigate the Jahn-Teller distortion on C_{60}^- is to study the isolated C_{60}^- ions. The C_{60}^- in gas phase was studied by MIR [96] and NIR [89] spectroscopy which show dynamic Jahn-Teller distortion of the molecules. When measuring C_{60}^- in solution or frozen matrix such as in 2-methyltetrahydrofuran (2-MeTHF) [97], the effect of the environment must also be taken into account. Another possibility is to study the C_{60}^- in solid-state compounds that contain bulky cations, so that it has nearly isolated C_{60}^-. But the presence of the large cations cause the symmetry lowering of the lattice. Therefore the choice of the compound must be made carefully.

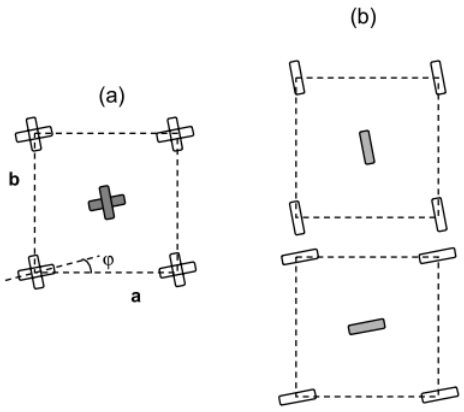

Figure 5.2.: Schematic representation of the C_{60} orientation in $(Ph_4P)_2BrC_{60}$ at (a) room temperature and (b) low temperature [95].

At room temperature, the dynamic nature of the Jahn-Teller effect in $(Ph_4Y)_2XC_{60}$ (X = Cl, I, or Br and Y = P or As) was shown by electron spin resonance (ESR) [98], nuclear magnetic resonance (NMR), and infrared (IR) spectroscopy [1–3]. Also theory predicts that the dynamic nature of the JT effect for singly charged fullerene C_{60}^- would be reflected in the IR spectrum [99]. At room temperature, the dynamic Jahn-Teller effect of the C_{60}^- is signalled in the infrared spectrum by the splitting of the T_{1u} fundamental modes and the activation of silent modes. The temperature dependence

of the JT dynamics was studied on $(Ph_4P)_2IC_{60}$ by far-infrared spectroscopy [1–3]. As a direct consequence of the dynamical symmetry breaking, silent mode activation in the infrared absorption spectrum was evaluated with the prediction that some of the relaxed JT-active Raman modes should be observable in the IR absorption. The IR parity selection rule breaks down and some Raman active modes appear in the IR spectrum as phonon overtones.

The other experimental evidence of dynamic nature of the JT effects were given by ESR measurements [4, 98, 100, 101]. The ESR [4] on $[A^{+}(C_6H_5)_4]_2C_{60}{}^{-}B^{-}$ (where A = P or As and B = I or Cl) indicate static disorder with random occupation of two "standard orientations" at low temperature. This is consistent with the structural transition from I4/m to I2/m in $(Ph_4P^{+})_2C_{60}{}^{-}Br^{-}$ around 120 K [95]. From the x-ray diffuse scattering and diffraction above 130 K $(Ph_4P)_2BrC_{60}$ has I4/m structure, which can be explained to be formed from the superposition of two orientations of C_{60}^{-} ion as shown in Fig. 5.2 (a). In other words, the icosahedral C_{60} does not have fourfold axis so to conserve the tetragonal environment the structure can have two orientations of the C_{60}^{-} molecule. This can be understood in terms of the dynamic Jahn-Teller effect with the C_{60}^{-} in different orientations. And on cooling below 120 K, the scenario to explain I2/m symmetry is to have ordered domains which can be conceived as the cooperative Jahn-Teller effect as shown in Fig. 5.2 (b).

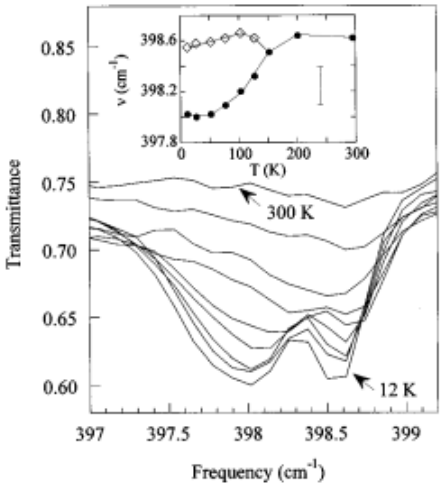

Figure 5.3.: Temperature dependence of $G_u(1)$-derived mode of $(Ph_4P)_2IC_{60}$ and the inset is a plot of frequency versus temperature [1].

As a function of temperature, a weak transition in the range of 125–150 K from infrared measurements was attributed to the dynamic-to-static Jahn-Teller transition

in $(Ph_4P)_2IC_{60}$ [1]. Long *et al* have discussed in detail all the observed vibrational modes in the far-infrared region as a function temperature. Among all the observed modes the major FIR features are at 90, 110, 135, 398, 504, 525, 527, and 576 cm^{-1}. Both the T_{1u} modes at 525 and 576 are doublets at room temperature and their splitting has been attributed to D_{5d} or D_{3d} distortions of the C_{60}^-. The counterion mode at 527 cm^{-1} strongly overlaps the $T_{1u}(1)$ of C_{60}^- vibrations and it is hard to follow the temperature-dependent behavior of the counterion mode. The mode at 504 cm^{-1} and the combination modes at 90, 110, 135 cm^{-1} are not clearly assigned. In general most of the modes harden with an exception of low frequency side of 398 cm^{-1}. The hardening of the combination modes and intermolecular modes could be due to the lattice stiffening at low temperature, where as the softening behavior is not very well understood but suggested to be due to the radial character of the mode. As an example, from Long *et al.* article, $G_u(1)$ mode (at 398 cm^{-1}) is discussed more in detail here. $G_u(1)$ mode is a newly activated in C_{60}^-, and is a singlet at room temperature. It persists as a singlet down to 150 K and on further cooling it splits in to a doublet at 150 K as seen in Fig 5.3. The high frequency side of the doublet is almost independent of the temperature, where as the low frequency side softens strongly just below the transition temperature and levels out. It has been suggested that the softening could occur due to the radial nature of the mode. The normal mode calculations of C_{60} have shown that $G_u(1)$ mode has 83 % radial character. Similarly in $(Ph_4As)_2ClC_{60}$, the C_{60}^- molecule shows weak changes around 125 K in the XRD experiments, that is attributed to orientational glass transition [93]. It has to be noted that in case of C_{60}^-, the magnitude of displacement is about 0.01 Å for only 20 out of the 60 carbon atoms [102]. Thus direct observation of the structural distortion is difficult [103], whereas this tiny distortion in a highly symmetric molecule can produce profound effects in the infrared vibrational properties.

5.4. High pressure infrared investigation of $(Ph_4P)_2IC_{60}$

High pressure infrared measurements on $(Ph_4P)_2IC_{60}$ up to 9 GPa were carried out with Syassen-Holzapfel DAC. CsI was used as the quasi hydrostatic pressure transmitting medium. The transmission measurements were carried out over a broad frequency range from FIR to visible (200–20000 cm^{-1}) at room temperature. The measurements on single crystal samples were performed with 1 cm^{-1} resolution in the frequency range 100–600 cm^{-1} and 2 cm^{-1} resolution for 550–8000 cm^{-1}. A typical view of DAC under

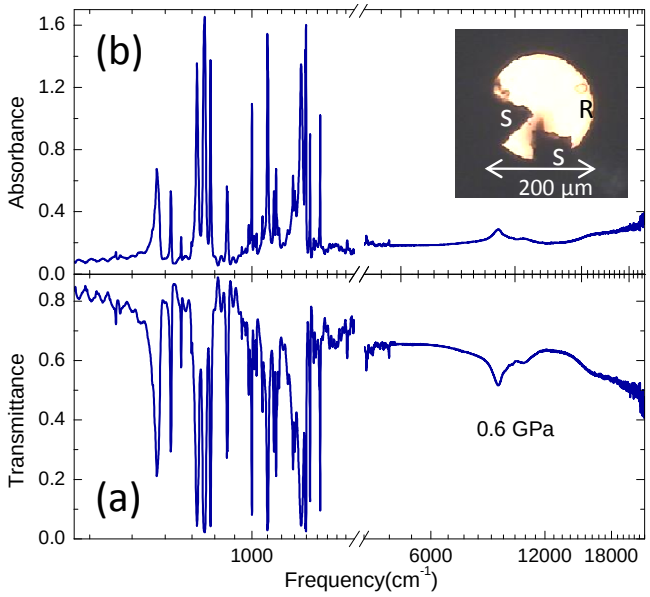

Figure 5.4.: Infrared (a) transmission and (b) absorption spectrum of $(Ph_4P)_2IC_{60}$. Inset: The DAC filled with sample (S), ruby ball (R) and pressure transmitting medium (bright region) for MIR measurement.

the microscope filled for FIR or MIR measurement containing the sample, the ruby ball and pressure transmitting medium is shown in the inset of Fig. 5.4. In order to obtain a good spectrum in the NIR-VIS region, finely ground sample was mixed with CsI and was filled in the DAC. After the pressure measurement the DAC was refilled with CsI to measure the reference at the end. The data were collected with 4 cm^{-1} resolution in the NIR-VIS region.

5.5. Results and discussion

Transmission and absorbance spectrum of $(Ph_4P)_2IC_{60}$ are presented in Fig. 5.4 from 300 to 20000 cm^{-1}. The far- and mid-infrared regions contain the vibrational modes of the C_{60}^{-} and $(Ph_4P^{+})_2I$. The near-infrared and visible region of the spectrum contains the electronic and vibronic transitions in the region between 6000–12000 cm^{-1}. Finally the LUMO $\rightarrow$ LUMO+1 transition is observed beyond 12000 cm^{-1}.

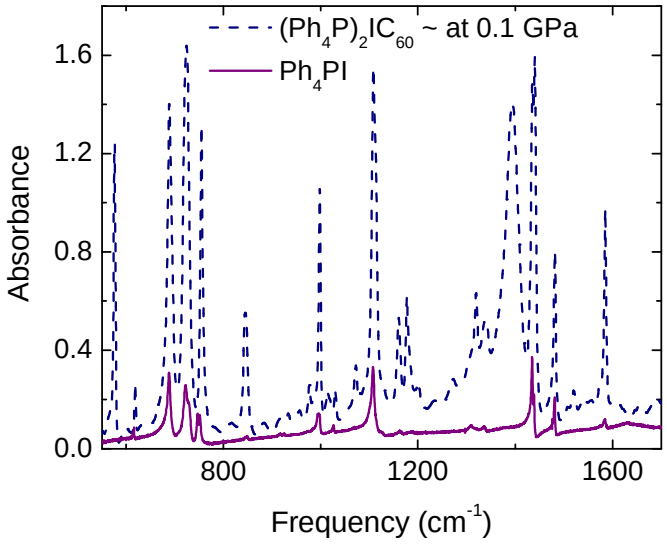

Figure 5.5.: Infrared absorption spectrum of $(Ph_4P)_2IC_{60}$ at $\sim$ 0.1 GPa in comparison with that of the cation Ph_4PI [104] spectrum.

5.5.1. Infrared spectrum of $(Ph_4P)_2IC_{60}$ at lowest pressure

Vibrational modes

The mid- and far-infrared spectra is populated with vibrational modes originating both from the C_{60}^- and the cation. The phenyl cation has significant number of infrared active vibrational modes. In order to illustrate this, the infrared spectrum of $(Ph_4P)_2IC_{60}$ (at $\sim$ 0.1 GPa) is presented in comparison with that of the Ph_4PI (at ambient conditions) in Fig. 5.5.

As already discussed in Chapter. 2.11, the neutral fullerene contains four fundamental (T_{1u}) infrared active vibrational modes. The T_{1u} modes of C_{60} are observed as sharp singlet at 517, 576, 1183, and 1428 cm^{-1} at ambient conditions. In $(Ph_4P)_2IC_{60}$ the T_{1u} modes of C_{60}^- are observed at (1) 517, 533, (2) 576, 578, (3) 1177, 1182, and (4) 1364, 1395 cm^{-1} for the lowest measured pressure. On comparing the fundamental modes of neutral C_{60} and C_{60}^-, the striking difference is that the T_{1u} modes of C_{60}^- are observed as doublets (see Fig.5.10). Among the four fundamental vibrational modes, $T_{1u}(4)$ shows the maximum downshift in frequency position compared to neutral C_{60}. $T_{1u}(4)$ has the greatest double bond stretching aspect of all the IR mode in I_h C_{60} [105]. Therefore this mode serves as a sensitive marker for identifying the the charge state [55]. Table 5.1 lists the inter-fullerene distance of some fullerene-based compounds to emphasize this. The nearest C_{60}-C_{60} distance in $(Ph_4A)^+X^-$ series is considerably larger than

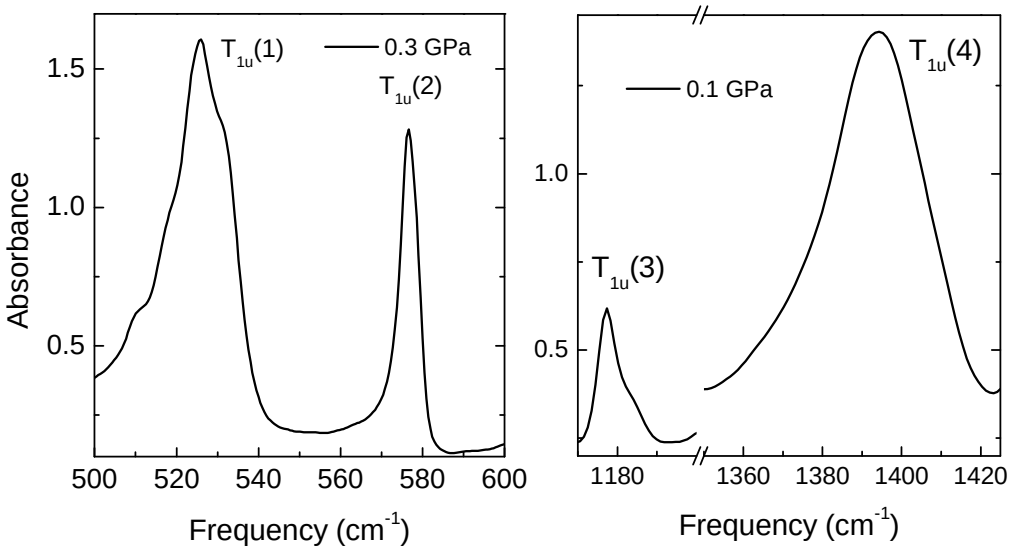

Figure 5.6.: Fundamental T_{1u} vibrational modes of $(Ph_4P)_2IC_{60}$.

C_{60}. In addition to the fundamental modes of C_{60}^{-}, there are other fullerene modes observed in the spectrum as activated silent modes.

Compound	interfullerene distance
$(Ph_4As)_2ClC_{60}$	12.59 Å
$(Ph_4P)_2ClC_{60}$	12.57 Å
K_3C_{60}	10.07 Å
C_{60}	10.02 Å
TDAE-C_{60}	9.98 Å

Table 5.1.: Inter fullerene distance of the fullerene-based compounds at ambient conditions [4].

As a matter of fact, the vibrational properties are highly sensitive to molecular symmetry. The dynamic Jahn-Teller distortion in $(Ph_4P)_2IC_{60}$ as a function of temperature was investigated with far-infrared spectroscopy by Long *et al* [1, 2]. The doublet splitting of the T_{1u} mode according to group theory would predict the symmetry to be D_{3d} or D_{5d} [106]. Among the subgroups of I_h symmetry, the possibility of D_{2h} was ruled out as this would give rise to triplet splitting. As the vibrational modes are highly sensitive to symmetry changes, the influence of the pressure or temperature can be well studied from the vibrational spectrum of the molecule. A direct comparison of the far-infrared temperature dependence on $(Ph_4P)_2IC_{60}$ by Long *et al.* [1, 2]

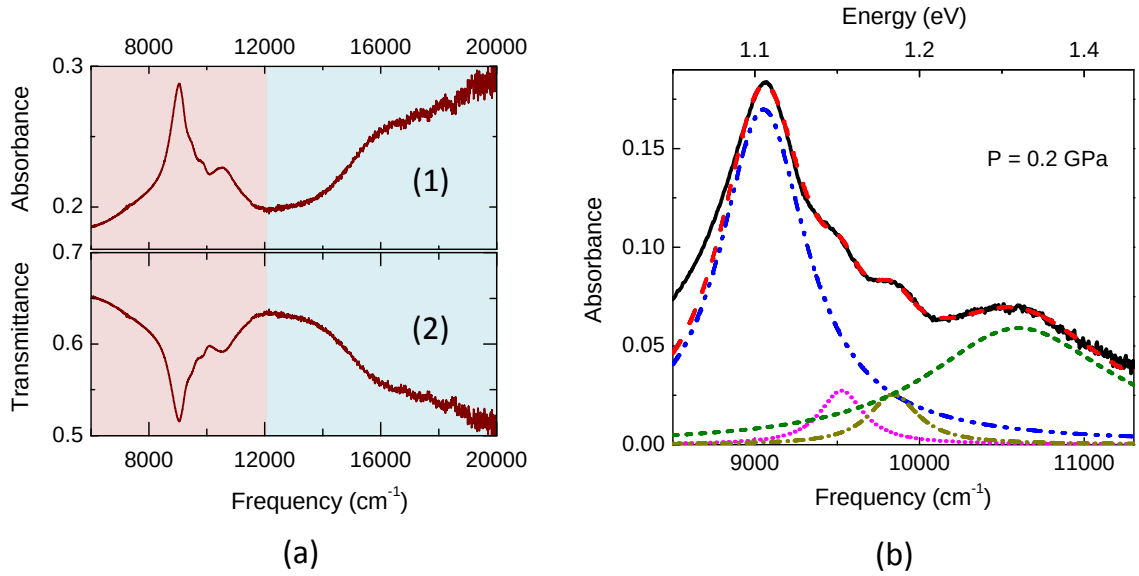

Figure 5.7.: (a) Transmission (1) and absorbance (2) spectra in the NIR-visible region. (b) Absorbance spectrum of $(Ph_4P)_2IC_{60}$ at 0.2 GPa with the fit (red dashed line) and its Lorentz oscillator contributions.

with this data is as follows:

- At the near ambient conditions, the doublet splitting of the $T_{1u}(1)$ and $T_{1u}(2)$ is consistent with their report.
- The $G_u(1)$ vibrational mode at 398 cm^{-1} is reported as a singlet at room temperature.
- The vibrational mode observed by Long *et al* [2] at 504 cm^{-1} has shifted to 509 cm^{-1} in the presented data. The origin of this mode is not very clear and has been discussed as a $T_{1u}(1)$ derived mode by Long *et al.* [3], and
- Lastly the vibrational mode at 619 cm^{-1} arising from cation is observed as a singlet.

The assignment of the vibrational modes in the MIR region are more difficult because of the abundance of the cation contribution in this region. In a recent paper, Long *et al.* [3] have investigated $(Ph_4As)_2ClC_{60}$ and discussed the possibility of lower symmetry both experimentally and theoretically. They discussed the possibility of C_{60}^{-} having $C_{2h,5}$ or C_i symmetry. $C_{2h,5}$ follows the D_{5d} symmetry undergoing a further distortion

to C_{2h} [31]. In case of $C_{2h,5}$, the largest bond length change of the distorted cage is the shortening of a few single bond by 0.012–0.013 Å. All other changes are less than 0.01 Å. This makes it hard to be detected by structural studies. Here the D_{3d} and D_{5d} symmetry are considered in the presented high pressure data of $(Ph_4P)_2IC_{60}$, while the possibility of lower symmetry are not completely ruled out.

Electronic/Vibronic transitions

Studying the electronic transitions of the C_{60}^- anion can throw light on understanding of the intermolecular interactions, charge transfer process, and electronic states. The electronic transitions have an advantage over the vibrational properties as they are less perturbed by the cation compared to the vibrational structure. The influence of the halogen ion (donor) radii indirectly affects the vibrational spectrum whereas the electronic absorption spectrum is relatively independent of the donor [106].

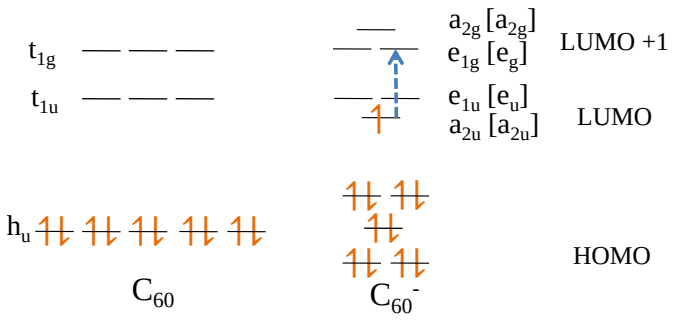

Figure 5.8.: Molecular orbital of C_{60} and C_{60}^- where the blue arrow indicates the optically allowed transition in C_{60}^- for D_{5d} or D_{3d} distortion [107, 108].

For C_{60}^- the electronic states are coupled to the vibrational modes which gives rise to the vibronic transitions. The electronic and vibronic transitions are clearly observed between 6000–12000 cm^{-1} as shown in the NIR region in Fig. 5.7 (marked with a pink background). Fig 5.7 (b) shows the fitting of the electronic transition in the NIR region of the measured spectrum along with its contributions. Lorentz oscillators were used as the fitting function. To obtain perfect fit on the low frequency side, an additional oscillator is required for describing the background which does not affect the frequency positions of the other main oscillators. There are four distinct transitions in the NIR region of the spectrum. In order to explain the observed features of the NIR region, the schematic presented in Fig. 5.8 can be used.

Several NIR investigations report similar spectra on C_{60}^- in solution [97] and isolated C_{60}^- [89]. Electronic transitions of isolated C_{60}^- in neon matrices showed well

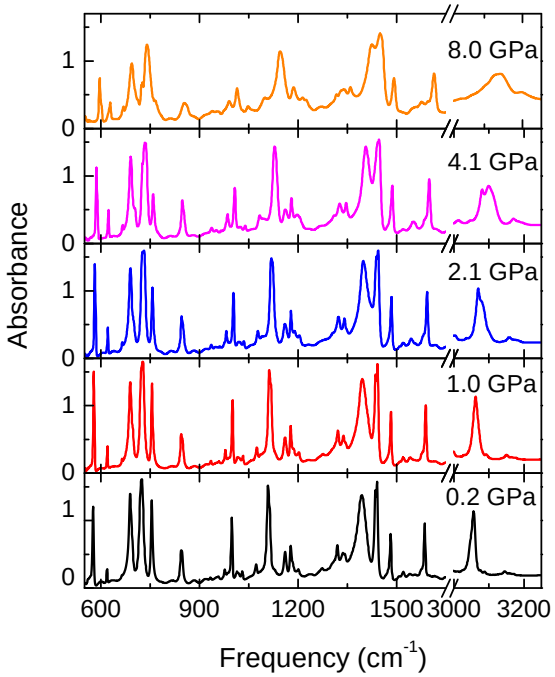

Figure 5.9: Development of the infrared absorption spectrum of $(Ph_4P)_2IC_{60}$ with increasing pressure.

resolved spectrum [109]. C_{60}^- anion in benzonitrile solution shows electronic transition at 9276.4 cm^{-1} and vibronic transitions at higher energies [107]. The environment in which the C_{60}^- anion is investigated is an important criterium to determine the nature of the distortion which can either be static or dynamic.

From the vibrational spectrum it is clear that at the lowest measured pressure C_{60}^- in $(Ph_4P)_2IC_{60}$ possess dynamic Jahn-Teller distortion. The basic question that immediately follows is about the symmetry of the molecule. The answer to this question can be obtained from understanding the electronic states. In C_{60}^- the t_{1u} and t_{1g} (LUMO and LUMO+1) are split into a_{2u}+e_{1u} and a_{2g}+e_{1g} respectively [38, 108], where e_{1g} and e_{1u} are doubly degenerate as shown in Fig. 5.8. The Jahn-Teller distortion of the ground and excited states of C_{60}^- leads to the symmetry lowering. The calculated symmetry for C_{60}^- gives rise to the three possible point groups D_{5d}, D_{3d} or D_{2h} which possess nearly same Jahn-Teller energies [110]. On adiabatic potential energy surface there are 6 equivalent structures possible for D_{5d} minima, 10 for D_{3d} minima, and 15 for D_{2h} minima [110]. Due to the equivalent energy the dynamic conservation among these distortions can take place. In case of D_{5d} symmetry, the orbitals ($^2t_{1u}$ and $^2t_{1g}$) undergo a doublet split into ($^2a_{2u}$, $^2e_{1u}$) and ($^2e_{1g}$, $^2a_{2g}$), respectively and similarly for D_{3d}, it would be ($^2a_{2u}$, ^2e_u) and (^2e_g, $^2a_{2g}$), respectively. Both D_{5d} and D_{3d} symmetry allow only one optical transition of the form $a_{2u} \rightarrow e_g$ as shown schematically in Fig. 5.8. In case of D_{2h} symmetry, $^2t_{1u}$ and $^2t_{1g}$ undergo a triplet splitting into ($^2b_{1u}$, $^2b_{2u}$,

$^2b_{3u}$) and ($^2b_{1g}$, $^2b_{2g}$, $^2b_{3g}$), respectively. Thus, D_{2h} distortion would give rise to two optically allowed transitions of the type $b_{1u} \rightarrow b_{3g}$ and $b_{1u} \rightarrow b_{2g}$ [97]. It has been suggested that D_{2h} symmetry can be stabilized only in a crystal field and not in case of a free C_{60}^- [32]. In contrast to this claim, Long *et al.* have ruled out the possibilities of D_{2h} symmetry due the the narrow lines in the FIR spectra of $(Ph_4P)_2IC_{60}$ [1, 2].

Lawson *et al.* explain the features observed in the NIR region of C_{60}^- anion in benzonitrile solution with D_{5d} symmetry [107]. The strong feature at 9276 cm^{-1} in the spectrum is attributed to the optically allowed $a_{2u} \rightarrow e_{1g}$ transition which is also in agreement with the density functional calculations of Green *et al.* [108]. The not very well resolved manifold around 10000 – 12500 cm^{-1} observed by Lawson *et al.* [107], is assigned to the vibronic transitions to the level a_{2g}. In a recent NIR investigation on C_{60}^- carried out by Hands *et al.*, a well-resolved spectrum in the region 9000 – 13000 cm^{-1} is presented [111]. They discuss the possibility of D_{3d} and D_{5d} symmetry and claim that the four contributions in the NIR region are due to the D_{3d} symmetry, and that the spectrum would have fewer contributions in case of D_{5d} symmetry. The dynamics for a minimum of D_{5d} symmetry is simpler than that of D_{3d} due to the tunneling splitting between symmetry-adapted states that correctly describe tunneling between equivalent minima [38]. In addition C_{60}^- ion prepared in other media such as in a gas matrix [109], by electrogeneration [112], and in salts [113] was also studied at ambient conditions. Also theoretical calculations [38, 110] have been carried out to explain the complicated electronic transition observed in C_{60}^-. There are also other arguments to explain the complicated NIR spectrum of C_{60}^-.

With a above review of the literatures available on the NIR spectra of C_{60}^- ion in different matrix and also theoretical explanation, the observed NIR spectrum is interpreted as the combination of electronic and vibronic transitions. The strong feature at 9049.8 cm^{-1} is due to the optically allowed $a_{2u} \rightarrow e_{1g}$ transition possible either in D_{5d} or D_{3d} symmetry. The higher lying manifold between 9300 and 11000 cm^{-1} is assigned to the vibronic transitions.

From the FIR-MIR data it is clear that the symmetry is governed by dynamic Jahn-Teller effect near ambient conditions. Following the same line of argument it is suggested that at lowest pressure the spectrum manifest the dynamic Jahn-Teller distortion of C_{60}^- also in the NIR region. Thus both the electronic and vibrational spectrum of $(Ph_4P)_2IC_{60}$ support the possibility of D_{3d} or D_{5d} symmetry under dynamic Jahn-Teller effect. The different orientations for D_{5d} and D_{3d} distortions are separated by shallow energy minima which are connected by pseudorotation causing the disorder in the dynamic system. Further in the visible region [107] the higher energy transition is observed above 12000 cm^{-1}.

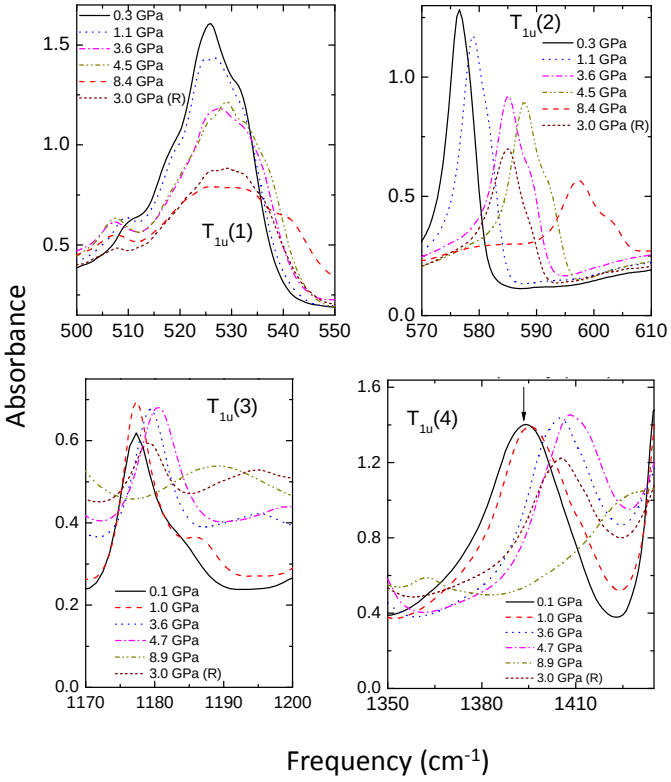

Figure 5.10.: Infrared absorbance spectra of T_{1u} modes of $(Ph_4P)_2IC_{60}$ for selected pressures.

5.5.2. Pressure dependence of $(Ph_4P)_2IC_{60}$

Pressure dependence of the vibrational modes

As already mentioned a direct comparison of the effects of lowering temperature and increasing pressure on $(Ph_4P)_2IC_{60}$ is possible. The results of $(Ph_4P)_2IC_{60}$ temperature dependence from Long *et al.* paper is presented briefly in Section. 5.3. On lowering the temperature, they observe weak anomaly in the range 125–150 K in several fullerene and cation modes.

To easily visualize the over all changes in the MIR region, spectrum for selected pressures are shown in Fig. 5.9. As already discussed from the lowest pressure data, the fundamental T_{1u} modes of C_{60}^{-} shows doublet splitting at near ambient conditions and these modes are presented for selected pressures in Fig. 5.10. The $T_{1u}(1)$ is strongly overlapped by the counterion modes, as illustrated in Fig. 5.11. Apparently, also the $(Ph_4P)^+$ cation mode undergoes pressure-induced changes, which complicates the analysis of this mode. To investigate the pressure dependence of the vibrational

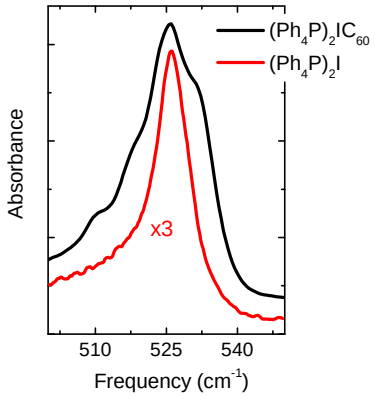

Figure 5.11: Absorbance spectra of $T_{1u}(1)$ mode of $(Ph_4P)_2IC_{60}$ in comparison with of $(Ph_4P)_2I$.

modes, the frequency positions of the vibrational modes were extracted by fitting the modes with Lorentzian functions. The pressure-dependent frequencies of four fundamental T_{1u} vibrational modes are plotted in Fig. 5.12. It is obvious that all the T_{1u} modes show doublet splitting at near-ambient conditions and harden with increasing pressure. These vibrational modes do not exhibit any pressure-dependent anomaly in contrast to the temperature dependence which shows an anomaly in the range 125–150 K [1, 2]. This can be because with lowering temperature, the modes remain sharp. Also the temperature dependence on $(Ph_4P)_2IC_{60}$ [1, 2] were measured with very high resolution and moreover the vibrational modes broaden substantially under pressure which can mask any subtle anomaly especially when the modes are broad doublets. Fig. 5.11 shows the pressure dependence of the mode at 518 cm^{-1}, which is a cation mode that coincides with the position of the $T_{1u}(1)$ mode.

The other important mode observed in the FIR region is the $G_u(1)$ mode at 398 cm^{-1} which is shown in Fig. 5.13 (a) for selected pressures. This mode is a singlet mode at lowest pressure which undergoes a two-fold splitting around 2 GPa. This can be clearly seen in Fig. 5.13 (d) which shows the frequency dependence of the $G_u(1)$ mode for different pressures. In general the modes with increasing pressure undergoes broadening and lose intensity. In contrast to this general scenario the vibrational mode at 509 cm^{-1} (see Fig. 5.13 (b)) softens with increasing pressure. Fig. 5.13 (c) shows frequency position of the mode with respect to pressure. Moreover the intensity of this mode steadily increases with increasing pressure and remains sharp until the highest measured pressure. These observations are consistent with the lowering temperature [1] in which the $G_u(1)$ mode undergoes a doublet splitting at 150 K and the mode at 509 cm^{-1} indicates softening behavior. According to group theory, a two-fold splitting of the G_u mode is expected as the system settles for a lower symmetry.

All the other vibrational modes observed in the MIR region are shown in Fig. 5.14 for selected pressures. There are several modes in this region and the pressure dependence

Table 5.2.: Vibrational modes of $(Ph_4P)_2IC_{60}$ with their pressure dependence and assignments. The strength of the modes is specified as strong (s), medium (m), and weak (w).

Mode position (at $\sim$ 0.1 GPa) (cm^{-1})	Pressure dependence	Strength	Assignment
398	hardens, doublet above 2 GPa	w	$G_u(1)$
509	softens	w	-
525	hardens	s	cation
517, 533	doublet, hardens	m,s	$T_{1u}(1)$
576, 578	doublet,hardens	s,m	$T_{1u}(2)$
619	hardens, doublet above 2 GPa	w	cation
665	sharpens, hardens, doublet $\sim$ 2 GPa	w	-
689, 695	doublet, hardens	s,m	cation
721, 726	doublet, hardens, triplet above 2GPa	s,s	cation
756	slope change above 2 GPa	s	cation
844, 848	doublet, hardens	w,w	C_{60}^-
975	gains intensity, hardens	w	cation
998	doublet above 2 GPa, hardens	m	cation
1072	hardens	w	C_{60}^-
1108, 1114	doublet, hardens	s,s	
1177, 1182	doublet, hardens	w,w	$T_{1u}(3)$
1201	hardens, undetectable above 3 GPa	w	-
1320	hardens, doublet at very high P	w	cation
1364, 1395	doublet at low P;hardens	w,s	$T_{1u}(4)$
1435, 1440	hardens, doublet	s,s	cation
1482	hardens, doublet above 2 GPa	m	cation
1585	hardens, sharp up to high P	m	cation
3047, 3056, 3076, 3088	multiplet, hardens	m,s,w,w	-

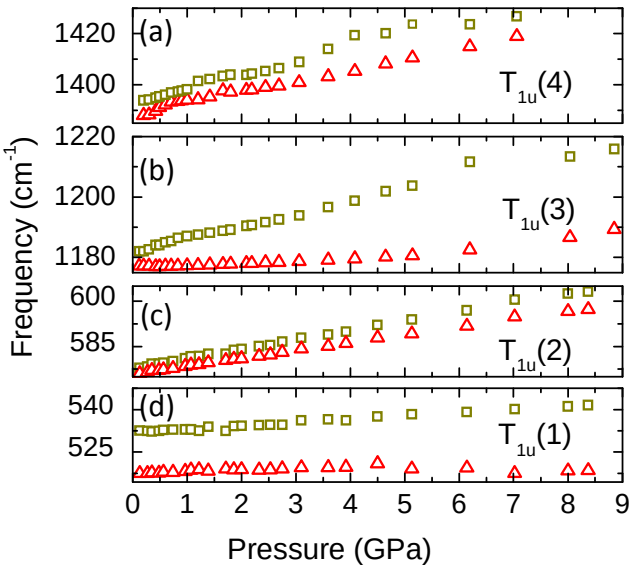

Figure 5.12.: Pressure dependence of frequency positions of the T_{1u} modes of $(Ph_4P)_2IC_{60}$.

of the prominent modes will be discussed. The pressure dependence of all the observed vibrational modes in the FIR and MIR region is summarized in Table. 5.2. The frequency positions of all the vibrational modes with increasing pressure is plotted in Fig. 5.15. The vibrational mode at 619 cm^{-1} shown in Fig. 5.14 (a) originating from the cation is a singlet at the lowest pressure and undergoes a doublet splitting above 2 GPa. Whereas this mode on lowering temperature [1] shows no splitting. The vibrational mode at 665 cm^{-1} [see Fig. 5.14 (b)] is attributed to C_{60}^- is a weak mode but gains intensity with increasing pressure and remains sharp until highest measured pressure. The doublet positioned around 690 cm^{-1} arising from cation hardens with increasing pressure [see Fig. 5.14 (c)]. Around 723 cm^{-1} is a cation mode which is a doublet at the lowest pressure and undergoes a three-fold splitting above 2 GPa. The doublet mode at 846 cm^{-1} [see Fig. 5.14 (e)] is skeptically attributed to C_{60}^- mode [3] which harden with pressure. The vibrational mode at 1072 cm^{-1} arising from C_{60}^- and the doublet mode around 1110 cm^{-1} hardens with increasing pressure. The vibrational mode at 1320 cm^{-1} whose origin is not very clear shows a doublet splitting above 2 GPa. The cation mode at 1482 cm^{-1} also undergoes a doublet splitting above 2 GPa which is shown in Fig. 5.14 (j). Finally there is the intense doublet around 3050 cm^{-1} which has weak modes on the high frequency side at 3076 and 3088 cm^{-1} (see Fig. 5.14 (l)). On increasing pressure this multiplet show different

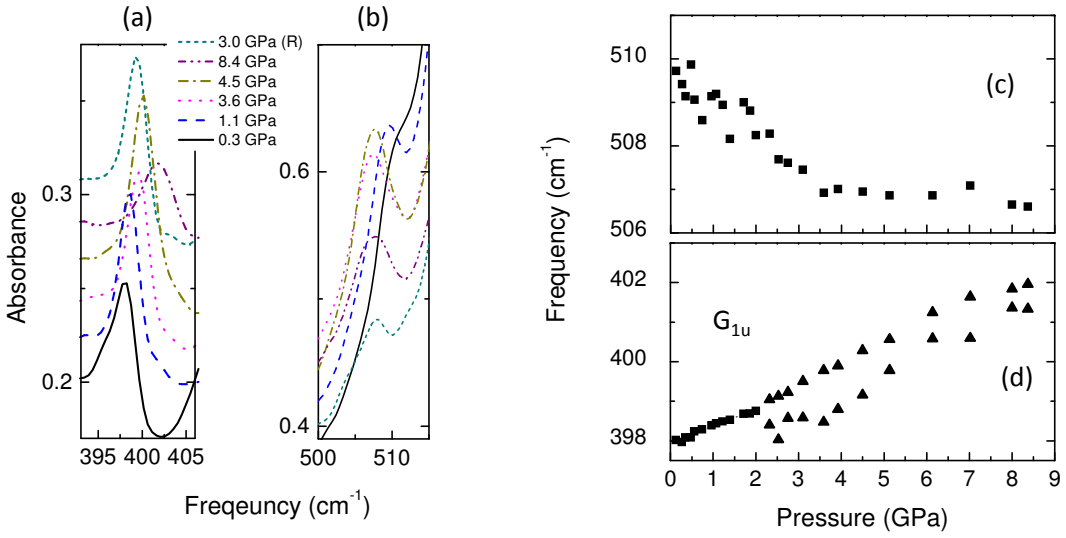

Figure 5.13.: (a)-(b) Absorbance spectra of the vibrational modes of $(Ph_4P)_2IC_{60}$ in FIR region for selected pressures (shifted for clarity) and (c)-(d) their corresponding pressure dependence.

pressure coefficient; this could be because they might have originated from different sources. Thus the frequency *versus* pressure plot shows crossover for these multiplet modes which is due to the different pressure coefficient. And the weak mode on the higher energy side can not be observed at higher pressure. The splitting is not only observed in C_{60} modes but also in cation modes, this implies that the symmetry change is at the bulk level.

The pressure-dependent behavior of the vibrational modes in the FIR and MIR region can be summarized as:

- All the vibrational modes show hardening behavior. The vibrational mode at 509 cm^{-1} softens as an exception.
- In general the vibrational mode broadens and looses intensity under pressure, nevertheless there are some exception to this. Vibrational modes at 665 cm^{-1}, 975 cm^{-1}, and 1585 cm^{-1} remain sharp until the highest measured pressure.
- Vibrational modes at 398 cm^{-1}, 619 cm^{-1}, 665 cm^{-1}, around 723 cm^{-1}, 998 cm^{-1}, and 1482 cm^{-1} undergo splitting above 2 GPa.

Splitting of vibrational modes is an indication of symmetry change that the molecule undergoes under external factors such as pressure or temperature. In $(Ph_4P)_2IC_{60}$ with

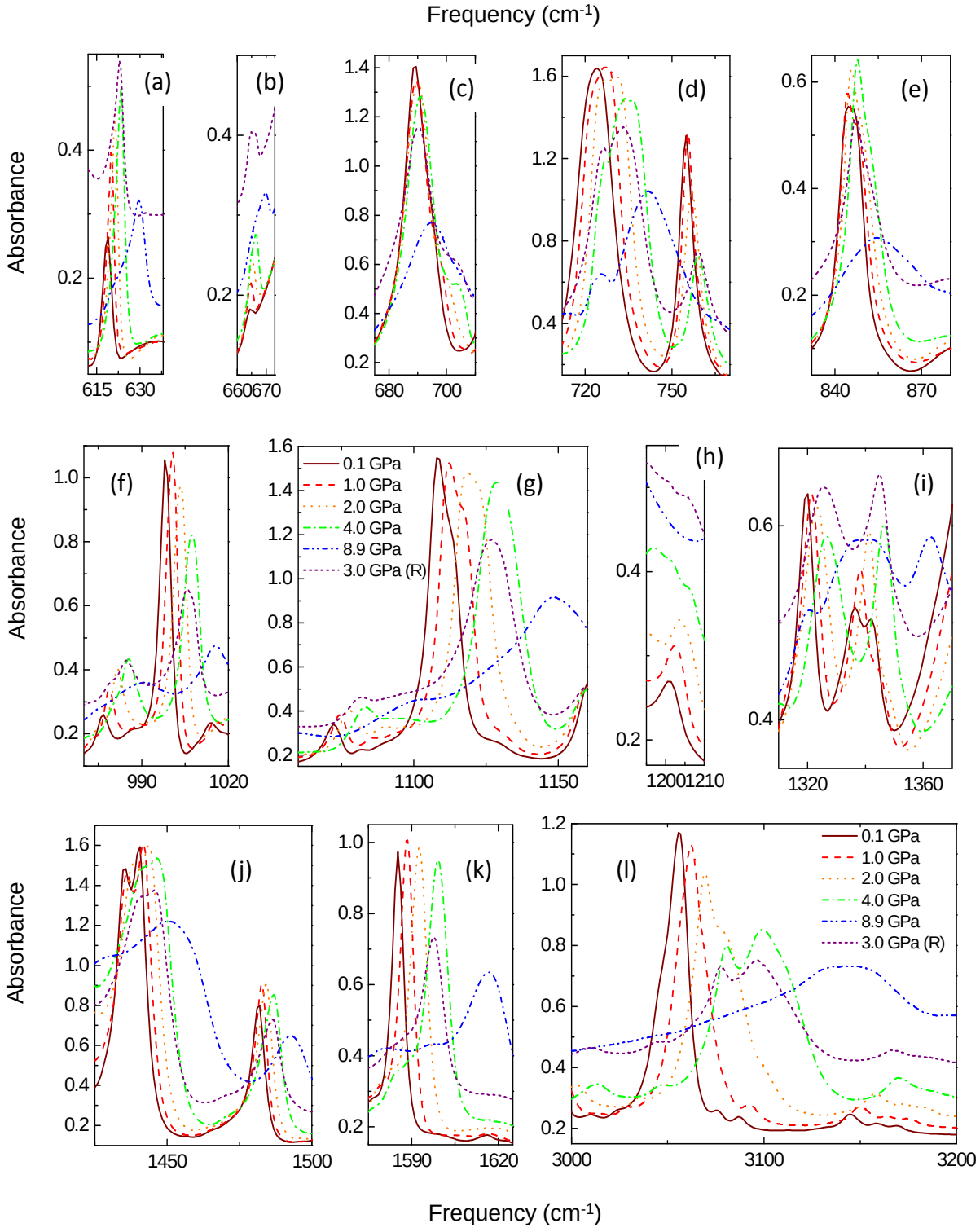

Figure 5.14.: Infrared vibrational modes of $(Ph_4P)_2IC_{60}$ for selected pressures.

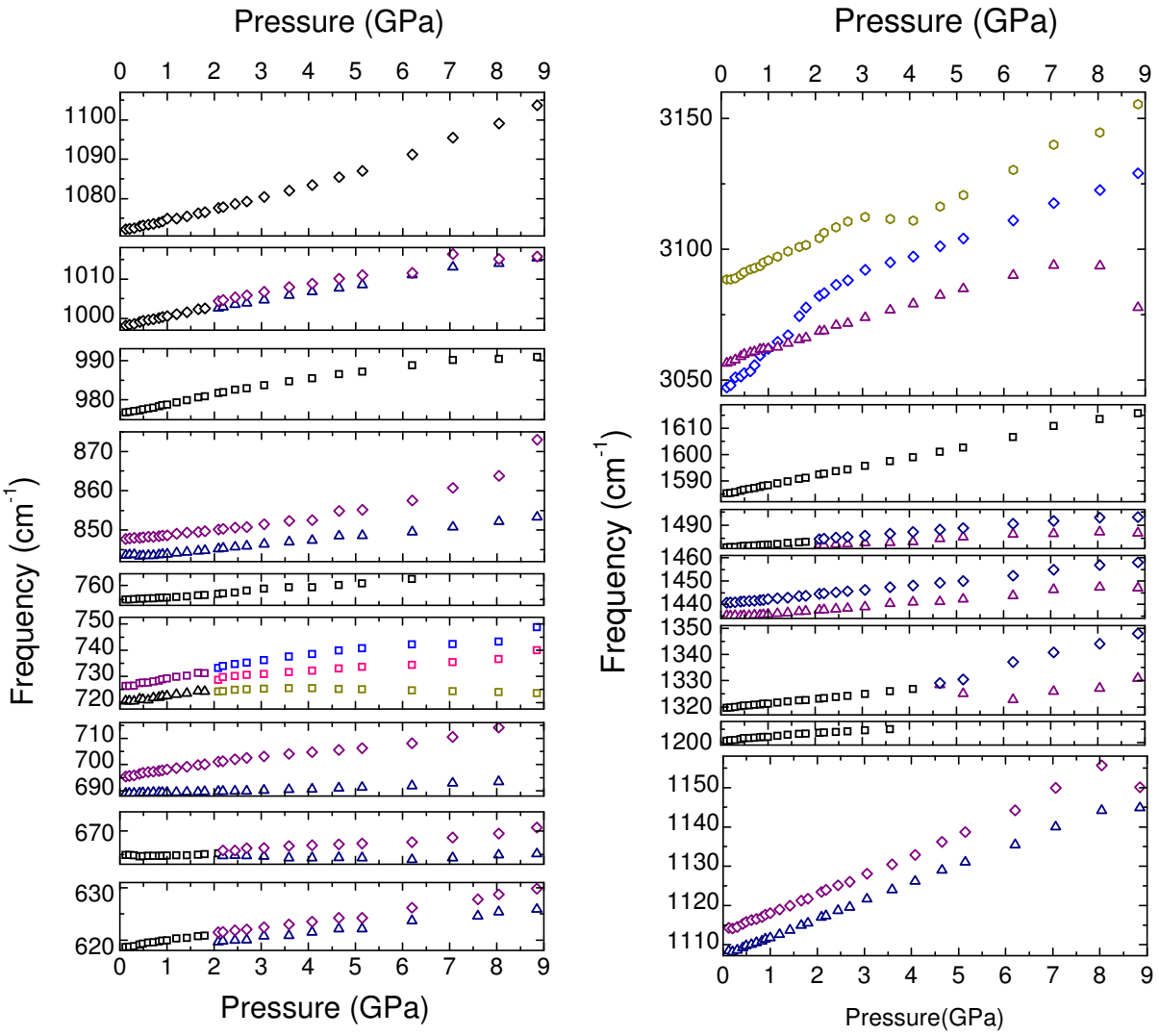

Figure 5.15.: Frequency dependence of the vibrational modes of $(Ph_4P)_2IC_{60}$ with pressure.

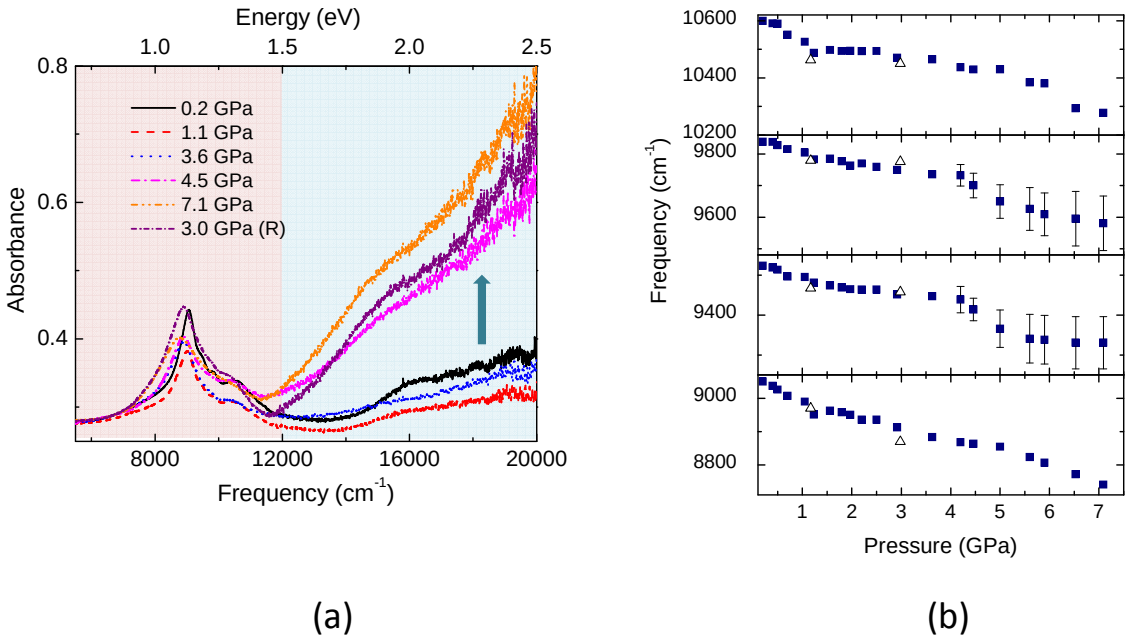

Figure 5.16.: (a) NIR-visible spectra of $(Ph_4P)_2IC_{60}$ showing the electronic transitions for selected pressures. The pink region shows the electronic and vibronic transitions and blue shows the LUMO→LUMO+1 transition. (b) Frequency positions of the electronic excitations of C_{60}^- as a function of pressure. The reversibility is illustrated by the measurement done during pressure release (open symbols)

increasing pressure several C_{60}^- and cation modes undergo splitting above 2 GPa. From the near ambient condition data, it has been established that $(Ph_4P)_2IC_{60}$ possesses dynamic Jahn-Teller distortion with the symmetry D_{5d} or D_{3d}. On increasing pressure $(Ph_4P)_2IC_{60}$ undergoes a transition to static state with D_{3d} or lower symmetry. The molecular deformation lifts the degeneracy of the LUMO by the electron-phonon interaction and splitting of the energy levels, which result in static Jahn-Teller distortion.

Pressure dependence of the electronic/vibronic transitions

The pressure-dependent NIR-visible spectrum of $(Ph_4P)_2IC_{60}$ is shown in Fig. 5.16 (a). The excitations between 9000 cm^{-1} – 12000 cm^{-1} show a red shift with increasing pressures. These features are reversible on releasing pressure. The pressure dependence of the excitations are shown in the Fig. 5.16 (b). Since the excitations broaden at higher pressure, the error bars are larger above 4 GPa as represented in Fig. 5.16 (b). The softening behavior of these electronic and vibronic excitations can be attributed

to the reduction of the separation of the electronic states as the lattice compresses under pressure.

The visible absorbance feature above 12000 cm^{-1} is also shown in Fig. 5.16 (a) (blue background), with increasing pressure these feature can be speculated to show a red shift similar to the behavior of electronic and vibration excitations. There is an irreversible change above 4 GPa which is marked by an arrow in Fig. 5.16 (a). Nevertheless it is hard to make conclusive remarks as the complete feature is not observed in the visible region and measurable frequency is limited. Higher energy pressure-dependent measurements are needed in order understand the pressure dependence of the feature observed in the visible region.

5.6. Summary

Single crystals of $(Ph_4P)_2IC_{60}$ were successfully synthesized by electrocrystallization and characterized by ATR-FTIR spectroscopy. High-pressure infrared transmission measurements over a broad frequency range up to 9 GPa were performed. In summary, the T_{1u} modes of C_{60}^- are split into doubled at the lowest pressure exhibiting the dynamic nature of the Jahn-Teller effect. The NIR spectrum also testifies the dynamic nature of Jahn-Teller effect. This can be inferred from the splitting of the vibrational modes of C_{60}^- and cation around 2 GPa. In the NIR-visible region, four absorption bands are observed and one is interpreted as optically allowed excitation between the $t_{1u} \rightarrow t_{1g}$ levels and others as higher lying vibronic transitions. The optically allowed transition is assigned to $e_{1u} \rightarrow e_{1g}$, which corresponds to either D_{5d} or D_{3d} symmetry. On applying pressure on $(Ph_4P)_2IC_{60}$ the C_{60}^- undergoes a dynamic-to-static Jahn-Teller transition around 2 GPa. The driving force of the transition can be due to the streric crowding of the C_{60}^- and cation with applied pressure.

6. Tuning the Mott-Jahn-Teller insulator by external pressure

6.1. Introduction

The aim of the work presented in this chapter is to probe the intriguing optical and electronic properties of A_4C_{60} (A = K, Rb) under pressure, searching for clear spectroscopic evidence of an insulator-to-metal transition. An enormous volume of contradicting data are discussed in the literature on insulator-to-metal transition on A_4C_{60} under pressure. With the high-pressure infrared investigation on A_4C_{60} (A = K, Rb), it is possible to tentatively identify the driving force of the insulator-to-metal transition. In addition, the Jahn-Teller dynamics involved in C_{60}^{4-} is of great interest to investigate, as it is known to govern the major properties of A_4C_{60}.

6.2. Literature review: insulator-to-metal transition in A_4C_{60}(A = K, Rb)

Experimental and theoretical works confirmed the Mott-Jahn-Teller insulator property of A_4C_{60} at ambient conditions. Efforts have been made to tune A_4C_{60} compounds to a metallic state under external pressure. Many groups have shown interest in carrying out high-pressure studies on A_4C_{60} for more than a decade. In spite of the large volume of the literature, it is not fully understood if A_4C_{60} undergoes an insulator-to-metal transition under high pressure and also the underlying mechanism. A concise overview on the important literatures in the chronological order is discussed here prior to presenting results of high-pressure infrared measurements on A_4C_{60}.

The very first insulator-to-metal transition was reported by Kerkoud *et al.* from ^{13}C- NMR in Rb_4C_{60} [114]. They discuss that the band structure evolves from a narrow indirect gap semiconductor to semi-metal under pressure around 8-12 kbar. At 8 kbar coexistence of metallic and insulating states are reported. Several high pressure studies were published in the following years. Sabouri-Dodaran *et al.* [115] from XRD

data on Rb_4C_{60} reported a transition around 0.5 – 0.8 GPa preserving the tetragonal symmetry. From theoretical calculations, they suggest that the pressure-dependent position of C and Rb atoms. An abrupt jump in compressibility under pressure was attributed to the migration of Rb atoms with the help of the theory. Additionally, they present the theoretical pressure dependence of the band width (W). Around the observed insulator-to-metal transition W is 0.5–0.55, and thus the critical $(U/W)_c$ is between 1.5–2.5. Huq *et al.* [116] from XRD under pressure on Rb_4C_{60} reported a tetragonal-to-orthorhombic phase transition around 0.4 GPa. It is suggested that the ordered orthorhombic phase becomes conducting only with further increase in pressure as the interfullerene distance decreases. They ascribe the discrepancy of their results with previous XRD results to the data analysis since only the low order peaks were taken into account and not the complete diffraction pattern was refined by Sabouri-Dodaran *et al.* The ordered phase was recently identified as *Immm* below 623 K [85]. Iwasiewicz-wabnig *et al.* [117, 118] carried out direct electric resistance measurements up to 2 GPa in the temperature range of 90–450 K and observed a sudden drop in resistance in the orders-of-magnitude at around 0.3–0.8 GPa but no clear metallic behavior was reported. However some samples showed a metallic behavior at 450 K and 0.2–0.3 GPa [118], which is speculated to be due to the phase separation of Rb_4C_{60} into Rb_3C_{60} (metallic phase) and Rb_6C_{60} at elevated temperature. Bellin *et al.* [119] carried out Raman measurements on Rb_4C_{60} up to 8 GPa and reported 3 anomalies; a low pressure structural anomaly at 0.6 GPa, a subtle second structural anomaly at 1.7 GPa, and molecular deformation at 4 GPa. A recent high pressure Raman measurement on Rb_4C_{60} up to 13 GPa reports a reversible phase separation scenario starting at 1 GPa and completing at 8 GPa [120, 121]. In this article, they have addressed the earlier experimental findings on insulator-to-metal transition in A_4C_{60} on the basis of phase separation phenomena. Although the phase separation theory explains reasonably many of the previous high-pressure experimental results, it is yet to be supported by any other experimental evidence for the presence of the metallic Rb_3C_{60} phase under high pressure. In this project, high-pressure infrared measurements were carried out on well characterized Rb_4C_{60} and K_4C_{60} in order to address the insulator-to-metal transitions and also investigate the driving mechanism of the transition. Furthermore, it is possible to comment on the phase separation of Rb_4C_{60} under pressure, since appearance of any new phases can be detected from the infrared active phonons.

6.3. A_4C_{60}: Mott-Jahn-Teller insulator

Tosatti and co-workers [122–125] have explained the property of A_4C_{60} (A = K, Rb) as nonmagnetic Mott-Jahn-Teller insulator at ambient conditions. A_4C_{60} is partially filled system with four electrons, which according to simple band theory is predicted as a metal. Furthermore, according to the Hund's rule it could be expected that the molecular ground state of A_4C_{60} to have highest spin S = 1, which would result in some sort of magnetic ground state. A brief insight into the crystal structure and the molecular orbital configuration is helpful to explain the Mott-JT insulating property of A_4C_{60}.

6.3.1. Crystal structure

The A_4C_{60} (A = K, Rb) crystalizes in body-centered-tetragonal (bct) structure with $I4/mmm$ space group [83] and lattice constants a = b = 11.9783 Å, and c = 11.035 Å [85]. The crystal structure of A_4C_{60} (A = K, Rb) is shown in Fig. 6.1. The bct structure is orientationally disordered at ambient conditions.

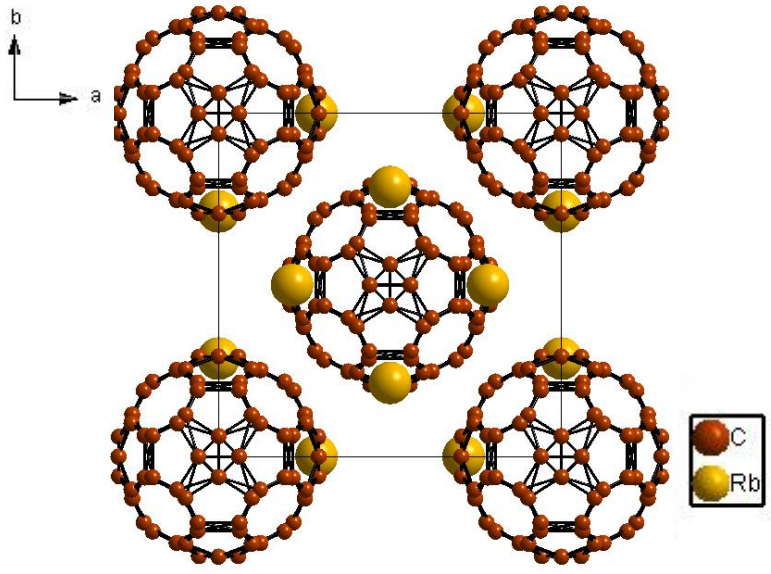

Figure 6.1.: Crystal structure of A_4C_{60} (A = K, Rb)

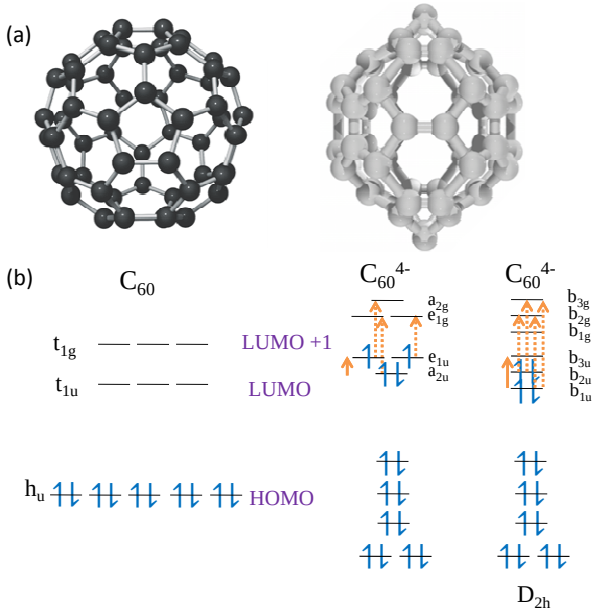

Figure 6.2.: (a) Geometric [29] and (b) electronic structure of pristine C_{60} and C_{60}^{4-} [107, 108]. The LUMO and LUMO+1 of C_{60}^{4-} are split due to JTE. The dotted arrow represents the optically allowed LUMO→LUMO+1 excitation and the solid arrow represents the t_{1u} interband transition.

6.3.2. Molecular orbital of C_{60}^{4-}

In icosahedral C_{60}, both t_{1u} and t_{1g} are triply degenerate orbitals. Addition of four electrons in C_{60}^{4-} results in a number of different electronic configurations. Two possible configuration of molecular orbitals of C_{60}^{4-} is presented in Fig. 6.2 (b). For one of the possible configuration, the JT distortion splits the LUMO into a non-degenerate lower a_{2u} level and doubly degenerate higher lying e_{1u} orbitals and similarly for LUMO+1 (t_{1g}) into doubly degenerate e_{1g} and single a_{2g} levels. Fig. 6.2 (a) shows molecular distortion for C_{60}^{4-} in which the carbon double bonds in the hexagonal faces are elongated and weakened due to the addition of extra charges [85].

Lawson *et al.* have discussed different possibilities and have narrowed down to two possible electronic orbital configurations for C_{60}^{4-}, but they have not discussed the possible molecular symmetry for these configurations [107]. Klupp *et al.* have discussed the splitting of the LUMO and LUMO+1 levels along with the possible symmetry of the C_{60}^{4-} molecule [33].

Rolling back to the explanation about the insulating property of A_4C_{60}(A = K, Rb), both strong correlations and JT effects are essential for the understanding of the insulating properties at ambient conditions. In bct structure, the crystal field effect is

not strong enough to split the degeneracy so as to produce a band insulator. Thus, the Mott insulating state is driven by the intermolecular and intramolecular electron correlations. The strong Coulomb repulsion (U) is the reason to drive the system to a Mott insulating state, and the Jahn-Teller splitting overrides the Hund's rule, making it nonmagnetic [122]. The Mott insulators are usually discussed in terms of U/W. In case of A_3C_{60} and A_4C_{60}, the U/W ratios are identical while in general the former is metallic and the latter is insulating. Moreover, A_3C_{60} can even become a superconductor at low temperature [126]. Among the class of A_4C_{60}, Na_4C_{60} has a stable fcc structure at high temperature and is the only paramagnetic metal in contrast to the insulating K_4C_{60}, Rb_4C_{60}, and Cs_4C_{60}. Na_4C_{60} has a unique 2D polymeric structure wherein each fullerene molecule is linked to four neighbors by single covalent C-C bonds in a plane [127]. The origin of the metallic behavior of the Na_4C_{60} is attributed to the polymerization and the complete charge transfer [128]. Thus, Na_4C_{60} does not fall under the class of compounds that are discussed in this chapter.

The optical measurements performed by Knupfer *et al.* have shown a direct band gap of 0.5–0.6 eV in K_4C_{60} [129]. The insulating state is non-magnetic with a spin gap to the lowest triplet exciton of 0.1–0.14 eV [114, 130]. Capone *et al.* have pointed out that the close agreement between the calculated spin and optical gaps of C_{60}^{4-} (0.1 and 0.5 eV) with the corresponding experimental value of K_4C_{60} and Rb_4C_{60} are a strong spectroscopic evidence in favor of the Mott-JT state [123]. It is expected that the Mott-JT insulating state can be destroyed by external pressure by tuning the W, which causes the intra-molecular interaction to disappear giving way to an insulator-to-metal transition.

6.4. High pressure investigation on A_4C_{60}

High-pressure infrared measurements on A_4C_{60} (A = K and Rb) up to 8 GPa were performed over a broad frequency range from FIR to visible at room temperature. K_4C_{60} was measured in transmission mode and Rb_4C_{60} in reflection/transmission mode with Syassen-Holzapfel and Cryo DAC mega, respectively. The synthesis of K_4C_{60} and Rb_4C_{60} samples used for this project are discussed in detail in Chap. 4. Details of the test measurements carried out on A_4C_{60} are presented in Chap. 3.4.7.

6.4.1. High-pressure measurements on Rb_4C_{60}

The reflectivity $R(\omega)$ measurements on Rb_4C_{60} pellets at the sample-diamond interface in the FIR-MIR region under pressure were performed and the spectra for selected

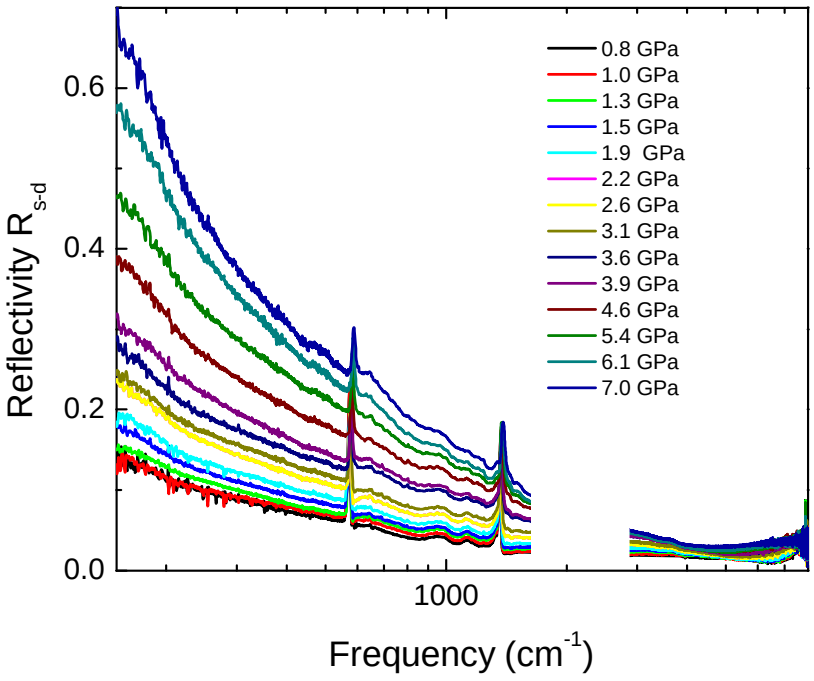

Figure 6.3.: Measured absolute reflectivity R(ω) on Rb_4C_{60} pellet in the FIR and MIR region under pressure.

pressures are shown in Fig. 6.3. The CuBe gasket was measured as the reference for the reflection measurements. As the surface quality of the Rb_4C_{60} pellet was not optimum, reflection measurements was not possible in the NIR-visible region. Thus measurement were made in transmission mode by filling the DAC with a mixture of Rb_4C_{60} powder and pressure transmitting medium. The reference for transmission measurements were measured by filling the DAC with the pressure transmitting medium. The transmission and absorption spectra of Rb_4C_{60} in the NIR-visible region for selected pressures are plotted in Fig. 6.4.

6.4.2. High-pressure measurements on K_4C_{60}

Infrared transmission measurements over a broad frequency (100–20000 cm^{-1}) range up to 7 GPa were performed with K_4C_{60} samples which have about $\sim$ 5 % K_3C_{60} impurities. The mid-infrared absorbance spectra for selected pressure are shown in Fig. 6.5. The over all quality of the reflection spectra is better compared to the transmission spectra in case of A_4C_{60} in FIR-MIR regions. Nevertheless, the $T_{1u}(2)$ phonon was clear and could be followed with pressure. The NIR-visible absorbance

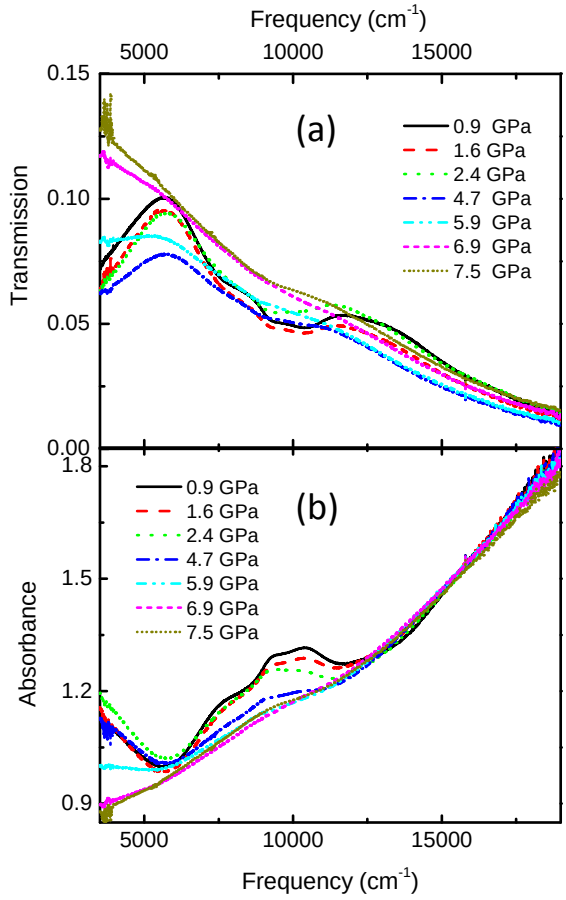

Figure 6.4.: (a) Transmission and (b) absorption spectra of Rb_4C_{60} for selected pressures in the NIR-visible region.

spectra of K_4C_{60} for selected pressures are plotted in the Fig. 6.12, with an inset showing the region containing the interband transitions.

6.5. Results and discussion

In principle, the Rb_4C_{60} and K_4C_{60} should behave similarly under pressure due to their very similar electronic and crystal structures. However, most of the high-pressure studies published are carried out on Rb_4C_{60} samples and there are no clear reasons for the choice of Rb_4C_{60} over K_4C_{60}. Interestingly the quality of the data in this project obtained by reflection of Rb_4C_{60} is better than the transmittance spectra of K_4C_{60} especially in the FIR-MIR region. Thus the discussion will be based extensively on the Rb_4C_{60} spectra for the FIR-MIR region. For both Rb_4C_{60} and K_4C_{60}, the NIR-visible region of the spectra were measured by transmission and thus a direct

comparison of the spectra in this region is possible.

Far- and mid-infrared region

The mid-infrared absorption spectra of K_4C_{60} under pressure shown in Fig. 6.5 has no remarkable changes in the low frequency region. The broad MIR band around 3000 cm^{-1} can be assigned to the interband transition within the split LUMO (t_{1u}) levels (see Fig. 6.2 (b)). With increasing pressure, the MIR band shows weak softening behavior. At higher frequency, above 7000 cm^{-1}, there is a signature of an absorption band, this will be discussed later in comparison with the Rb_4C_{60} spectrum.

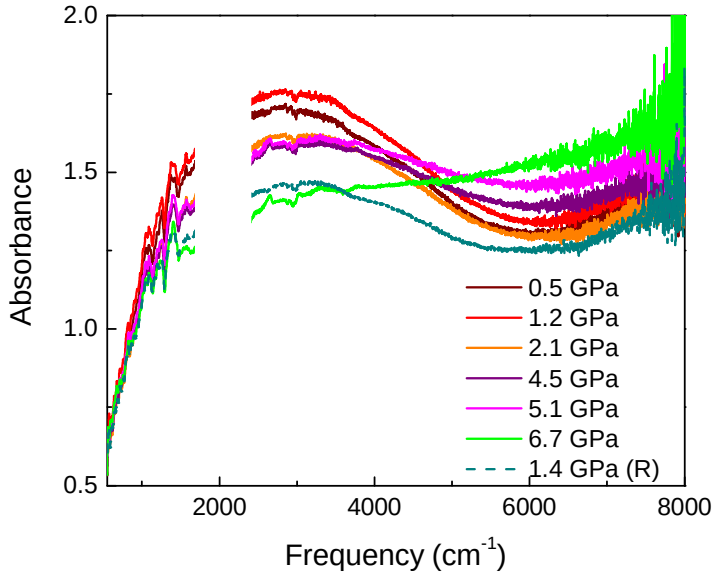

Figure 6.5.: Mid infrared absorption spectra of K_4C_{60} for selected pressure. Spectrum measured during pressure release is marked by (R)

The reflectivity spectra (FIR-MIR region) of Rb_4C_{60} are fitted with Drude-Lorentz model with a Fano approach in order to account for the asymmetric phonon modes. To fit the reflectivity spectra, the following procedure was adopted. The pressure dependent high-frequency permittivity (ε_∞) that was used in the fitting was determined from the Clausius-Mossotti relation [131],

$$\frac{\varepsilon_\infty(P)-1}{\varepsilon_\infty(P)+2} = \frac{\alpha}{3\varepsilon_0 V(P)} \tag{6.1}$$

where $\varepsilon_0 = 8.854 \times 10^{-12}$ F/m, α is electronic polarisability which is obtained from the lowest pressure data and is assumed to be constant with increasing pressure, and *V(P)* is change in volume with increasing pressure.

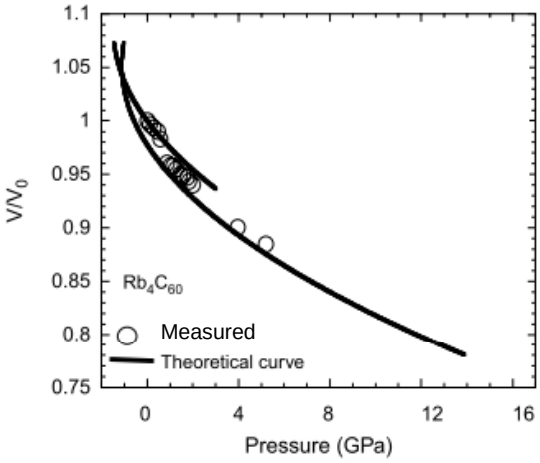

Figure 6.6: A comparison between experimental and theoretical equation of state of Rb_4C_{60} [132].

At ambient conditions, the unit cell volume of Rb_4C_{60} is 1583.3 Å^3 [85] and the static dielectric constant for C_{60} is 4.0 – 4.5 [133, 134]. For the lowest measured pressure (0.8 GPa) the FIR-MIR data were fitted with Drude-Lorentz model, the corresponding optical conductivity was obtained. The NIR-Visible spectrum was suitably manipulated to match the optical conductivity (σ_1) obtained from FIR MIR data around ∼7000 cm^{-1} by using the Eq. 3.8. The best ε_∞ value that describes the 0.8 GPa spectrum between 100 cm^{-1} and 20000 cm^{-1} of Rb_4C_{60} is in the range 3 – 3.2. Thus, using these values we obtain α from the Eqn. 6.1 to be 1.674 × 10^{-38} Å^3 at ambient conditions. The change in volume of Rb_4C_{60} with pressure has been reported separately from a X-ray diffraction experiment [116] and coherent - incoherent X-ray scattering [132]. Sabouri-Dodaran *et al.* [115] showed that the experimental results are in good agreement with the theoretical equation of state with increasing pressure as shown in Fig. 6.6. From the available information, the change in volume with increasing pressure was extracted and is plotted in Fig. 6.7. The overall volume change of Rb_4C_{60} in the measured pressure range is about 300 Å^3. For every pressure the ε_∞ was calculated by taking into account the corresponding volume of Rb_4C_{60}. The calculated value of ε_∞ is plotted with increasing pressure in Fig. 6.8 that was used for fitting the high-pressure FIR-MIR spectra. The reflectivity spectra for selected pressure along with the fit using the Drude-Lorentz model and the respective ε_∞ is shown in Fig. 6.9.

The development of the real part of the optical conductivity $\sigma_1(\omega)$ spectra of Rb_4C_{60} for different pressures obtained by fitting the measured reflectivity spectra is shown in Fig. 6.10. The low-frequency optical conductivity increases with increasing pressure. At the lowest measured pressure (0.8 GPa), the low-frequency optical conductivity has a finite value signifying a bad metal behavior. Also this Drude contribution shows an increase with increasing pressure. It was not possible to trace the transition pressure

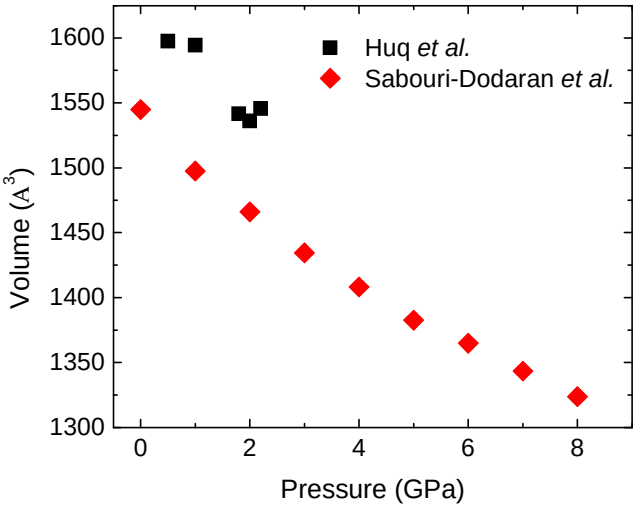

Figure 6.7.: Change in volume of Rb_4C_{60} extracted from the Huq *et al* [116] and Sabouri-Dodaran *et al* [115] results.

as the lowest possible pressure was 0.8 GPa, which according the literature review in Section. 6.2 is high enough to have a metallic phase. The optical conductivity spectra found in literature has a MIR band at around 0.5 eV (4032.77 cm^{-1}) which is attributed to the interband transition within the split t_{1u} band (see Fig. 6.2 (b)). This is also observed as a broad mid-infrared absorption band in the K_4C_{60} spectra (see Fig. 6.5). This region is very close to the diamond multiphonon absorption of the DAC, therefore it was not possible to reliably follow this region of the data under pressure. Nevertheless, this feature is seen partly in the raw reflectivity spectra of Rb_4C_{60} from visual examination, but it is not possible to carry out the analysis on this feature as it softens with increasing pressure. The band at 7300 cm^{-1} (0.9 eV) for Rb_4C_{60} in the optical conductivity spectra (see Fig. 6.10) is attributed to the transition from the LUMO (t_{1u}) to LUMO+1 (t_{1g}) as illustrated in the Fig. 6.2 (b). However, in the measured reflectivity spectrum the LUMO $\rightarrow$ LUMO+1 excitation is weak and was fitted with a single Lorentzian oscillator. With the increasing pressure the band shifts towards the lower energy which implies a lowering of the energy gap between the LUMO and LUMO+1 levels (see Fig. 6.2) with increasing pressure. In case of K_4C_{60}, this feature is see partly in the MIR region (see Fig. 6.5). In the NIR-visible absorption spectrum for both K_4C_{60} and Rb_4C_{60} the transitions can be clearly resolved, since the transmission measurement are more sensitive to the splitting compared to the reflection measurements on pellet.

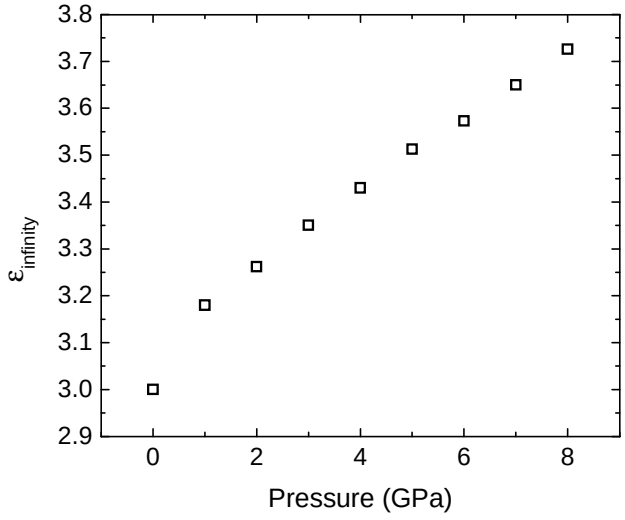

Figure 6.8.: Calculated high-frequency permittivity (ε_∞) with increasing pressure.

NIR and visible region

The NIR-visible absorbance spectra of Rb_4C_{60} for all pressures are plotted in Fig. 6.11 (shifted vertically for clarity). In this region of the spectra the higher energy side of the MIR band is observed below 5800 cm^{-1}. Above 6000 cm^{-1} there are three distinct excitations, which were fitted with one broad band in the MIR region as seen in the optical conductivity spectra (see Fig. 6.10) as discussed above. The NIR-visible absorption spectra of K_4C_{60} under pressure are identical to that of Rb_4C_{60} (see Fig. 6.12). In order to determine the assignments for these transitions, available literature will be discussed in short. The possible number of LUMO $\rightarrow$ LUMO+1 transitions according to Lawson *et al.* [107] is either three or four and according to Klupp *et al.* [33] is two and four. Furthermore, Klupp *et al.* have discussed a transition from dynamic-to-static Jahn-Teller distortion with temperature lowering which is accompanied by molecular symmetry change from D_{3d}/D_{5d} to D_{2h} and is reflected in the NIR spectrum spectrum as a twofold to fourfold splitting in K_4C_{60} but it was not well resolved in the case of Rb_4C_{60} [33]. The dynamic-to-static JT transition temperatures for K_4C_{60} and Rb_4C_{60} are at 270 K and 330 K, respectively. Also Wachiwiak *et al* have suggested that in K_4C_{60}, D_{2h} was observed to stabilize the molecular level [135]. From the presented NIR-visible data of Rb_4C_{60}, a threefold splitting is observed marked by solid arrows in Fig. 6.11 and at around 12500 cm^{-1} (marked by dotted arrow in Fig. 6.11) is a weak feature. When examining the spectra presented in Ref [33], they observe the fourth excitation at an energy around 13000 cm^{-1} at low temperature in case of K_4C_{60} while

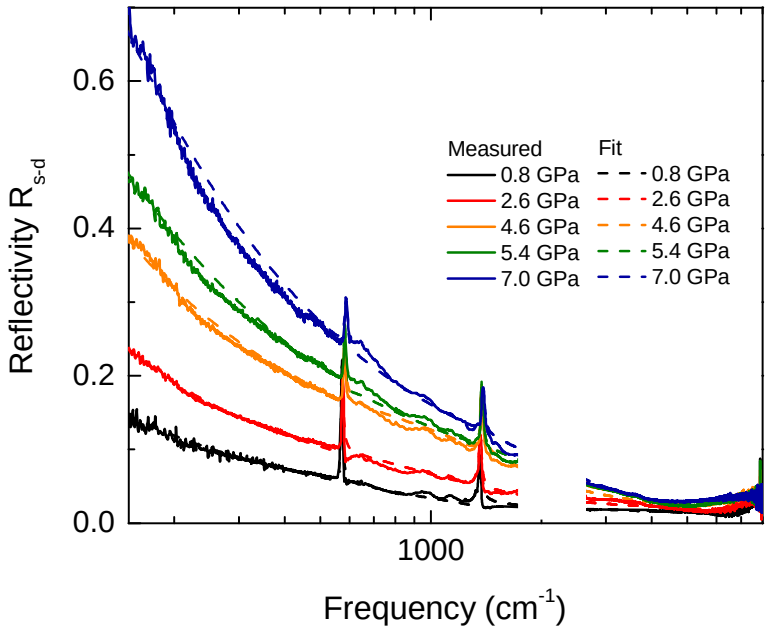

Figure 6.9.: Measured absolute reflectivity R(ω) (line) on Rb_4C_{60} pellet in the FIR and MIR region under pressure with the corresponding fitting (dashed line) using Drude-Lorentz model.

in case of Rb_4C_{60} the excitations are much broader and are not well resolved. The dynamic-to-static transition temperature for Rb_4C_{60} is at 330 K and all the presented data in this project were measured at room temperature, therefore the C_{60}^{4-} molecules must assume a static JT distortion at all measured pressures. For static C_{60}^{4-} the symmetry must be D_{2h} as presented in the Scheme in Fig. 6.2 and will have four optically allowed transitions as marked in the scheme. Thus, in this NIR-visible data the weak feature can reasonably considered as the fourth excitation (see in Figs. 6.12 and 6.11 marked with dotted arrow). It is likely that the fourth excitation is hidden by the tail of the UV absorption band. In case of K_4C_{60} the lowest pressure is at 0.5 GPa which is considerably high in case of the fullerene-based compound to induce an dynamic-to-static JT transition. Since the samples are air sensitive, it was not possible to measure any pressure lower than 0.5 GPa with the DACs used in this project. Thus the critical pressure for dynamic-to-static transition could not be determined.

With increasing pressure the NIR-Visible bands due to the LUMO $\rightarrow$ LUMO+1 excitations soften, which indicate a decrease in the separation between the energy levels. Also the tails of the MIR bands of Rb_4C_{60} and K_4C_{60} show a softening behavior meaning the split t_{1u} levels close in with increasing pressure. A decrease in the splitting

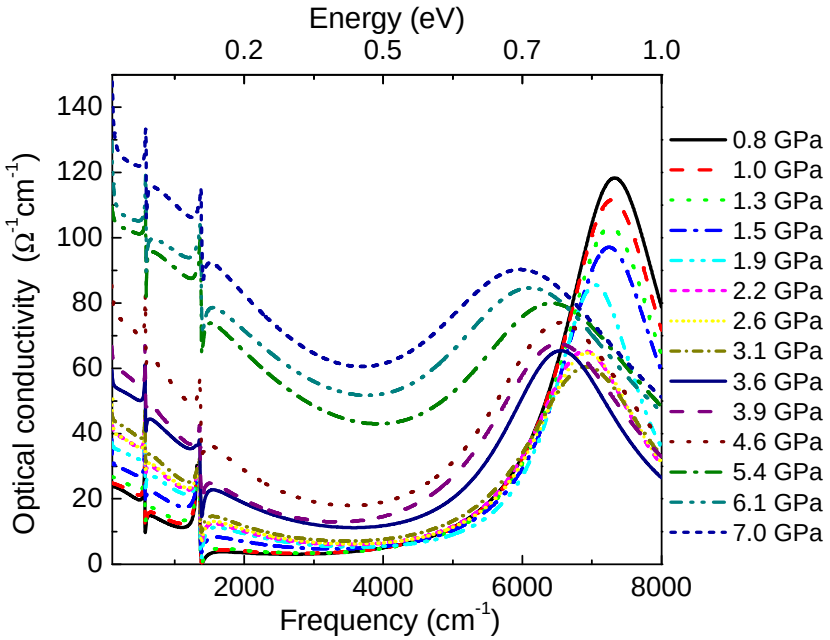

Figure 6.10.: Real part of the optical conductivity $\sigma_1(\omega)$ of Rb_4C_{60} obtained from the fitting of the reflectivity spectra with Drude-Lorentz model.

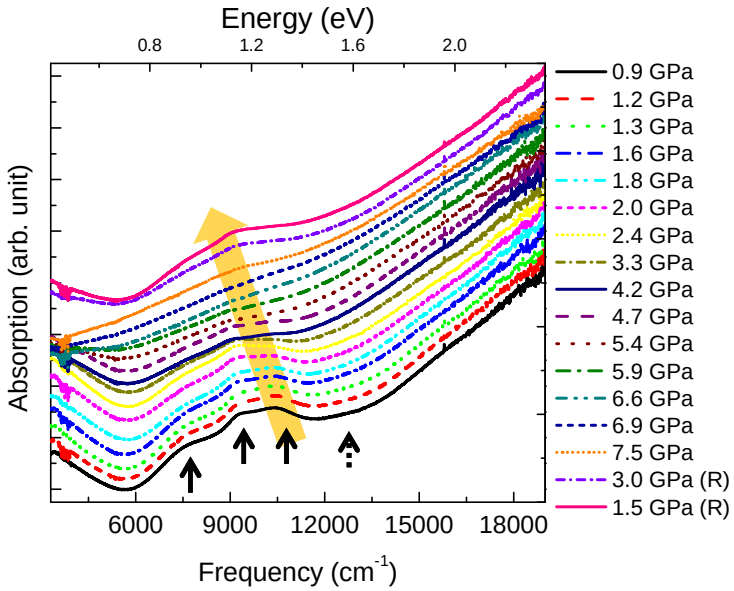

Figure 6.11.: NIR-visible absorption spectra of Rb_4C_{60}, the spectra are offset along the vertical axis for clarity. The pressure releasing are marked with (R) in the legend

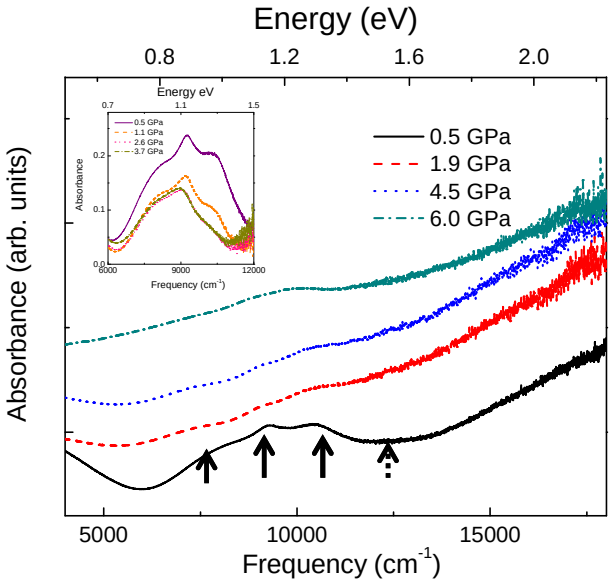

Figure 6.12.: NIR-visible absorption spectra of K_4C_{60} (shifted vertically) for selected pressures. Inset: the interband transition after linear background subtraction for selected pressures.

of the energy levels at molecular level favors the appearance of the metallic state due to the changing W under pressure. By investigating the phonon, it is possible to comment on the phase separation theory under pressure.

6.5.1. Phonons

Two of the four phonons of the neutral C_{60} are observed for Rb_4C_{60} at 575 cm^{-1} and 1350 cm^{-1} as seen in Fig. 6.14. The downshift of the $T_{1u}(4)$ mode from 1429 cm^{-1} for C_{60} to 1350 cm^{-1} for Rb_4C_{60} is due the charge transfer effects, this clearly indicated a lower symmetry than icosahedral for C_{60}^{4-}. Furthermore, the line shape of the phonons in the reflectivity spectrum are better described by Fano profile rather than a typical Lorentzian shape as illustrated in Fig. 6.13. Klupp *et al.* have reported a twofold $T_{1u}(4)$ mode at 420 K and on lowering temperature it undergoes a threefold splitting around 300 K [33] from the infrared transmittance data. Generally transmission measurements show signatures of even weak absorbance, thus to resolve the splitting of the phonon, transmission measurements are better than the reflection measurements. Although the pressure measurements were carried out at room temperature, in this data the $T_{1u}(4)$ mode is observed as doublet. The splitting of the phonons is due to the JT distortion of the C_{60}^{4-}. The oscillator width of the second branch of the $T_{1u}(4)$

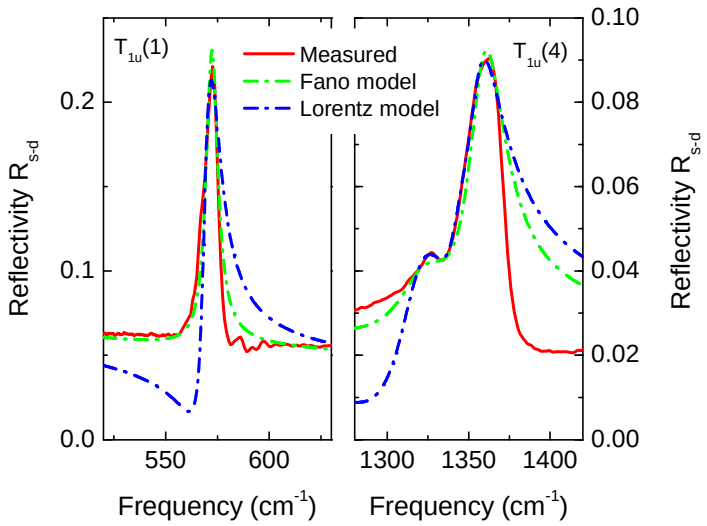

Figure 6.13.: Reflectivity R(ω) spectrum of Rb_4C_{60} showing the T_{1u} phonons and fits of these modes with Fano lineshape and Lorentz harmonic oscillator.

mode for 0.8 GPa is 33 cm^{-1}, which is broad enough to be a doublet therefore the possibility of the triplet splitting of $T_{1u}(4)$ in this data cannot be ruled out. The parameters used for fitting the phonons using Fano line shape is plotted with pressure in Fig. 6.14, the error bars indicate that the general trend with increasing pressure is reliable. The Fano resonance describes the quantum interference effect of the coupling between the discrete state and the continuum states giving rise to an asymmetric phonon line shape. The use of Fano profile for the phonons can be interpreted as the coupling of the (T_{1u}) phonon vibrations to the electronic states. The parameters of the fit evolve monotonically with increasing pressure as shown in the Fig. 6.14. The pressure dependence of the Fano parameter is very important in analyzing the coupling between the vibrational and the electronic states as it would provide an insight on the behavior of the gap itself. The Fano parameter (q) which is defined as the ratio of the optical response of the perturbed non-radiative mode to the continuum. The sign of the Fano parameter is significant as it suggests which electronic background is coupled to the vibration. In case of Rb_4C_{60}, the Fano parameter remains positive up to the highest pressure which indicates that the phonon is couple to the electronic states which is lying at lower energy that the phonons itself. At lower frequencies is the Drude conductivity to which the vibrational modes are coupled. In Rb_4C_{60} the value of q for both $T_{1u}(2)$ and $T_{1u}(4)$ phonons decreases with increasing pressure from 1.3 to 1.0 and 2.0 to 1.15, respectively. According to the discussed in chapter. 3.4.6

about the Fano resonance model, the $|q| \sim 1$, the electron and phonon contributions are comparable. In this data, at low pressure the value of q > 1 means the phonon contributions dominate the electronic contribution. With increasing pressure as the band gap closes, the contribution of the electron gets significant causing a decrease in the Fano parameter (q).

Another aim of the experiment was to check for any phase separation of Rb_4C_{60} under pressure as proposed by Yao *et al.* according to the reaction [121],

$$3Rb_4C_{60} \rightleftharpoons 2Rb_3C_{60} + Rb_6C_{60}. \tag{6.2}$$

The infrared phonons serve as a marker for the presence of the different phases in the sample, which was discussed in the chapter. 2.11. For Rb_3C_{60} phase, only $T_{1u}(2)$ and $T_{1u}(4)$ phonons are expected similar to Rb_4C_{60} and their positions are also very close to that of Rb_4C_{60}. In addition with increasing pressure the phonons shift, thus it is extremely hard to confirm the appearance of Rb_3C_{60} phase under pressure. While the Rb_6C_{60} phase shows all the four infrared phonons (refer Chapter. 2.11). In the measured spectra only $T_{1u}(2)$ and $T_{1u}(4)$ phonons are observed upto the highest pressure. Thus we do not observe the appearance of the Rb_6C_{60} phase under pressure. Therefore, we could rule out the possibility of Rb_3C_{60} phase and the phase separation theory within the measured infrared later resolution scale. In Ref [120, 121] the authors has suggested that the phase separation primarily occurs on the nanometer length scale, which might be hard to be followed in the infrared measurements as it measures the macroscopic response of the sample.

In absorbance spectra of K_4C_{60}, $T_{1u}(2)$ phonon was clearly identified and could be followed under pressure where as the $T_{1u}(4)$ phonons was hard to be followed. The $T_{1u}(2)$ phonon absorbance is shown in Fig. 6.15 (a) for selected pressures. The phonon was fitted with a Lorentz oscillators to extract the phonon frequency which is plotted in Fig 6.15 (b) for different pressures. The pressure dependence of the phonon shows a weak anomaly around 0.8 GPa and this could be assigned to the dynamic-to-static transition. In case of the NIR-Visible spectra it is believed to have static distortion already sets in at the lowest measured pressure. Hence it can be suggested that the transition can be around 0.5–0.8 GPa. Due to the smaller size of the K_4C_{60} ions, pressure is required to drive C_{60}^{4-} to static state, while the Rb_4C_{60} ions are considerably bigger which causes a static distortion even at room temperature and at ambient pressure. Thus a upper bound for the dynamic-to-static JT transition can be fixed at 0.8 GPa for K_4C_{60}.

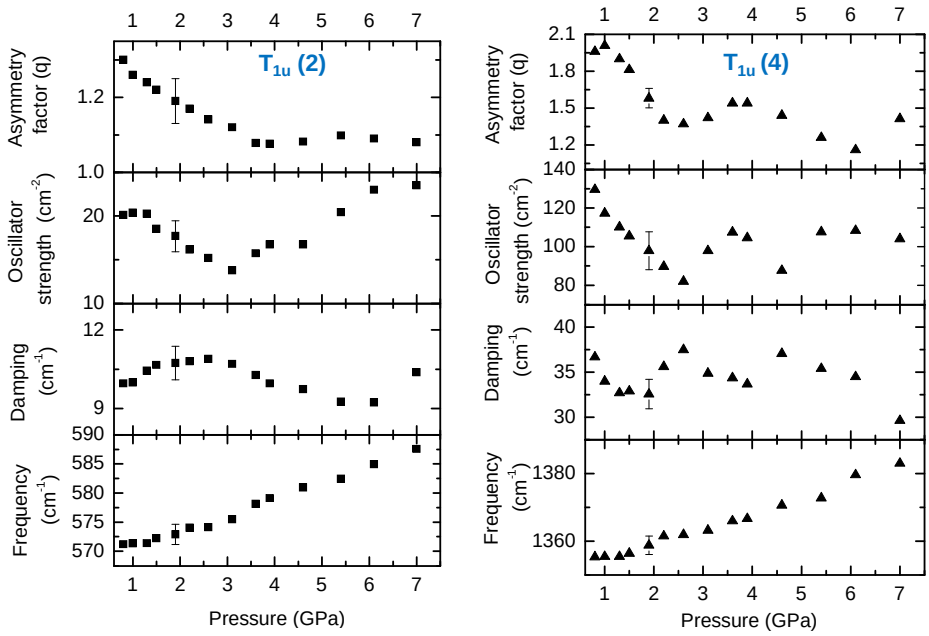

Figure 6.14.: The four parameters from the Fano model fit of the T_{1u} phonons of Rb_4C_{60} with increasing pressure.

6.6. Summary

A_4C_{60} (A = K and Rb) samples were successfully synthesis and characterized by powder XRD. High-pressure infrared measurements on the well characterized samples were performed over a broad frequency in the range 0.8 – 8 GPa. In summary, the real part of the optical conductivity of Rb_4C_{60} spectra show a Drude-like term at the lowest measured pressure. Thus Rb_4C_{60} shows a bad metal characteristics above 0.8 GPa. Furthermore, with increasing pressure the low-frequency Drude term shows a monotonic increase indicating an increase in the metallic behavior. Its is not possible to clearly determine the critical pressure of the insulator-to-metal transition due to the lack of the low pressure data. In case of the K_4C_{60} it is hard to comment on the low frequency data.

The t_{1u} interband transition at $\sim$ 3000 cm^{-1} in the K_4C_{60} spectra show a weak softening and similarly in the reflectivity spectra of Rb_4C_{60} the excitation also softens with increasing pressure. The LUMO $\rightarrow$ LUMO+1 transitions at around 0.9 eV in both Rb_4C_{60} and K_4C_{60} show a softening behavior with increasing pressure. The softening of these excitations can be attributed to the decrease in the splitting of the energy levels. From the NIR-visible spectra for K_4C_{60} and Rb_4C_{60}, it can be concluded that the C_{60}^{4-} in the measured pressure range assumes static JT distortion.

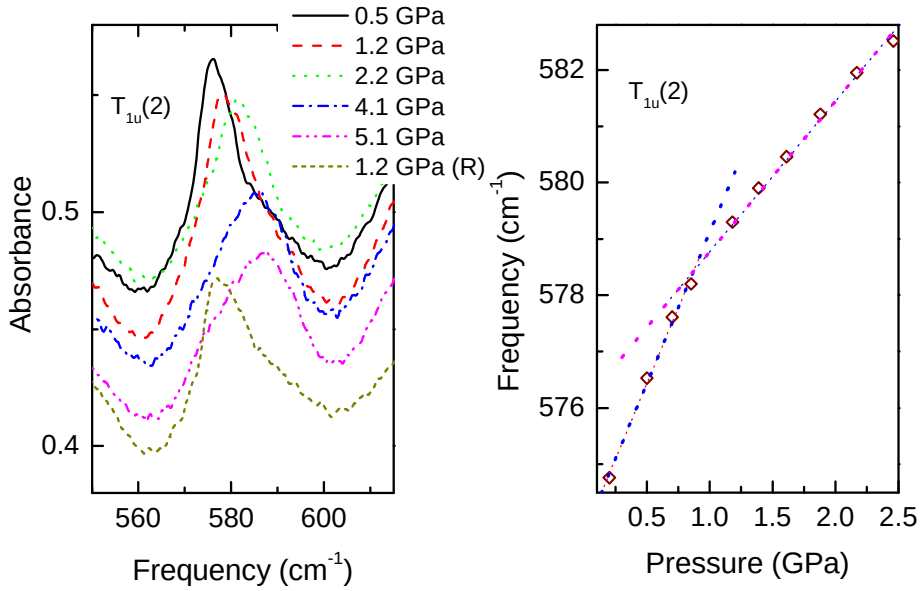

Figure 6.15.: (a) $T_{1u}(2)$ phonon spectra in K_4C_{60} for selected pressures and (b) the frequency shift of the $T_{1u}(2)$ phonon with pressure.

The phonon of the Rb_4C_{60} could be analyzed only with the use of a Fano lineshape, which indicate a coupling between the electronic and vibrational states. The pressure dependence of the Fano parameters has no significant anomaly. The $T_{1u}(2)$ phonon of K_4C_{60} shows a weak anomaly at around 0.8 GPa indicating the dynamic-to-static transition of the C_{60}^{4-}. The Fano parameter in Rb_4C_{60} under pressure for both $T_{1u}(2)$ and $T_{1u}(4)$, are 1.3 and 2.0, respectively at 0.8 GPa. As the pressure is increased the Fano parameter decreases indicating that the coupling between the discrete vibrational states and the electronic continuum gets stronger. This is due to the lowering of the energy gap between the split t_{1u} levels and between LUMO - LUMO+1, is confirmed by the shifting of the excitation towards low frequency in the NIR-Visible spectra.

The observed bad-metallic behavior of Rb_4C_{60} under pressure can be rather attributed to the changing W with increasing pressure rather than to a phase separation theory. This is because there are clear indication for the decreasing gap between the energy levels at molecular level from the NIR-visible spectra under pressure and there are no indication to believe the appearance of any new phases under pressure from this high-pressure infrared data.

7. Orientational ordering in $C_{60}{\cdot}C_8H_8$ under hydrostatic pressure

7.1. Introduction

This chapter is dedicated to investigate $C_{60}{\cdot}C_8H_8$ under hydrostatic conditions in order to determine the orientational ordering transition pressure and understand the underlying mechanism. High-pressure infrared transmission measurements up to 9.5 GPa were carried out on the rotor-stator molecular cocrystal namely $C_{60}{\cdot}C_8H_8$ with argon and helium as hydrostatic pressure transmitting media. Helium is one of the best hydrostatic pressure transmitting media available, while it can also intercalate into the $C_{60}{\cdot}C_8H_8$ lattice. Thus in addition to the pressure effects, the effect of interaction of the pressure medium is also discussed. Infrared spectroscopy is a very sensitive method to observe the symmetry changes in the molecules. Therefore, by investigating the pressure-induced splitting of the vibrational modes of $C_{60}{\cdot}C_8H_8$ it is possible to deduce the site symmetry of the molecule which can indirectly verify the space group of the ordered phase (*Pnma*), that was reported recently. This chapter has an introduction to $C_{60}{\cdot}C_8H_8$ and its properties, which is followed by the results of high-pressure studies on $C_{60}{\cdot}C_8H_8$ with argon and helium as pressure transmitting media. Finally, the phase transition in $C_{60}{\cdot}C_8H_8$ under hydrostatic conditions and its driving mechanism are discussed in detail.

7.2. Cubane

Cubane (C_8H_8) was first synthesized by Eaton and Cole [136] although they were suspicious if such a highly strained molecule can be synthesized. At ambient conditions, solid cubane has rhombohedral structure with $R\bar{3}$ space group [137] and is orientationally disordered. In general, there are two types of C-C-C bonds: sp^2 has the bond angle of 120° and sp^3 has 109.5°, any other type of C-C-C bond would decrease the stability of the structure. Whereas in cubane the C-C-C bond angle is 90°, which gives rise to a high strain energy of approximately 6.5 eV per molecule [138]. The cubane has an

extremely rigid structure at room temperature with exceptional electronic [139], structural and dynamical [140–144] properties compared to other hydrocarbons. The two of it's interesting properties are relatively high melting point of 405 K among this class of materials and very high frequency of the lowest lying intramolecular vibrational mode (617 cm^{-1}) [141,142].

Cubane undergoes a first order phase transition with T_c = 394 K by preserving the rhombohedral structure unlike the usual fcc structure of many orientationally-ordered solids [143]. In association with the transition it undergoes a remarkable volume expansion of 5.4%. The cubane in the orientationally disordered phase rotates about one or more axes, this kind of tumbling motion of the molecule is often referred to as *plastic phase*. This tumbling motion seizes slowly as the temperature is lowered, and the molecule starts to rotate around a fixed axis. The high-temperature rhombohedral phase was identified by XRD [145] with much higher α = 103.3° that persists up to the melting temperature of 405 K. At room temperature, C_8H_8 undergoes explosive decomposition at 3 GPa [146].

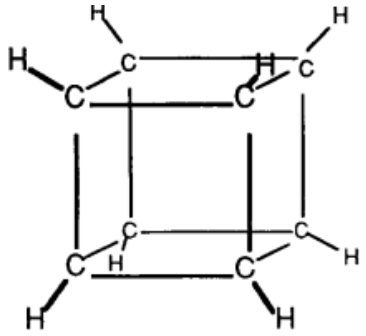

Figure 7.1.: The crystal structure of cubane molecule [141].

7.3. Rotar stator co-crystal C_{60}·C_8H_8

Both C_{60} and cubane were experimentally known for a long time before the first synthesis of fullerene-cubane co-crystals by Pekker *et al.* [147]. The high stability of the 1:1 stoichiometry of C_{60}·C_8H_8 is attributed to the perfect matching of the molecular geometry of the convex interstitial site of fullerene and concave surface of cubane. Cubane molecule occupies the octahedral voids of the fcc C_{60} to form a stable C_{60}·C_8H_8. The co-crystals consist of separate sublattice of rotating fullerene and static cubane of icosahedral and cubic symmetry, respectively. This kind of coexistence of two different sublattices is characteristic of the rotor-stator phases. C_{60}·C_8H_8 forms the highest symmetry member in the family of co-crystals. Table 7.1 lists the lattice parameters of C_{60}·C_8H_8 and its constituent molecules at ambient conditions.

The cubane molecule is held in its well-oriented position due to the retrieving forces of the expanded C_{60} lattice. In order to accommodate the C_8H_8, the C_{60} lattice enlarges with an increase in the nearest-neighbor distance from 10.01 Å to 10.42 Å in

Material	space group	lattice parameter	reference
C_{60}	$Fm\bar{3}m$	a = 14.15 Å	[148]
C_8H_8	$R\bar{3}$	a = 5.34 Å; α = 72.26°; φ = 47.28°	[137]
C_{60}·C_8H_8	$Fm\bar{3}m$	a = 14.74 Å	[147]

Table 7.1.: Lattice parameters of C_{60}, C_8H_8, and C_{60}·C_8H_8 at ambient conditions.

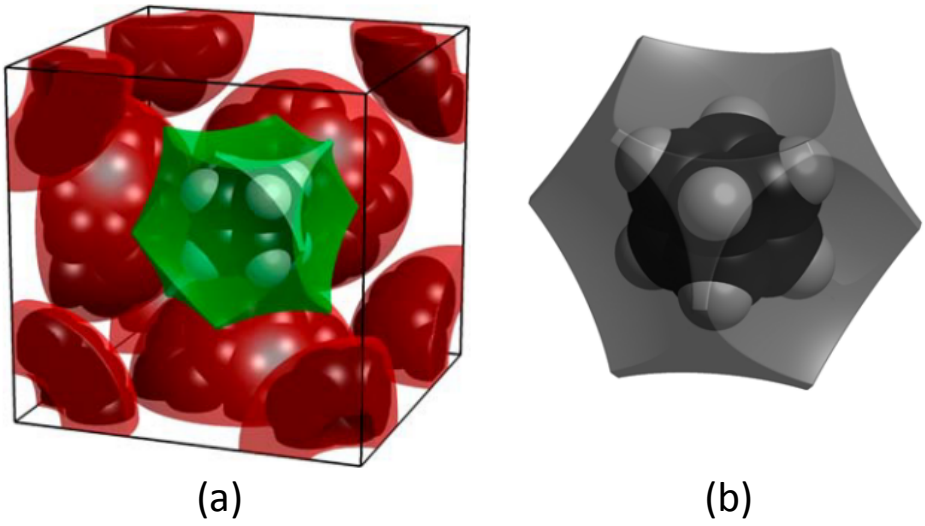

Figure 7.2.: (a) Structure of C_{60}·C_8H_8 unit cell at ambient conditions and (b) concave surface of cubane molecule in the octahedral void formed by rotating fullerene [151].

C_{60}·C_8H_8. The cubic faces of cubane are aligned parallel to that of the unit cell [149]. Fig. 7.2 (a) shows the structure of C_{60}·C_8H_8 and (b) features the outer surface of cubane that allows perfect matching with the octahedral voids of C_{60} molecule. The cubane molecules behave like a molecular bearing by aiding easy rotation of fullerene molecules. Any change in the orientation of the cubane would destroy the match of the complementary molecular surfaces resulting in a decrease of the cohesion energy. As the C_8H_8 is a highly symmetric molecule, it is expected to produce less distortion in the host C_{60} lattice. The ionization potential of the molecular cubane is 8.6 eV [150]. The electron affinity is negative suggesting that it has an energy gap in the ultraviolet range. Since the band edges of C_{60} are inside the ones of cubane, Pekker *et al.* commented that the cubane can be used to mimic negative hydrostatic pressure in fullerite without altering the optical properties of the host [147].

C_{60}	C_8H_8	C_{60}·C_8H_8	Assignment
526		527	$T_{1u}(1)$, F1
577		577	$T_{1u}(2)$, F2
	852	857	T_{1u}, C1
1183		1181	$T_{1u}(3)$, F3
	1235	1224	T_{1u}, C2
1430		1428	$T_{1u}(4)$, F4
	2990	2976	T_{1u}, C3

Table 7.2.: List of the T_{1u} vibrational frequencies in cm^{-1} for C_{60} [48], C_8H_8 [153], and C_{60}·C_8H_8 [154].

7.3.1. Infrared spectrum of C_{60}·C_8H_8

The infrared spectrum of C_{60}·C_8H_8 has seven characteristic vibrational modes, of which four belong to C_{60}. As already mentioned, the neutral C_{60} belongs to I_h symmetry and has 4 T_{1u} IR active modes. Cubane belongs to the octahedral (O_h) point group and has 48 degrees of freedom. By neglecting the the translational and rotational modes of the molecule, it results in 42 internal degrees of freedom. The high symmetry of the cubane molecule contributes to only 18 distinct frequencies and of which only 3 T_{1u} modes are IR active [152]. Table 7.2 lists the vibrational frequencies of the modes of C_{60}, C_8H_8, and C_{60}·C_8H_8. It is clear that the frequency of the modes of C_{60}·C_8H_8 does not have significant shift compared to that of its constituted molecules. This reflects that the co-crystal is held together by a weak Van der Waals interaction [147].

7.4. Orientational ordering in C_{60}·C_8H_8

7.4.1. Solid C_{60}·C_8H_8 at low temperature

On cooling, C_{60}·C_8H_8 undergoes orientational ordering transition at 140 K [147]. At the transition, the symmetry lowers from fcc-to-orthorhombic. Neutral C_{60} is known to undergo a first-order phase transition associated with change in crystal structure from fcc-to-sc with T_c = 249 K [17]. A similar orientational ordering transition in C_{60}·C_8H_8 happens at much lower temperature compared to the C_{60} due to the ball bearing arrangements which facilitates easier rotation of the C_{60} molecule in C_{60}·C_8H_8. By simulated annealing analysis of powder x-ray diffraction data the space group of the ordered orthorhombic phase was identified as *Pnma* [155] recently. From XRD measurements at the phase transition not only a jump in lattice parameter was reported

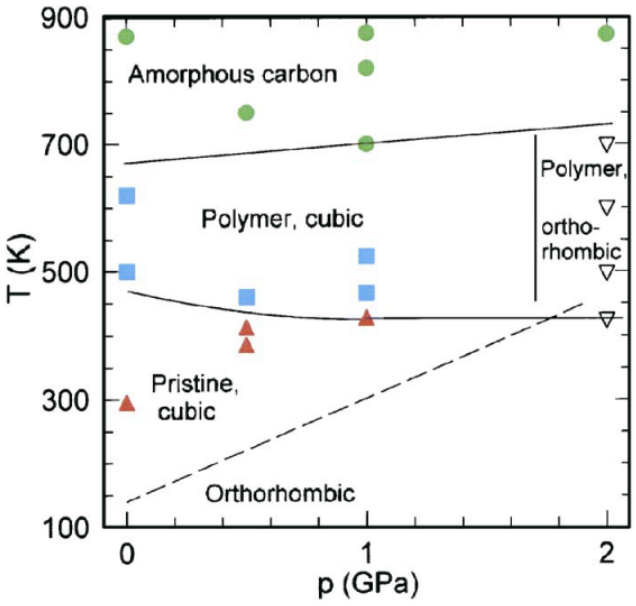

Figure 7.3.: Temperature pressure phase diagram of $C_{60}{\cdot}C_8H_8$ [156].

but also the splitting of reflections indicate symmetry lowering [149]. This would mean that the nearest-neighbor fullerene–cubane interaction plays an important role in the orientational ordering. According to the most recent article by Bortel *et al.* [155], both nearest-neighbor C_{60}-C_{60} and fullerene-cubane interactions influence the ordering transition that coincides with the structural phase transition to the Pnma symmetry. Also it has been stated that the driving force for the crystal symmetry lowering could be the formation of two different short-distance C_{60}-C_{60}. Furthermore, nearest-neighbor fullerene-cubane interaction has also been discussed and these change are much less with decreasing molecular distance.

$C_{60}{\cdot}C_8H_8$ has an interesting temperature-pressure phase diagram with five different structural phases as shown in Fig. 7.3. At room temperature $C_{60}{\cdot}C_8H_8$ has fcc structure and below the orientational ordering temperature it has orthorhombic structure. At elevated temperatures there are two polymeric states with pseudocubic and pseudoorthorhombic structures. At temperatures above 650 K it forms amorphous carbon [156]. Furthermore, the C_{60} – C_{60} distance in $C_{60}{\cdot}C_8H_8$ is uniform (10.42 Å) which splits into five different distances in the ordered phase in the range 10.00 – 11.07 Å [155].

7.4.2. Solid $C_{60}{\cdot}C_8H_8$ under high pressure

Since the main focus of the work is to understand the underlying mechanism of orientational-ordering transition in $C_{60}{\cdot}C_8H_8$. A priori knowledge of the orientational-ordering transition in C_{60} (refer chapter. 2.10) is interesting as both compounds are held together by the Van der waals interactions. C_{60} undergoes orientational-ordering (fcc-to-sc) transition under pressure around 0.8 GPa.

Two pressure-induced anomalies in $C_{60}{\cdot}C_8H_8$ at 0.5 and 1.3 GPa were reported from high-pressure infrared measurements [92]. The first anomaly at 0.5 GPa was interpreted as orientational ordering transition of the fullerene molecules and the second anomaly was correlated to the fullerene–cubane interaction. It has to be noted that these high-pressure infrared studies were carried out with quasi-hydrostatic pressure transmitting medium (KCl). The pressure induced changes were observed as change in slopes of the vibrational modes plotted against increasing pressure. Experimentally it has been shown that the orientational ordering transition is accompanied by structural transition from fcc-to-orthorhombic and also involve changes in the site symmetry of the molecule [149]. Thus splitting of the infrared vibrational modes in the orthorhombic phase is expected which is also acknowledged by the authors of reference [92]. While on the contrary, splitting was not observed in the vibrational modes due to considerable broadening at higher pressures with the use of KCl as pressure transmitting medium. The magnitude of broadening of the modes is larger than the magnitude of the splitting. In addition, the quasi-hydrostatic pressure transmitting medium can cause strain effects on the samples. Since the vibrational modes are highly sensitive to external environment, it is ideal to investigate $C_{60}{\cdot}C_8H_8$ with better hydrostatic conditions.

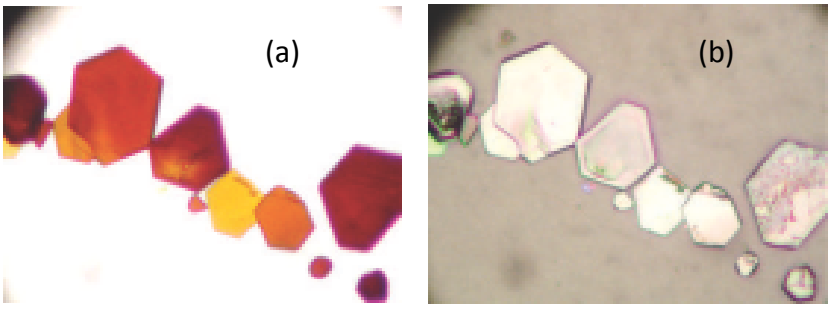

Figure 7.4.: (a) Transmission and (b) reflection of $C_{60}{\cdot}C_8H_8$ single crystals over quartz plate under optical microscope [147]

7.5. Results and discussion

In an effort to explore the vibrational properties of $C_{60}{\cdot}C_8H_8$ under hydrostatic pressure, argon and helium were chosen as the pressure transmitting medium for this work. Optical microscopy photos of the $C_{60}{\cdot}C_8H_8$ crystals are shown in Fig. 7.4.

7.5.1. High-pressure infrared measurements on $C_{60}{\cdot}C_8H_8$

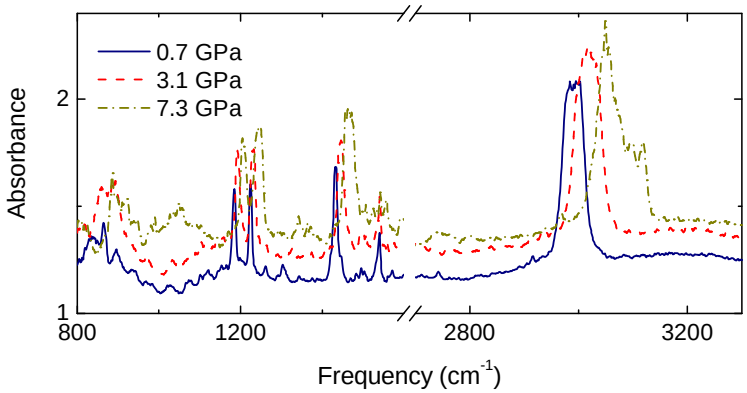

Figure 7.5.: High-pressure mid-infrared spectrum of $C_{60}{\cdot}C_8H_8$ measured with argon as pressure transmitting medium.

The high pressure was generated using Syassen-Holzapfel DAC with helium as the hydrostatic pressure transmitting medium and Cryo DAC mega was used with argon as the pressure medium. Loading DAC with fluid helium or argon as pressure transmitting media was introduced in chapter. 3.3.3.2. Pressures up to 8 GPa were reached with argon and even up to 16 GPa with helium. Infrared transmission measurements were carried out in the mid-infrared frequency range with Bruker IFS 66 V/s coupled to an infrared microscope with a resolution of 2 cm^{-1}. All measurements were performed at room temperature.

The work was started with argon as pressure medium since loading the DAC with argon is relatively easier than with helium. $C_{60}{\cdot}C_8H_8$ was measured with argon as pressure transmitting medium in the mid infrared range and the spectrum for selected pressures are presented in Fig. 7.5. The shift in the vibrational modes had similar trend like that with the solid medium due to limitations of the hydrostaticity of argon. As argon solidifies at 1.3 GPa, and this process can move the sample and making the reference measurements difficult. Also the transmission level before and after solidification are not the same. In order to over come these shortcomings the high pressure

measurements were resorted to the use of helium as pressure medium. Therefore liquid helium which is one of the best pressure transmitting media was used in spite of the complications involved in loading the DAC.

Helium provides good hydrostatic conditions even when it solidifies. A typical filling of the DAC with helium is shown in Fig. 7.6. As already mentioned, the $C_{60}{\cdot}C_8H_8$ has seven vibrational modes in the infrared region of which six modes are clearly detected in the presented mid-infrared data. These modes for selected pressure can be seen in the Fig. 7.7. The C3 mode has very high absorbance and the vibrational mode saturates so the analysis of this mode was not performed. Fig. 7.8 shows a closer view of the vibrational modes of fullerene (F) and cubane (C) for selected pressures with helium as pressure medium. In these data, it can be clearly seen that even up to the highest measured pressure the vibrational modes remain very sharp. In contrast to this, with KCl as pressure transmitting medium the vibrational modes undergo significant broadening with increasing pressure [92].

Figure 7.6.: Photos of DAC under the microscope filled with sample (S), Ruby balls (R) and helium (the bright area).

The vibrational modes are fitted with Lorentz oscillators to extract the frequency with increasing pressure. The plot in Fig. 7.9 shows the pressure dependence of the vibrational modes. In general, all vibrational modes harden with increasing pressure. Among the fullerene modes, the most sensitive F4 mode shows a two-fold splitting around 1 GPa. At 3 GPa, F3 and F4 modes show threefold splitting. Also the two observed cubane modes show a threefold splitting at 3 GPa. It is interesting to note that the vibrational mode F2 remains as a singlet up to high pressure.

The splitting of the cubane and fullerene modes at 3 GPa are interpreted as the orientational ordering transition of the fullerene molecules. This transition is accompanied by fcc-to-orthorhombic transition of the crystal and this would indeed cause a molecular symmetry change. The threefold splitting of the T_{1u} modes of fullerene can be contemplated as sign for possible transformation of C_{60} molecule to a lower symmetry such as D_{2h}. The orthorhombic phase with *Pnma* space group can be attributed to have a molecular site symmetry of D_{2h}. The driving force for orientational ordering transition in $C_{60}{\cdot}C_8H_8$ is suggested to be due to both nearest-neighbor fullerene-cubane and C_{60}-C_{60} interactions. Whereas the observed critical transition

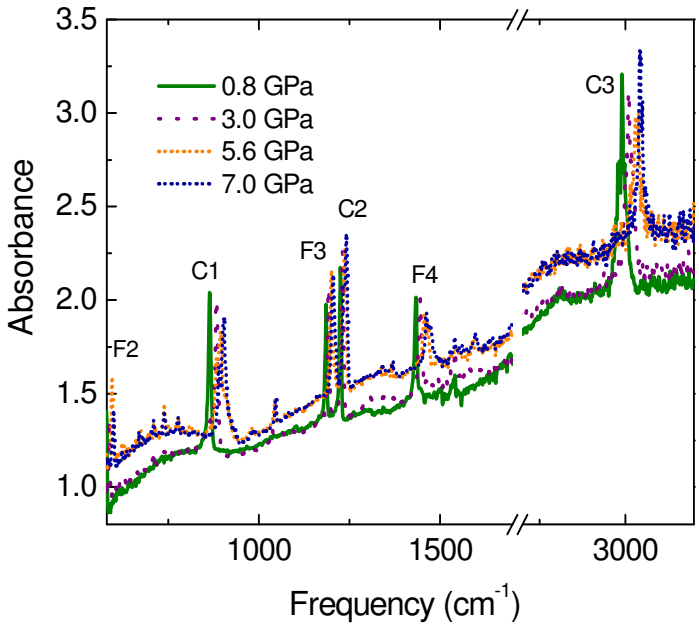

Figure 7.7.: Mid-infrared absorbance spectrum showing the $C_{60}{\cdot}C_8H_8$ vibrational modes for selected pressures.

pressure value of 3 GPa from this data is much higher than the reported 0.5 GPa in the earlier work [92]. Now with the knowledge from the current work, the previous work [92] can be rethought and the reported 1.3 GPa transition which was originally attributed to the fullerene-cubane interaction must be the orientational ordering transition. As the broadening of the vibration mode hampered the observation of the mode splitting, it was misinterpreted that the orientational ordering occurs at 0.5 GPa.

The application of pressure and lowering of temperature are analogous to each other in many fullerene-based compounds. Thus, the temperature dependence of $C_{60}{\cdot}C_8H_8$ is reviewed, the orientational ordering temperature is lowered by 100 K in case of $C_{60}{\cdot}C_8H_8$ compared to that of the pristine C_{60}. Therefore, naively the orientational ordering transition pressure can be expected at a higher in case of $C_{60}{\cdot}C_8H_8$ than C_{60}. Additionally, by the use of helium as the pressure transmitting medium, which can diffuse into the voids of the $C_{60}{\cdot}C_8H_8$ lattice can have an effect on the transition pressure. Prior to understanding the observed high critical pressure, a brief review about the properties of helium as pressure transmitting media is presented. Helium ensures very good hydrostatic conditions in the DAC which would reduce the strain effects on the sample and brings out a more reasonable transition pressure in comparison to the use

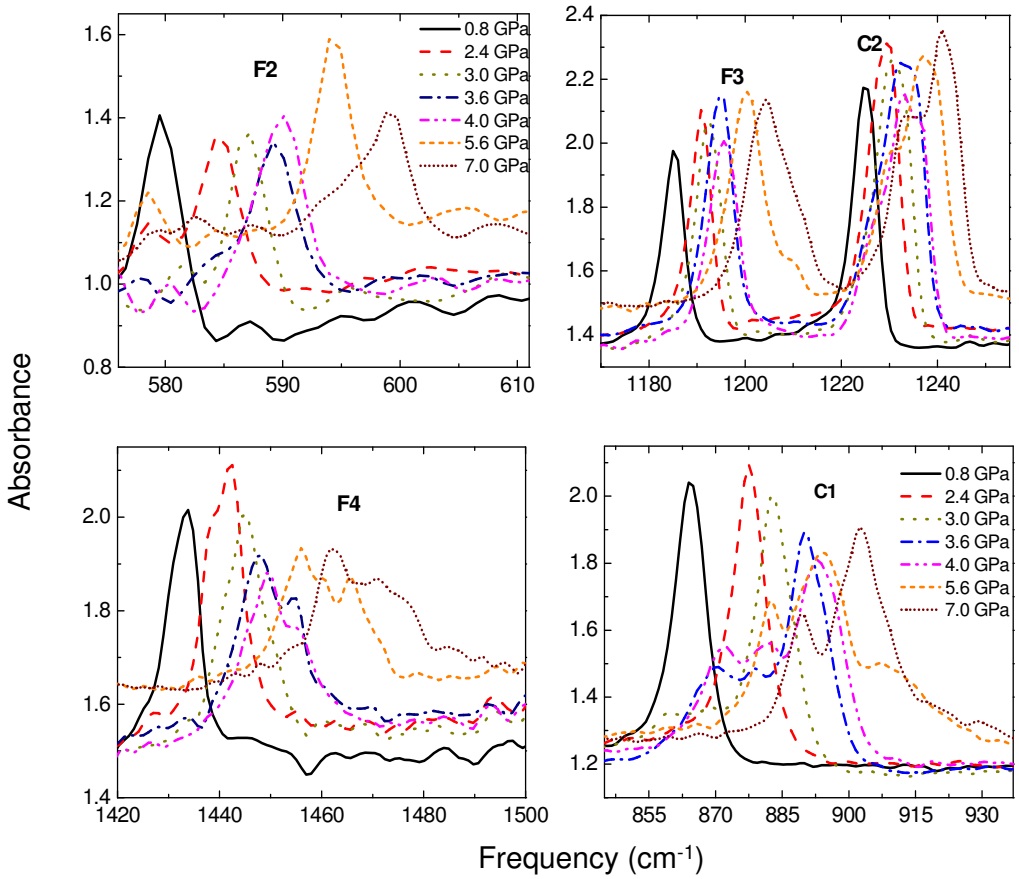

Figure 7.8.: Infrared absorption modes of $C_{60}{\cdot}C_8H_8$ for selected pressures.

of solid medium. The solid medium causes local strain causing higher pressure locally, this results in wrong estimation of the critical pressure. In case of fullerene based compounds, the voids are large enough for some diffusion of the helium in to the lattice. Hence, it is good to follow up the behavior of the parent compound, namely C_{60} under hydrostatic conditions. Experiments on C_{60} with hydrostatic pressure transmitting medium such as helium, nitrogen, argon, etc were performed [157, 158]. In fcc C_{60}, each C_{60} molecule in the lattice has two tetrahedral and one octahedral voids with average diameters of 2.2 Å and 4.2 Å, respectively [159]. Any impurities in the voids can considerably affect the properties such as the orientational ordering transition temperature or pressure, compressibility, thermal expansion coefficient, etc [158]. Sundqvist summarizes the results of the orientational ordering transition boundary from various experiments, with the solid pressure transmitting medium it occurs at 0.5 GPa against a slightly higher value of 0.8 GPa for helium as pressure medium [90]. With the use of alcohol mixture (4:1 methanol-ethanol) as pressure transmitting medium, which has

good hydrostatic conditions the transition pressure was reported to be 0.4 GPa [160]. Furthermore experiments have clearly suggested that helium can penetrate the fcc C_{60} lattice and influence the orientational motion of the molecules. Helium with an atomic radius of 0.93 Å [161,162] can penetrate both the octahedral and tetrahedral voids but probably cannot penetrate the C_{60} molecule itself. At first helium penetrates the octahedral voids rapidly and then followed by the tetrahedral voids [158]. With the helium inside the lattice, it can render the lattice less compressible than in its absence. In case of C_{60} the helium present in the lattice can increase the orientational phase transition by 10 K and the change in lattice parameter at the transition is halved [158]. Moreover the intercalation is much more rapid with increasing pressure [158]. The pressure dependence of the orientational ordering is influenced by the presence of the interstitial species in the lattice of pure C_{60}. Therefore, it is clear that the pressure transmitting medium and its hydrostaticity can play a key role in high pressure experiment on C_{60}-based compounds. By apply the same idea for $C_{60}{\cdot}C_8H_8$ in which the octahedral void of the fcc C_{60} is occupied by the C_8H_8 the tetrahedral voids are free for hosting the helium. Experiments on C_{60} suggest that the diffusion can also be a function of time *i.e.*, the longer the sample is exposed to the helium the more intercalation takes place. During the initial time of 25 – 30 hours the intercalation takes place more rapidly which is evident from the rapid increase of the lattice parameter of pristine C_{60} [158]. Typically the helium filling of the DAC for the presented data was done with the bath cryostat. The minimum time required for such filling was about 8 hours until the setup warms up to room temperature to retrieve the DAC for high pressure measurements. Thus the $C_{60}{\cdot}C_8H_8$ samples were exposed to helium for least 8 hours before the high-pressure infrared measurements, which is considerable time for some helium to diffuse into the $C_{60}{\cdot}C_8H_8$ lattice. Therefore the intercalation of helium in at least some of the tetragonal voids of $C_{60}{\cdot}C_8H_8$ is highly probable.

Nevertheless the influence of the intercalated helium on the transition pressure will be weak and would only shift the pressure to a slightly higher value similar to the case of C_{60}. In case of pristine C_{60} the critical pressure changes by the presence of the helium in the octahedral and tetrahedral void only by 0.3 GPa higher in contrast to solid medium. Not only in fullerene-based compounds but also in nanotubes an ideal critical pressure was reported with helium as pressure medium which is slightly high in value compared to solid medium [163]. Moreover the helium would only intercalate into the tetrahedral voids in case of $C_{60}{\cdot}C_8H_8$. So influence of the intercalated helium on the critical pressure would not be very large.

Further evidence that supports the orientational ordering transition at 3 GPa is the activation of silent modes due the symmetry reduction. Fig. 7.10 (a) shows the

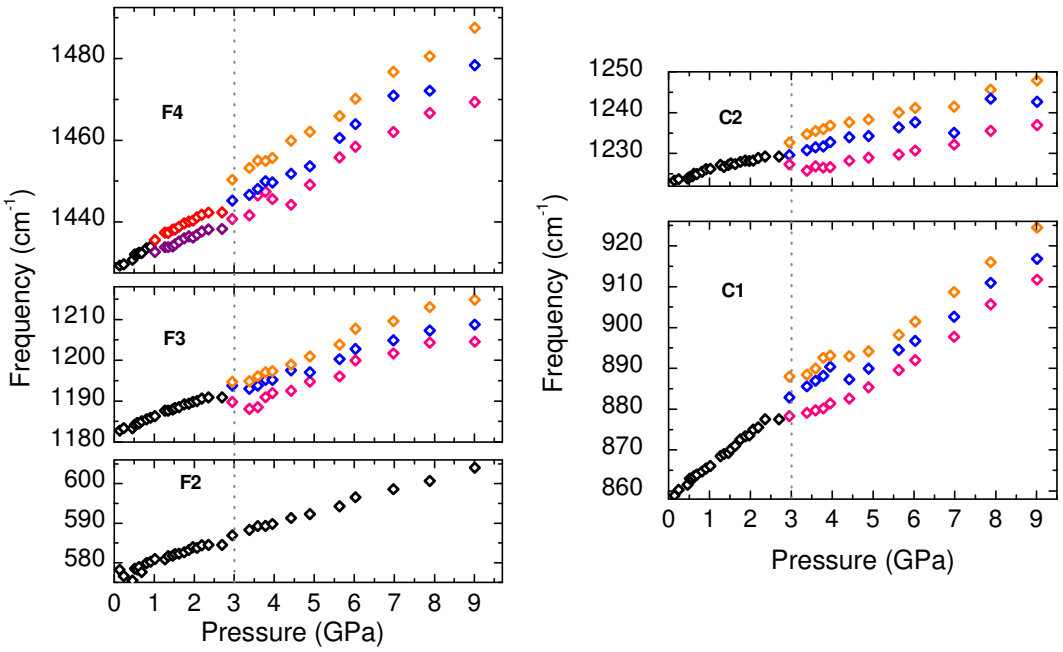

Figure 7.9.: Frequency position of the vibrational modes of fullerene and cubane with increasing pressure.

activated silent mode at 3 GPa and at 8 GPa close to C1 mode. The silent modes harden with increasing pressure as seen in 7.10 (b). Few other silent modes activated under pressure are also observed in the region 700–800 cm^{-1} (see Fig. 7.11). This serves as additional evidence that the symmetry lowers at 3 GPa in connection with the disorder-order transition in $C_{60}{\cdot}C_8H_8$.

Both $C_{60}{\cdot}C_8H_8$ and C_{60} are held together by weak Van der Waals interactions nevertheless they show different critical pressure for the orientational ordering transitions. The higher P_c in $C_{60}{\cdot}C_8H_8$ in comparison to C_{60} could be attributed to larger lattice of $C_{60}{\cdot}C_8H_8$ and underlying driving mechanism of the transition (*i.e.* only nearest-neighbor C_{60}-C_{60} interactions in case of C_{60} where as both nearest-neighbor C_{60}-C_{60} and C_{60}-cubane play a role in $C_{60}{\cdot}C_8H_8$). Thus, in the presented data on $C_{60}{\cdot}C_8H_8$ with helium as pressure medium the orientational ordering transition pressure observed is reasonable. With the above agrement it can be summarized at 3 GPa, the $C_{60}{\cdot}C_8H_8$ undergoes orientational ordering transition which is accompanied by the fcc-to-orthorhombic structural transition.

This new result on $C_{60}{\cdot}C_8H_8$ sheds light on the pressure-temperature phase diagram of $C_{60}{\cdot}C_8H_8$ which originally has a orientational ordering transition line based on the

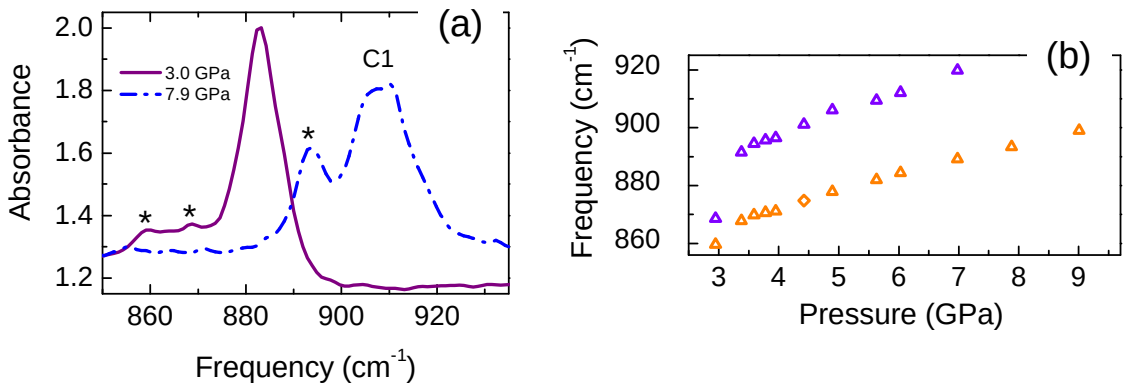

Figure 7.10.: (a) Silent modes (marked with ∗) that are close to C1 vibrational modes for selected pressures and (b) pressure dependence of these silent modes.

pressure coefficient of the pure C_{60}. [156]. From this P-T diagram the orientational ordering transition occurs at 1 GPa. According to the present understanding on the orientational ordering mechanism in C_{60}·C_8H_8, it is not only driven by the nearest-neighbor C_{60}-C_{60} interaction but also by the nearest-neighbor fullerene-cubane interaction plays a significant role. This has to be taken into account and the orientational ordering transition in the P-T diagram of C_{60}·C_8H_8 should be altered, which would result in a high P_c at 300 K than that indicated by Iwasiewicz-Wabnig *et al.* [156].

In addition to the 3 GPa orientational ordering transition, the F4 mode shows splitting already at 1 GPa into a doublet and this has be explained in terms of the appearance of the silent modes under pressure. Kamarás *et al.* [48] have discussed the appears of forbidden vibrational modes in the solid state C_{60}. The presence of crystal field in the fcc crystal reduced the point group I_h of the C_{60} molecule to T_h site symmetry. This causes the activation of some silent odd-parity modes. At ambient conditions, these effects are weak and are not observed in the infrared spectrum due to the dynamical orientational disorder, whereas with lowering temperature several modes appear in the spectrum. Similarly, with increasing pressure of the vibrational modes can appear such as the one observed very close to F4 mode at 1 GPa, which is weak and is seen more as a shoulder to the F4 mode. This mode can be attributed to the G_u mode and should not be confused as splitting of the F4 mode itself. This mode is very weak and could not be followed well when the F4 mode undergoes a threefold splitting at 3 GPa. Similarly, at 710 cm^{-1} the weak H_u mode appears already at 0.8 GPa, which can be seen in Fig. 7.11. Finally, the robustness of the F2 mode has already been discussed in literature from temperature-dependent measurements. Thus

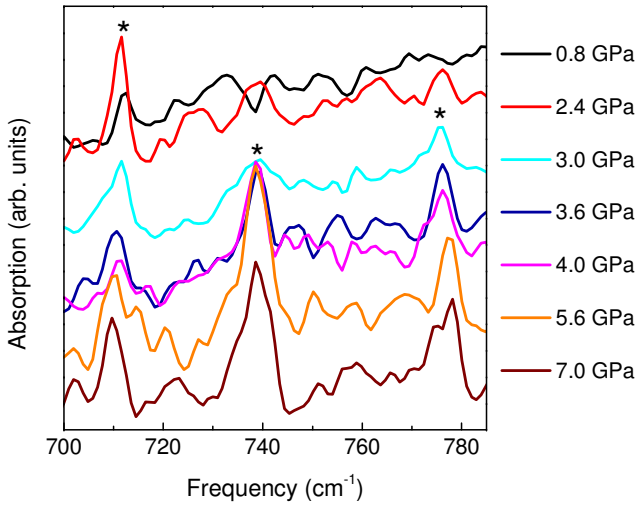

Figure 7.11.: Activation of the silent modes (marked with $*$) under pressure.

it is not surprising that the F2 mode does not undergo any splitting under pressure.

7.6. Summary

A successful investigation of $C_{60}{\cdot}C_8H_8$ under very good hydrostatic condition was done. In summary, the orientational ordering transition was observed at 3 GPa from the threefold splitting of the fullerene and cubane vibrational modes. The driving force of the transition is attributed to both the nearest neighbored C_{60}-C_{60} and fullerene-cubane interactions. The threefold splitting of fullerene and cubane mode can be attributed to D_{2h} molecular site symmetry, which is consistent with *Pnma* space group of orthorhombic ordered phase of $C_{60}{\cdot}C_8H_8$. Furthermore, the activation of silent modes is also observed above 3 GPa which confirms the critical pressure of the orientational ordering transition. Also some weak modes are activated in the infrared spectrum at lower pressure ($\sim$ 1 GPa) due to the crystal field effects. With this result, additional evidence are brought forth that the driving force of the orientational ordering transition is influence by both nearest neighbor fullerene-cubane and C_{60}-C_{60} interactions. Thus, the orientational ordering transition marked on the pressure-temperature phase diagram by Iwasiewicz-Wabnig *et al.* has to be revised by taking into account these results.

8. Conclusions

As a part of this project, the pressure-dependent infrared measurements on the Jahn-Teller active fullerene-based compounds namely $(Ph_4P)_2IC_{60}$ and A_4C_{60} were performed over a broad frequency range. The vibrational and electronic properties of both $(Ph_4P)_2IC_{60}$ and A_4C_{60} were investigated. The dynamic-to-static JT transition was investigated on C_{60}^- in $(Ph_4P)_2IC_{60}$ and an insulator-to-metal transition was probed in A_4C_{60}. In addition, the rotar stator co-crystal $C_{60}{\cdot}C_8H_8$ were investigated under hydrostatic pressure to determine the critical pressure of orientational ordering transition and the driving mechanism from their vibrational properties.

The pressure dependence of the vibrational and electronic/vibrobic excitations of C_{60}^- anion in $(Ph_4P)_2IC_{60}$ were investigated up to 9 GPa for the first time. All the four fundamental T_{1u} modes shows a doublet splitting at the lowest measured pressure, which reflects the dynamic nature of the Jahn-Teller distortion. The C_{60}^- undergoes a pressure induced static-to-dynamic transition at around 2 GPa caused by steric crowding of the lattice. This is reflected by the splitting of several fullerene and the cation modes of $(Ph_4P)_2IC_{60}$ and by pressure-dependent anomalies of the vibrational modes. The electronic spectrum of $(Ph_4P)_2IC_{60}$ has four bands that correspond to the excitations between the split LUMO levels (t_{1u} and t_{1g}) due to the presence of the Jahn-Teller distortion and the vibronic excitations. The observed bands in the NIR-VIS region can be interpreted as one optically allowed transition from $a_{2u}{\rightarrow}e_{1g}$ and three higher lying vibronic transitions. These transitions in the NIR-visible region soften under pressure indicating that the splitting of the LUMO and LUMO+1 electronic states are reduced under pressure. It has been inferred from the vibrational and electronic transitions that the C_{60}^- would posses either D_{5d} or D_{3d} symmetry at lowest measured pressure.

Infrared high-pressure measurements on A_4C_{60} (A = K and Rb) over a broad frequency range upto 8 GPa were performed. The FIR spectra of Rb_4C_{60} has a finite spectral weight in the low frequency (Drude term) region indicating a bad metal behavior under pressure. There is a monotonic increase in the spectral weight of the Rb_4C_{60} at low frequency with increasing pressure. The low frequency region of the MIR absorbance spectra of K_4C_{60} under pressure shows very less changes. The MIR

absorbance band due to the interband transition within the t_{1u} orbital is clearly observed in case of K_4C_{60} spectrum and with increasing pressure it shows a weak softening behavior. In case of the Rb_4C_{60} reflectance spectra, the t_{1u} interband excitations are weak and are hard to follow due to the diamond absorbance of the DAC. The NIR-visible absorbance spectra of both Rb_4C_{60} and K_4C_{60} show the LUMO→LUMO+1 transitions. These transitions indicate that both compounds assume a static JT distortion at the lowest measured pressure. The transitions soften with increasing the pressure indicating a decrease in the splitting of the orbitals at the molecular level. Thus, it can be concluded that the Rb_4C_{60} shows a bad metal behavior with increasing pressure and the tentative argument on driving mechanism of the transition is due to the change in W which makes the electron correlations to cause a metallic state and also the JT distortion is stabilized under pressure. Another possible explanation for the metallic behavior in literature is the phase separation of the Rb_4C_{60} into Rb_3C_{60} and Rb_6C_{60}, where Rb_3C_{60} is a metallic phase. From the infrared high-pressure measurements, only $T_{1u}(2)$ and $T_{1u}(4)$ phonons are observed until the highest measured pressure, this suggests that there is no appearance of Rb_6C_{60} phase under pressure which in turn eliminates the appearance of Rb_3C_{60} within the lateral resolution of the infrared measurement scale. The Rb_4C_{60} phonons were better described by the Fano line shape. The pressure dependence of Fano parameter suggest that the phonon are coupled to the electronic background lying at lower energy than the phonon itself. Furthermore, the frequency of the Rb_4C_{60} phonon shows a monotonic hardening with increasing the pressure. The phonon of K_4C_{60} shows a weak anomaly at around 0.8 GPa, which might be interpreted as the dynamic-to-static Jahn-Teller transition. From the NIR-Visible excitation, it is observed that the K_4C_{60} assumes a static distortion at the lowest pressure (0.5 GPa). Therefore, an upper bound for the dynamic-to-static transition for K_4C_{60} can be assigned at 0.8 GPa.

The $C_{60}{\cdot}C_8H_8$ were investigated under hydrostatic pressure with helium as pressure transmitting medium. The orientational ordering transition was observed at 3 GPa which is accompanied by the fcc-to-orthorhombic transition. The threefold splitting of the fullerene and cubane vibrational modes at 3 GPa confirms the recent finding of the Pnma space group of the ordered orthorhombic phase. The driving force of the orientational ordering transition in $C_{60}{\cdot}C_8H_8$ is influenced by both the nearest-neighbor fullerene-cubane and C_{60}-C_{60} interactions. Thus, the predicted orientational ordering transition in the pressure-temperature phase diagram must be altered by taking these findings into account. Moreover the earlier high-pressure infrared data on $C_{60}{\cdot}C_8H_8$ can be better understood with knowledge gained from the presented results and the orientational ordering transition in earlier results [92] has to be attributed to

the anomaly at 1.3 GPa with use of solid pressure transmitting medium. With the use of helium as pressure transmitting medium, activation of the silent mode occurs around 1 GPa which is due to the effect of crystal field environment under pressure.

A. XRD on alkali fullerides

The X-ray diffraction spectra of most of the synthesized samples are presented here. In order to identify the phase(s), in addition to the spectra the calculated peak position of the possible phases are marked below each XRD spectra. Each figure has a brief description about the phases identified.

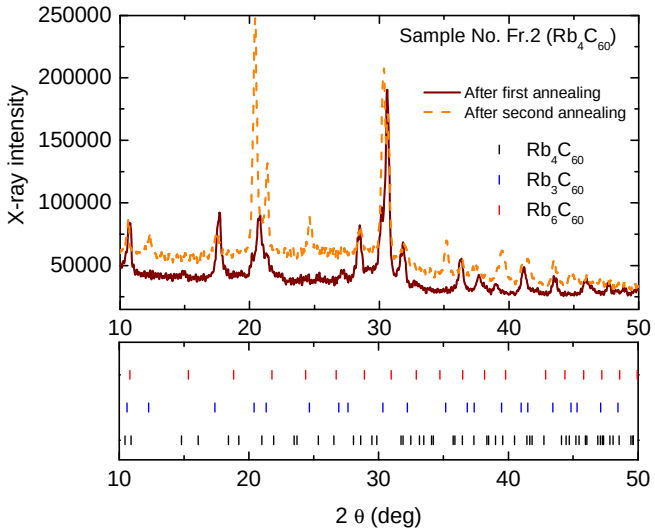

Figure A.1.: The XRD spectrum of Fr.2 sample, which has a majority of Rb_3C_{60} phase after the completion of the first heat treatment cycle. In order to improve the quality of the sample, weighed quantity of Rb was added to the sample and further heat treatment was done. Nevertheless the sample did not reach the required phase after the second heat treatment.

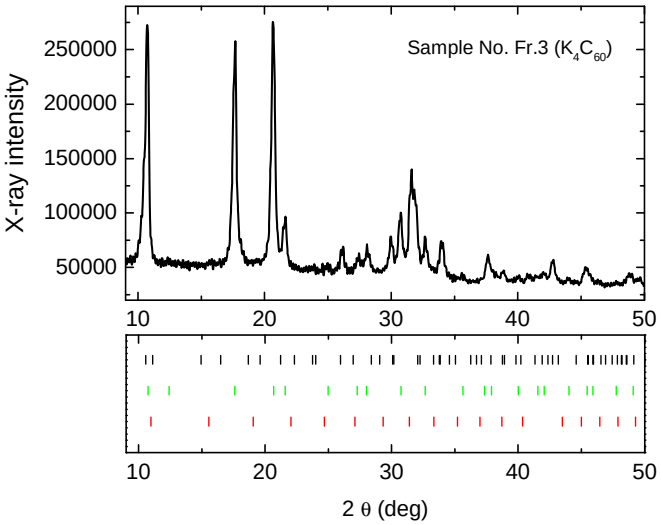

Figure A.2.: The XRD spectrum of Fr.3 sample, which is a complete mixture of K_3C_{60} and K_4C_{60}. The ratio of K_3C_{60} phase accounts to more than 60 %.

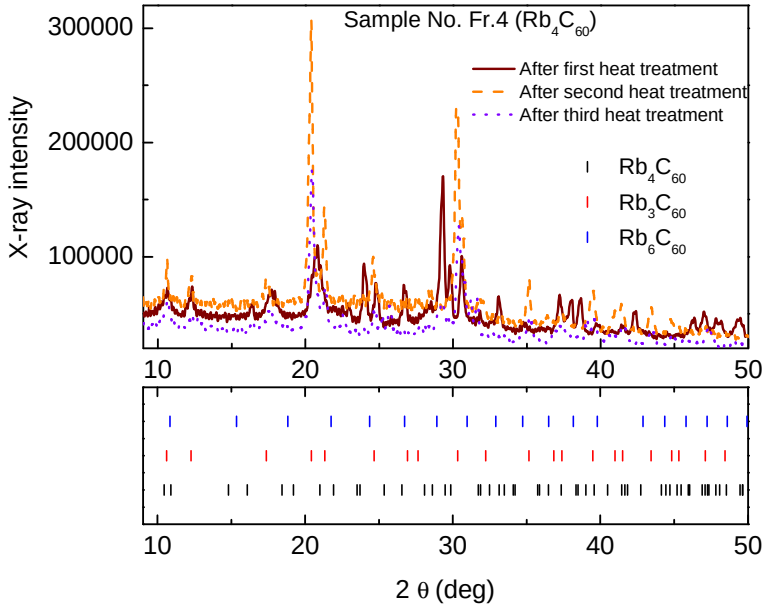

Figure A.3.: The XRD spectra of Fr.4 sample that was annealed several times to eliminate the undesired phases. By addition either C_{60} or Rb to correct the stoichiometry of the sample but the sought after was not attained.

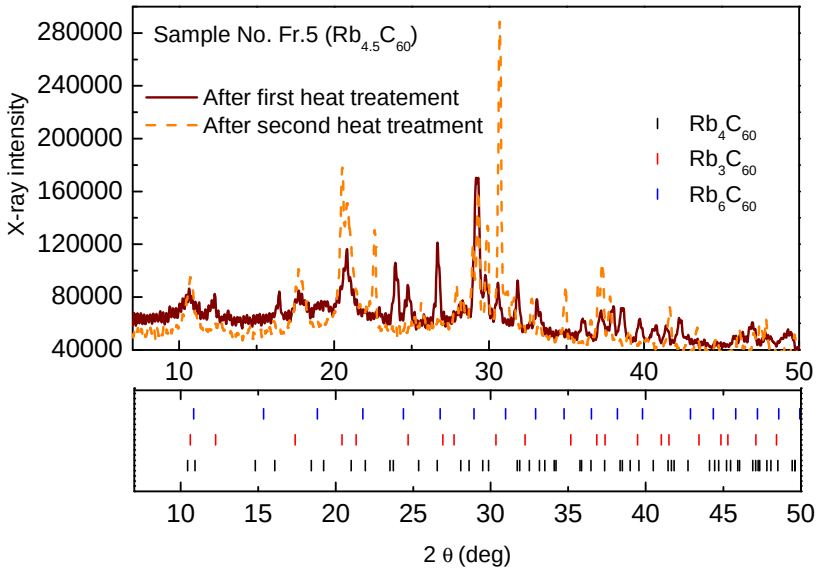

Figure A.4.: The XRD spectrum of Fr.5 sample after the first heat treatment cycle was a mixture of Rb_3C_{60} and Rb_6C_{60} with a majority of Rb_3C_{60} phase. This means the reaction was not complete so the sample was further annealed and the resulting sample was mixture of all the three phases.

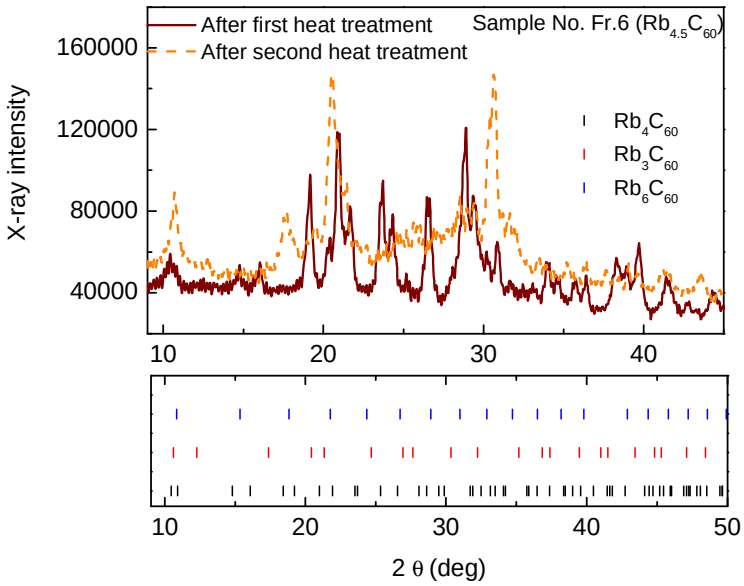

Figure A.5.: The XRD spectrum after first heat treatment of Fr.6 sample was a mixture of all three phases but with a majority of Rb_4C_{60} phase. Thus the second heat treatment was done and the resultant sample was again a phase mixture.

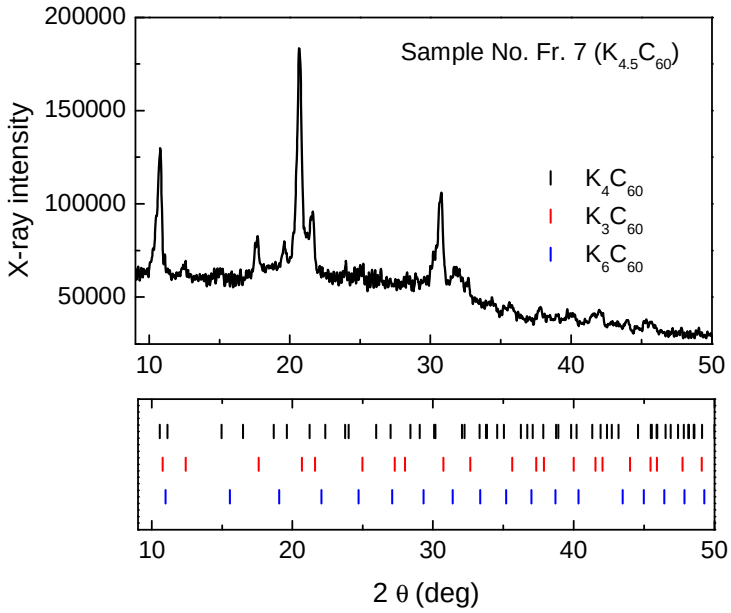

Figure A.6.: The XRD spectrum of Fr.7 showed a majority of K_4C_{60} and a minority phase of K_3C_{60}. The sample was heat treated again but it resulted in a phase mixture with majority of K_3C_{60}.

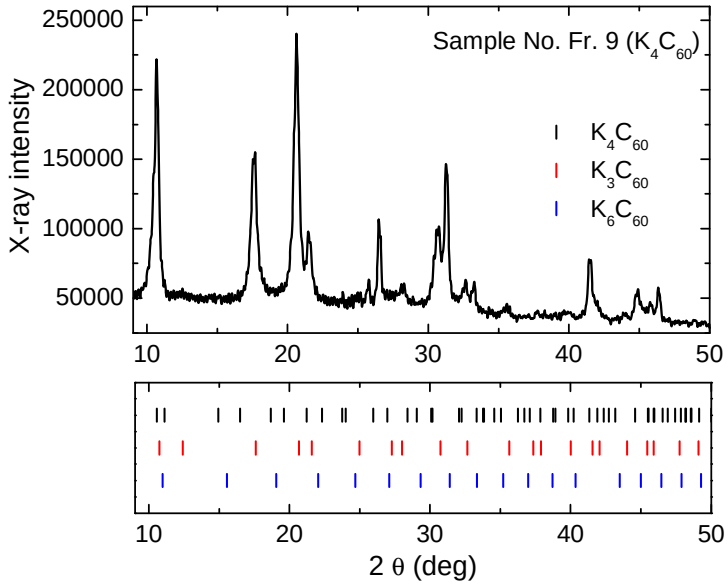

Figure A.7.: The XRD spectrum of Fr9 sample with nearly 80 % of the K_3C_{60} phase. In order to obtain the require phase a calculated amount of K was added and the second heat treatment was carried out but unfortunately the sample was destroyed while sealing under vacuum.

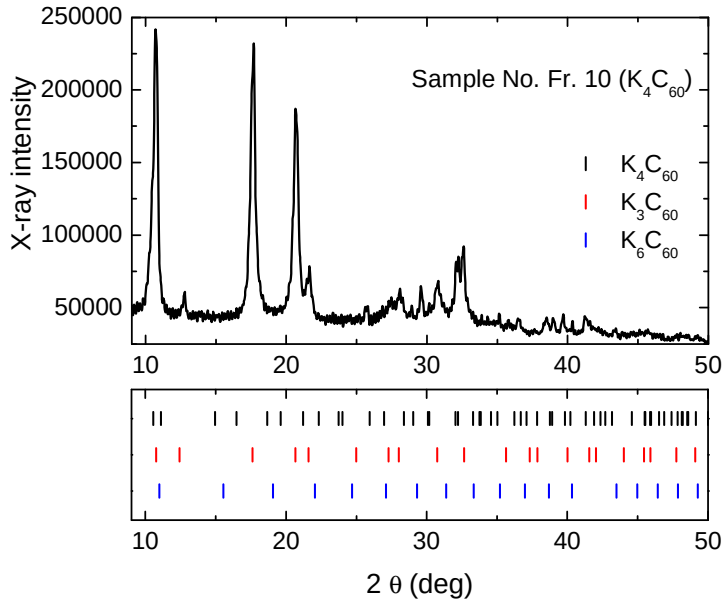

Figure A.8.: The XRD spectrum of Fr.10 sample. It was nearly phase pure K_3C_{60} with minority of other phases.

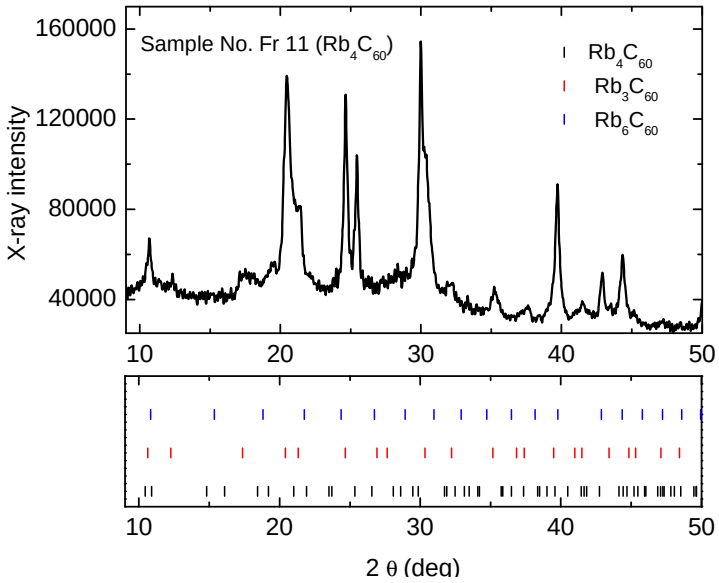

Figure A.9.: The XRD spectrum of Fr.11 sample contain a combination of all three phases.

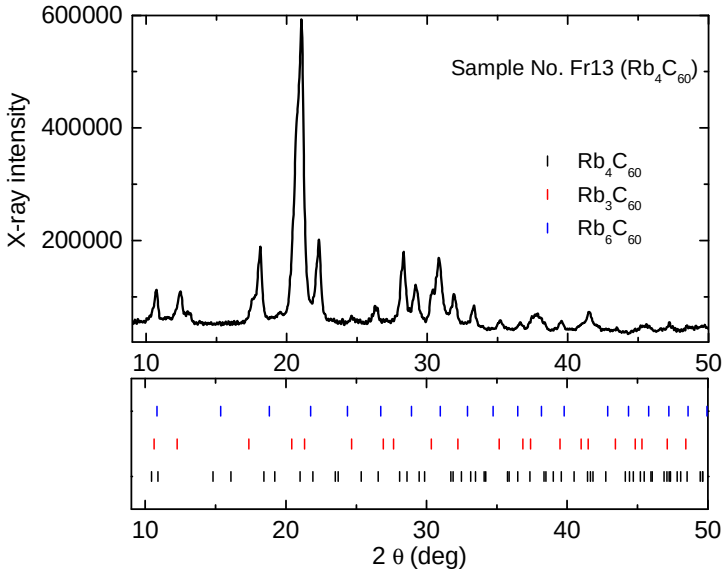

Figure A.10.: The XRD spectrum of Fr.13 was a admixture of different phases.

Bibliography

[1] V. C. Long, J. L. Musfeldt, K. Kamarás, A. Schilder, and W. Schütz, Phys. Rev. B **58**, 14338 (1998).

[2] V. Long, J. Musfeldt, K. Kamarás, A. Schilder, and W. Schütz, Synt. Met. **103**, 2435 (1999).

[3] V. C. Long, J. Musfeldt, K. Kamarás, E. C. Schundler, G. B. Adams, J. B. Page, W. Bietsch, and I. Bauer, Phys. Rev. B **75**, 125402 (2007).

[4] W. Bietsch, J. Bao, J. L*ü*decke, and S. van Smaalen, Chem. Phys. Lett. **324**, 37 (2000).

[5] G. Völkel, A. Pöppl, J. Simon, J. Hoentsch, S. Orlinskii, H. Klos, and B. Gotschy, Phys. Rev. B **52**, 10188 (1995).

[6] H. W. Kroto, J. R. Heath, S. C. O'Brien, R. F. Curl, and R. E. Smalley, Nature **318**, 162 (1985).

[7] S. Iijima, Nature **354**, 56 (1991).

[8] K. S. Novoselov, A. K. Geim, S. V. Morozov, D. Jiang, Y. Zhang, S. V. Dubonos, I. V. Grigorieva, and A. A. Firsov, Science **306**, 666 (2004).

[9] H. Yang, B. Q. Mercado, H. Jin, Z. Wang, A. Jiang, Z. Liu, C. M. Beavers, M. M. Olmstead, and A. L. Balch, Chem. commun. (Camb). **47**, 2068 (2011).

[10] P. R. Buseck, S. J. Tsipursky, and R. Hettich, Science **257**, 215 (1992).

[11] L. Becker, J. Bada, R. Winans, J. Hunt, T. Bunch, and B. French, Science **265**, 642 (1994).

[12] P. R. Buseck, Earth Planet. Sci. Lett. **203**, 781 (2002).

[13] W. Krätschmer, L. Lamb, K. Fostiropoulos, and D. Huffman, Nature **347**, 354 (1990).

[14] R. D. Johnson, D. S. Bethune, and C. S. Yannoni, Acc. Chem. Res. **25**, 169 (1992).

[15] M. Yoshida, M. Fujita, and Ōsawa Eiji, Synt. Met. **70**, 1487 (1995).

[16] C. H. Pennington and V. A. Stenger, Rev. Mod. Phys. **68**, 855 (1996).

[17] P. A. Heiney, J. E. Fischer, A. R. McGhie, W. J. Romanow, A. M. Denenstein, J. P. McCauley Jr., A. B. Smith, and D. E. Cox, Phys. Rev. Lett. **66**, 2911 (1991).

[18] F. Rioux, J. Chem. Educ. **80**, 1380 (2003).

[19] R. Carter, *Molecular symmetry and Group Theory* (John Wiley and Sons, New York, 1998).

[20] R. Haddon, L. Brus, and K. Raghavachari, Chem. Phys. Lett. **125**, 459 (1986).

[21] R. C. Haddon, Acc. Chem. Res. **25**, 127 (1992).

[22] T. Rabenau, A. Simon, R. K. Kremer, and E. Sohmen, Z. Phys. B - Condensed Matter **90**, 69 (1993).

[23] N. Troullier and J. L. Martins, Phys. Rev. B **46**, 1754 (1992).

[24] Y. M. A. Oshiyama, S. Saitot and N. Hamada, J. Phys. Chem. Solids **53**, 1689 (1992).

[25] J. L. Martins, N. Troullier, and J. H. Weaver, Chem. Phys. Lett. **180**, 457 (1991).

[26] S. Saito and A. Oshiyama, Phys. Rev. Lett. **66**, 2637 (1991).

[27] I. László and L. Udvardi, Chem. Phys. Lett. **136**, 418 (1987).

[28] H. A. Jahn and E. Teller, Proc. R. Soc. Lond. A, Math. Phys. Sci. **161**, 220 (1937).

[29] J. N. O'Shea, Science **310**, 453 (2005).

[30] M. C. M. O'Brien, Phys. Rev. B **53**, 3775 (1996).

[31] G. Klupp and K. Kamarás, in *The Jahn-Teller Effect*, Vol. **97** of *Springer Series in Chemical Physics*, edited by H. Köppel, D. R. Yarkony, and H. Barentzen (Springer, Berlin Heidelberg, 2009), pp. 489–515.

[32] C. C. Chancey and M. O'Brien, *The Jahn-Teller Effect in C_{60} and Other Icosahedral Complexes* (Princeton Univeristy Press, Princeton, New Jersey, 1997).

[33] G. Klupp, K. Kamarás, N. M. Nemes, C. M. Brown, and J. Leão, Phys. Rev. B **73**, 085415 (2006).

[34] A. Auerbach, N. Manini, and E. Tosatti, Phys. Rev. B **49**, 12998 (1994).

[35] J. Stinchcombe, A. Penicaud, P. Bhyrappa, P. D. W. Boyd, and C. A. Reed, J. Am. Chem. Soc. **115**, 5212 (1993).

[36] J. L. Dunn and C. A. Bates, Phys. Rev. B **52**, 5996 (1995).

[37] J. L. Dunn, I. D. Hands, and C. A. Bates, J. Mol. Struct. **838**, 60 (2007).

[38] I. D. Hands, J. L. Dunn, and C. A. Bates, Phys. Rev. B **73**, 014303 (2006).

[39] C. M. Varma, J. Zaanen, and K. Raghavachari, Science **254**, 989 (1991).

[40] O. Gunnarsson, H. Handschuh, P. S. Bechthold, B. Kessler, G. Ganteför, and W. Eberhardt, Phys. Rev. Lett. **74**, 1875 (1995).

[41] J. L. Dunn, in *Fullerenes for the New Millennium: Proceedings of the International Symposium on Fullerenes, Nanotubes, and Carbon Nanoclusters*, edited by K. M. K. Prashant V. Kamat, Dirk M. Guldi (The Electrochemical Society, Washington, DC, 2001), Vol. **11**, Chap. Vibronic coupling in fullerene systems, p. 585.

[42] I. B. Bersuker, in *The Jahn-Teller effect and vibronic interactions in Modern Chemistry*, *Modern inorganic chemistry*, edited by J. John P. Fackler (Plenum Press, New York, 1984).

[43] R. Tycko, R. C. Haddon, G. Dabbagh, S. H. Glarum, D. C. Douglass, and A. M. Mujsce, J. Phys. Chem. **95**, 518 (1991).

[44] R. Tycko, G. Dabbagh, R. M. Fleming, R. C. Haddon, A. V. Makhija, and S. M. Zahurak, Phys. Rev. Lett. **67**, 1886 (1991).

[45] P. A. Heiney, G. B. M. Vaughan, J. E. Fischer, N. Coustel, D. E. Cox, J. R. D. Copley, D. A. Neumann, W. A. Kamitakahara, K. M. Creegan, D. M. Cox, J. P. McCauley, and A. B. Smith, Phys. Rev. B **45**, 4544 (1992).

[46] R. C. Yu, N. Tea, M. B. Salamon, D. Lorents, and R. Malhotra, Phys. Rev. Lett. **68**, 2050 (1992).

[47] J. Onoe and K. Takeuchi, J. Phys. Chem. **99**, 16786 (1995).

[48] K. Kamarás, L. Akselrod, S. Roth, A. Mittelbach, W. Hönle, and H. von Schnering, Chem. Phys. Lett. **214**, 338 (1993).

[49] J. P. Lu, X.-P. Li, and R. M. Martin, Phys. Rev. Lett. **68**, 1551 (1992).

[50] A. B. Harris and R. Sachidanandam, Phys. Rev. B **46**, 4944 (1992).

[51] K. H. Michel, D. Lamoen, and W. I. F. David, Acta Crystallographica Section A Foundations of Crystallography **51**, 365 (1995).

[52] G. A. Samara, J. E. Schirber, B. Morosin, L. V. Hansen, D. Loy, and A. P. Sylwester, Phys. Rev. Lett. **67**, 3136 (1991).

[53] R. Komori and Y. Miyamoto, J. Phys. Chem. Solids **56**, 535 (1995).

[54] M. Dresselhaus, G. Dresselhaus, A. Rao, and P. Eklund, Synt. Met. **78**, 313 (1996).

[55] T. Pichler, R. Winkler, and H. Kuzmany, Phys. Rev. B **49**, 15879 (1994).

[56] F. Wooten, *Optical properties of solids.* (Academic Press, New York, 1972).

[57] A. Jayaraman, Rev. Mod. Phys. **55**, 65 (1983).

[58] J.-A. Xu, J. Yen, Y. Wang, and E. Huang, High Pressure Research **15**, 127 (1996).

[59] C. Narayana, H. Luo, J. Orloff, and A. L. Ruoff, Nature **393**, 46 (1998).

[60] M. I. Eremets, *High pressure experimental methods* (Oxford University press, New York, 1996).

[61] G. J. Piermarini and S. Block, Rev. Sci. Instrum. **46**, 973 (1975).

[62] W. A. Bassett, T. Takahashi, and P. W. Stook, Rev. Sci. Instrum. **38**, 37 (1967).

[63] H. Mao and P. Bell, in *Year Book Carnegie Inst.* (Carnegie Institute, Washington, 1978), Vol. **77**, Chap. Design and varieties of the megabar cell, pp. 904–908.

[64] G. Huber, K. Syassen, and W. B. Holzapfel, Phys. Rev. B **15**, 5123 (1977).

[65] L. Merrill and W. A. Bassett, Rev. Sci. Instrum. **45**, 290 (1974).

[66] A. Van Valkenburg, *Conference Internationale Sur-les-Hautes Pressions* (Le Creusot, Saone-et-Loire, France, 1965).

[67] S. Klotz, J.-C. Chervin, P. Munsch, and G. Le Marchand, J. Phys. D: Appl. Phys. **42**, 075413 (2009).

[68] R. J. Angel, M. Bujak, J. Zhao, G. D. Gatta, and S. D. Jacobsen, J. Appl. Crystallogr. **40**, 26 (2007).

[69] P. Bell and H. Mao, in *Carnegie Institution of Washington Year Book* (Carnegie Institute, Washington, 1981), Vol. **80**, pp. 404–6.

[70] A. Dewaele, P. Loubeyre, R. Andre, and J. Hartwig, J. Appl. Phys. **99**, 104906 (2006).

[71] R. A. Forman, G. J. Piermarini, J. D. Barnett, and S. Block, Science **176**, 284 (1972).

[72] J. D. Barnett, S. Block, and G. J. Piermarini, Rev. Sci. Instrum. **44**, 1 (1973).

[73] M. Born and E. Wolf, *Princleple of optics: Electromagnectic therory of propagation, interference, and diffraction of light* (Pergamon Press, London, 1959).

[74] D. R. Lide, in *Physical Constants of Organic Compounds in CRC Handbook of Chemistry and Physics, Student Edition*, No. 5 in *Internet Version*, ed., edited by D. R. Lide (CRC Press, Boca Raton, FL, 2005), .

[75] L. B. J. García Solé and D. Jaque, *An introduction to the optical spectroscopy of inorganic solids* (Hoboken, NJ : J. Wiley Sons Ltd, England, 2005).

[76] U. Fano, Phys. Rev. **124**, 1866 (1961).

[77] G. Caimi, L. Degiorgi, N. N. Kovaleva, P. Lemmens, and F. C. Chou, Phys. Rev. B **69**, 125108 (2004).

[78] Z. Li, C. H. Lui, E. Cappelluti, L. Benfatto, K. F. Mak, G. L. Carr, J. Shan, and T. F. Heinz, Phys. Rev. Lett. **108**, 156801 (2012).

[79] J. Fitzpatrick and J. A. Reffner, in *Handbook of Vibrational Spectroscopy*, edited by J. M.Chalmers and P. R. Griffiths (John Wiley and Sons Ltd, Chichester, 2002).

[80] J. D. Schuttlefield and V. H. Grassian, J. Chem. Educ. **85**, 279 (2008).

[81] R. Fleming, M. Rosseinsky, A. Ramirez, D. Murphy, J. Tully, R. Haddon, T. Siegrist, R. Tycko, S. Glarum, P. Marsh, and Others, Nature **352**, 701 (1991).

[82] D. Poirier, D. Owens, and J. Weaver, Phys. Rev. B **51**, 1830 (1995).

[83] C. A. Kuntscher, G. M. Bendele, and P. W. Stephens, Phys. Rev. B **55**, R3366 (1997).

[84] P. Dahlke and M. J. Rosseinsky, Chem. Mater. **14**, 1285 (2002).

[85] S. Hoffmann, D. Kasinathan, and T. F. Fässler, Inorg Chem. **49**, 2577 (2010).

[86] O. Zhou and D. E. Cox, J. Phys. Chem. Solids **53**, 1373 (1992).

[87] P. M. Allemand, G. Srdanov, A. Koch, K. Khemani, F. Wudl, Y. Rubin, F. Diederich, M. M. Alvarez, S. J. Anz, and R. L. Whetten, J. Am. Chem. Soc. **113**, 2780 (1991).

[88] A. Penicaud, A. Perez-Benitez, R. Gleason V., E. Munoz P., and R. Escudero, J. Am. Chem. Soc. **115**, 10392 (1993).

[89] S. Tomita, J. Andersen, E. Bonderup, P. Hvelplund, B. Liu, S. Nielsen, U. Pedersen, J. Rangama, K. Hansen, and O. Echt, Phys. Rev. Lett. **94**, 2 (2005).

[90] B. Sundqvist, Adv. Phys. **48**, 1 (1999).

[91] K. Thirunavukkuarasu, C. A. Kuntscher, G. Bényei, I. Jalsovszky, G. Klupp, K. Kamarás, E. Kováts, and S. Pekker, Phys. Status Solidi (b) **244**, 3857 (2007).

[92] K. Thirunavukkuarasu, C. A. Kuntscher, B. J. Nagy, I. Jalsovszky, G. Klupp, K. Kamarás, E. Kováts, and S. Pekker, J. Phys. Chem. C **112**, 17525 (2008).

[93] K. Pilz, A. Jobst, E. Lam, J. Lüdecke, J. Bao, W. Bietsch, and M. Schwoerer, Z. Kristallogr. **217**, 78 (2002).

[94] U. Bilow and M. Jansen, Z. Anorg. Allg. Chem. **621**, 982 (1995).

[95] P. Launois, R. Moret, N.-R. D. Souza, J. A. Barrios, and A. Penicaud, Eur. Phys. J. B **450**, 445 (2000).

[96] P. Kupser, J. D. Steill, J. Oomens, G. Meijer, and G. von Helden, Phys. Chem. Chem. Phys. **10**, 6862 (2008).

[97] H. Kondo, T. Momose, and T. Shida, Chem. Phys. Lett. **237**, 111 (1995).

[98] B. Gotschy and G. Völkel, Appl. Mag. Reson. **11**, 229 (1996).

[99] W.-Z. Wang, A. R. Bishop, and L. Yu, Phys. Rev. B **50**, 5016 (1994).

[100] B. Gotschy, M. Keil, H. Klos, and I. Rystau, Solid State Commun. **92**, 935 (1994).

[101] U. Becker, G. Denninger, V. Dyakonov, B. Gotschy, H. Klos, G. Röler, A. Hirsch, and H. Winter, Europhys. Lett. **21**, 267 (1993).

[102] J. Ihm, Phys. Rev. B **49**, 10726 (1994).

[103] P. Paul, Z. Xie, R. Bau, P. D. W. Boyd, and C. A. Reed, J. Am. Chem. Soc. **116**, 4145 (1994).

[104] K. Kamaras, Private communication .

[105] R. E. Stanton and M. D. Newton, J. Phys. Chem. **92**, 2141 (1988).

[106] V. Semkin, N. Spitsina, S. Król, and A. Graja, Chem. Phys. Lett. **256**, 616 (1996).

[107] D. R. Lawson, D. L. Feldheim, C. A. Foss, P. K. Dorhout, C. M. Elliott, C. R. Martin, and B. Parkinson, J. Electrochem. Soc. **139**, L68 (1992).

[108] W. H. Green, S. M. Gorun, G. Fitzgerald, P. W. Fowler, A. Ceulemans, and B. C. Titeca, J. Phys. Chem. **100**, 14892 (1996).

[109] J. Fulara, M. Jakobi, and J. P. Maier, Chem. Phys. Lett. **211**, 227 (1993).

[110] N. Koga and K. Morokuma, Chem. Phys. Lett. **196**, 191 (1992).

[111] I. D. Hands, J. L. Dunn, C. A. Bates, M. J. Hope, S. R. Meech, and D. L. Andrews, Phys. Rev. B **77**, 115445 (2008).

[112] G. A. Heath, J. E. Mc Grady, and R. L. Martin, J. Chem. Soc., Chem. Commun. 1272 (1992).

[113] R. Bolskar, Chem. Phys. Lett. **247**, 57 (1995).

[114] R. Kerkoud, P. Auban-Senzier, D. Jérome, S. Brazovskii, N. Kirova, I. Luk'yanchuk, F. Rachdi, and C. Goze, Synt. Met. **77**, 205 (1996).

[115] A. Sabouri-Dodaran, M. Marangolo, C. Bellin, F. Mauri, G. Fiquet, G. Loupias, M. Mezouar, W. Crichton, C. Hérold, F. Rachdi, and S. Rabii, Phys. Rev. B **70**, 174114 (2004).

[116] A. Huq and P. W. Stephens, Phys. Rev. B **74**, 075424 (2006).

[117] A. Iwasiewicz-Wabnig, T. Wågberg, T. Makarova, and B. Sundqvist, Phys. Rev. B **77**, 1 (2008).

[118] A. Iwasiewicz-Wabnig, T. Wågberg, and B. Sundqvist, J. Phys. Chem. Solids **69**, 1218 (2008).

[119] C. Bellin, J. C. Chervin, C. Hérold, and N. Bendiab, Phys. Rev. B **77**, 245409 (2008).

[120] M. G. Yao, B. Sundqvist, and T. Wågberg, Phys. Rev. B **79**, 081403 (2009).

[121] Y. Mingguang, W. Thomas, I.-W. Agnieszka, M. Tatiana L, and B. Sundqvist, J. Phys.: Conf. Ser. **215**, 012020 (2010).

[122] M. Fabrizio and E. Tosatti, Phys. Rev. B **55**, 13465 (1997).

[123] M. Capone, M. Fabrizio, P. Giannozzi, and E. Tosatti, Phys. Rev. B **62**, 7619 (2000).

[124] M. Capone, M. Fabrizio, and E. Tosatti, Phys. Rev. Lett. **86**, 5361 (2001).

[125] M. Capone, M. Fabrizio, C. Castellani, and E. Tosatti, Science **296**, 2364 (2002).

[126] R. C. Haddon, A. F. Hebard, M. J. Rosseinsky, D. W. Murphy, S. J. Duclos, K. B. Lyons, B. Miller, J. M. Rosamilia, R. M. Fleming, A. R. Kortan, S. H. Glarum, A. V. Makhija, A. J. Muller, R. H. Eick, S. M. Zahurak, R. Tycko, G. Dabbagh, and F. A. Thiel, Nature **350**, 320 (1991).

[127] G. Oszlányi, G. Baumgartner, G. Faigel, and L. Forró, Phys. Rev. Lett. **78**, 4438 (1997).

[128] A. Rezzouk, F. Rachdi, Y. Errammach, and J. Sauvajol, Physica E **15**, 107 (2002).

[129] M. Knupfer and J. Fink, Phys. Rev. Lett. **79**, 2714 (1997).

[130] G. Zimmer, K. Thier, M. Mehring, and F. Rachdi, Appl. Magn. Reson. **11**, 263 (1996).

[131] R. Haumont, P. Bouvier, A. Pashkin, K. Rabia, S. Frank, B. Dkhil, W. A. Crichton, C. A. Kuntscher, and J. Kreisel, Phys. Rev. B **79**, 184110 (2009).

[132] A. Sabouri-Dodaran, C. Bellin, M. Marangolo, F. Mauri, G. Fiquet, G. Loupias, M. Mezouar, T. Buslaps, C. Herold, and F. Rachdi, J. Phys. Chem. Solids **67**, 1132 (2006).

[133] H. Kataura, Y. Endo, Y. Achiba, K. Kikuchi, T. Hanyu, and S. Yamaguchi, J. Phys. Chem Solids **58**, 1913 (1997).

[134] X.-Y. Zhu, G. Dutton, D. P. Quinn, C. D. Lindstrom, N. E. Schultz, and D. G. Truhlar, Phys. Rev. B **74**, 241401 (2006).

[135] A. Wachowiak, R. Yamachika, K. H. Khoo, Y. Wang, M. Grobis, D.-H. Lee, S. G. Louie, and M. F. Crommie, Science **310**, 468 (2005).

[136] P. E. Eaton and T. W. Cole, J. Am. Chem. Soc. **86**, 3157 (1964).

[137] E. B. Fleischer, J. Am. Chem. Soc. **86**, 3889 (1964).

[138] B. D. Kybett, S. Carroll, P. Natalis, D. W. Bonnell, J. L. Margrave, and J. L. Franklin, J. Am. Chem. Soc. **88**, 626 (1966).

[139] V. Galasso, Chem. Phys. **184**, 107 (1994).

[140] P. M. Gehring, D. A. Neumann, W. A. Kamitakahara, J. J. Rush, P. E. Eaton, and D. P. VanMeurs, J. Phys. Chem. **99**, 4429 (1995).

[141] R. A. Dalterio and F. J. Owens, Solid State Commun. **67**, 673 (1988).

[142] T. W. Cole, J. Perkins, S. Putnam, P. W. Pakes, and H. L. Strauss, J. Phys. Chem. **85**, 2185 (1981).

[143] M. A. White, R. E. Wasylishen, P. E. Eaton, Y. Xiong, K. Pramod, and N. Nodari, J. Phys. Chem. **96**, 421 (1992).

[144] A. Detken, H. Zimmermann, U. Haeberlen, R. Poupko, and Z. Luz, J. Phys. Chem. **100**, 9598 (1996).

[145] T. Yildirim, P. M. Gehring, D. A. Neumann, P. E. Eaton, and T. Emrick, Phys. Rev. Lett. **78**, 4938 (1997).

[146] G. J. Piermarini, S. Block, R. Damavarapu, and S. Iyer, Propellants, Explosives, Pyrotechnics **16**, 188 (1991).

[147] S. Pekker, E. Kováts, G. Oszlanyi, G. Bényei, G. Klupp, G. Bortel, I. Jalsovszky, E. Jakab, F. Borondics, K. Kamarás, M. Bokor, G. Kriza, K. Tompa, and G. Faigel, Nature Mater. **4**, 764 (2005).

[148] W. I. F. David, R. M. Ibberson, J. C. Matthewman, K. Prassides, T. J. S. Dennis, J. P. Hare, H. W. Kroto, R. Taylor, and D. R. M. Walton, Nature **353**, 147 (1991).

[149] N. M. Nemes, M. García-Hernández, G. Bortel, E. Kováts, B. J. Nagy, I. Jalsovszky, and S. Pekker, J. Phys. Chem. B **113**, 2042 (2009).

[150] C. Lifshitz and P. E. Eaton, Int J Mass Spectrom Ion Phys. **49**, 337 (1983).

[151] G. Bortel, G. Faigel, E. Kováts, G. Oszlányi, and S. Pekker, Phys. Status Solidi (b) **243**, 2999 (2006).

[152] T. Yildirim, C. Kılıc, S. Ciraci, P. Gehring, D. Neumann, P. Eaton, and T. Emrick, Chem. Phys. Lett. **309**, 234 (1999).

[153] T. W. Cole, J. Perkins, S. Putnam, P. W. Pakes, and H. L. Strauss, J. Phys. Chem. **85**, 2185 (1981).

[154] G. Klupp, F. Borondics, E. Kováts, A. Pekker, G. Bényei, I. Jalsovszky, R. Hackl, S. Pekker, and K. Kamarás, J. Phys. Chem. B **111**, 12375 (2007).

[155] G. Bortel, S. Pekker, and E. Kováts, Cryst. Growth Des. **11**, 865 (2011).

[156] A. Iwasiewicz-Wabnig, B. Sundqvist, E. Kováts, I. Jalsovszky, and S. Pekker, Phys. Rev. B **75**, 024114 (2007).

[157] G. A. Samara, L. V. Hansen, R. A. Assink, B. Morosin, J. E. Schirber, and D. Loy, Phys. Rev. B **47**, 4756 (1993).

[158] Y. E. Stetsenko, I. V. Legchenkova, K. A. Yagotintsev, A. I. Prokhvatilov, and M. A. Strzhemechnyi, Low Temperature Physics **29**, 445 (2003).

[159] P. W. Stephens, L. Mihaly, J. B. Wiley, S.-M. Huang, R. B. Kaner, F. Diederich, R. L. Whetten, and K. Holczer, Phys. Rev. B **45**, 543 (1992).

[160] K. Meletov, D. Christofilos, G. Kourouklis, and S. Ves, Chem. Phys. Lett. **236**, 265 (1995).

[161] B. Morosin, Z. Hu, J. D. Jorgensen, S. Short, J. E. Schirber, and G. H. Kwei, Phys. Rev. B **59**, 6051 (1999).

[162] J. E. Schirber, G. H. Kwei, J. D. Jorgensen, R. L. Hitterman, and B. Morosin, Phys. Rev. B **51**, 12014 (1995).

[163] A. Abouelsayed, K. Thirunavukkuarasu, F. Hennrich, and C. A. Kuntscher, J. Phys. Chem. C **114**, 4424 (2010).

Acknowledgements

I express my gratitude to my supervisor Prof. Kuntscher for giving me an opportunity to work in her group. She patiently provided the encouragement and advise necessary for me to proceed through the work and complete my thesis.

I thank our collaborator Dr. Kamarás for the fruitful scientific discussions and giving me the chance to prepare samples in her lab as part of this work. I also thank the whole group of Dr. Kamarás for extending their support during my stay in Hungary, especially Mrs. K. Neméth and Dr. G.Klupp for their help with preparation of the samples. I appreciate Dr. S. Pekker and group for their scientific inputs.

I owe my heartfelt thanks to Mrs. Beate Shörhase, EP II for all the technical assistance offered for the smooth working of this project. I also appreciate Mrs. Danuta Trojak, EP II for her help with the glass sealing facility and all the other technical staffs of EP II. A special thanks to Mrs. Dana Vieweg, EP V, for her help with the x-ray diffraction measurements.

I would like to thank all my current and ex-colleagues for providing a nice working environment. I would like to acknowledge all the help they extended in every possible way during these years. I would like to thank Dr. A. Pashkin, Dr. L. Baldassarre, Dr. K. Thirunavukkuarasu, and Dr. R. Kaneez for introducing the experimental technique at the start of my PhD and their willingness to always assist me with any problem.

I am very thankful to Prof. Dr. Ramaprabhu, IIT Madras, India for introducing me to the vast and interesting filed of nanomaterials. I take this opportunity to thank Dr. Leela Mohana Reddy, Research Scientist, Rice University, USA for his constant motivation.

My friends who were a part of this journey especially Mr. Kannan, Dr. Pathikumar, Mrs. Smitha, Mr.Sathya, and others in India, Germany, and other parts of the world are greatly acknowledged. I wish to thank my parents Dr. J. Francis Lawrence and Mrs. Mary Porkodi for always being with me and extending their support in every possible way. My husband Sam Pravin, whose love and encouragement allowed me to be motivated through this journey. I thank my brother Felix for his support. I also

acknowledge all my friends and relatives who wished the best for me.

List of publications

- *Asymmetric Flexible Supercapacitor Stack.*
  Leela Mohana Reddy, F. Estaline Amitha, Imran Jafri and S. Ramaprabhu,
  Nanoscale Res Lett **3**, 145 (2008).

- *A nonaqueous electrolyte based asymmetric supercapacitor with Polymer and metal oxide/multi walled nanotube electrodes*
  F. Estaline Amitha, A. Leela Mohana Reddy and S. Ramaprabhu,
  J Nanopart Res **11**, 725 (2009).

- *Investigation of the Jahn-Teller effect in the monoanion under high pressure.*
  E. A. Francis, S. Scharinger, K. Németh, K. Kamarás, and C. A. Kuntscher,
  phys. stat. sol. (b) **247**, 3047 (2010).

- *Pressure-induced transition from the dynamic to static Jahn-Teller effect in* $(Ph_4P)_2IC_{60}$.
  E. A. Francis, K.Neméth, S.Scharinger, K.Kamarás and C.A.Kuntscher,
  Phys. Rev. B **85**, 195428 (2012).

- *Phase transitions in* $C_{60}{\cdot}C_8H_8$ *under hydrostatic pressure.*
  E. A. Francis, G. Durkó, I. Jalsovszky, G. Klupp, K. Kamarás, É. Kováts, S. Pekker, and C. A. Kuntscher,
  phys. stat. sol. (b) **249**, 2596 (2012).

Curriculum Vitae

Personal information

Date of birth : 21 Feb 1983
Nationality : Indian
Gender : Female

Education

June 1988 - May 1998	All India Secondary School Examination, Central Board of Secondary Education, India.
June 1998 - May 2000	St. Michael's Academy Matriculation Higher Secondary School, Chennai, India.
June 2000 - Apr 2003	Bachelor's degree in Physics, Stella Maris College (Autonomous), Chennai, India.
June 2003 - June 2005	Master's degree in Materials Science, Anna University, Chennai, India. Title: *Synthesis and thermal characterization of silica aerogel.*
June 2006 - Nov 2007	Master of Philosophy (M.Phil) degree in Physics, Bharathidasan University, Trichy, India. Title: *Synthesis of carbon nanotubes and study of their properties as electrodes for supercapacitors.*
Jan 2008 - Nov 2012	Research Assistant at Experimental Physics II, Universität Augsburg, Augsburg, Germany.